

**CZECH TECHNICAL
UNIVERSITY IN PRAGUE**

**FACULTY OF NUCLEAR
SCIENCES AND PHYSICAL
ENGINEERING**

Generation of laser radiation
in the atmospheric window
around the wavelength
of 2035 nm

MASTER'S THESIS

AUTHOR: Bc. Dominika Popelová

SUPERVISOR: Ing. Jan Šulc, Ph.D.

CONSULTANT: Ing. Jan Kratochvíl

ACADEMIC YEAR: 2023/2024

I. OSOBNÍ A STUDIJNÍ ÚDAJE

Příjmení: **Popelová** Jméno: **Dominika** Osobní číslo: **464814**
Fakulta/ústav: **Fakulta jaderná a fyzikálně inženýrská**
Zadávací katedra/ústav: **Katedra fyzikální elektroniky**
Studijní program: **Fyzikální elektronika**
Specializace: **Laserová fyzika a technika**

II. ÚDAJE K DIPLOMOVÉ PRÁCI

Název diplomové práce:

Generace laserového záření v atmosférickém okně v okolí vlnové délky 2035 nm

Název diplomové práce anglicky:

Generation of laser radiation in the atmospheric window around the wavelength of 2035 nm

Pokyny pro vypracování:

1. Seznamte se s metodami generace laserového záření v okolí vlnové délky 2035 nm a s jeho možnými aplikacemi. Zaměřte se na pevnolátkové lasery využívající thulium dopované aktivní prostředí a na možnost využití objemových Braggových mřížek.
2. Proveďte základní spektroskopickou charakterizaci dostupných thulium dopovaných krystalů z hlediska jejich využití pro konstrukci laseru.
3. Navrhněte a s využitím dostupných komponent sestavte diodově čerpaný laser generující záření v okolí vlnové délky 2035 nm.
4. Proveďte charakterizaci generovaného výstupního záření a srovnajte jednotlivé konstrukční varianty.

Seznam doporučené literatury:

1. Romano C., Panitzek D., Lorenz D., Forster P., Eichhorn M., Kieleck C., High-power thulium-doped fiber MOPA emitting at 2036 nm, Journal of Lightwave Technology, Early Access, doi: 10.1109/JLT.2023.3310121, 2023.
2. Gorajek L., Kwiatkowski J., Linearly polarized 2044-nm pulsed laser generation in Ho:YAG active medium, Optical Engineering 61, 046104, 2022.
3. McComb T. S., Sims R. A., Willis C. C. C., Kadwani P., Shah L., Richardson M., Atmospheric Transmission Testing Using a Portable, Tunable, High Power Thulium Fiber Laser System, in Conference on Lasers and Electro-Optics 2010, OSA Technical Digest, paper JThJ5, 2010.
4. Glebov L., Volume Bragg Gratings in PTR Glass - New Optical Elements for Laser Design, Advanced Solid-State Photonics (ASSP) Topical Meeting. ASSP Technical Digest, Paper MD1, Nara, Japan, 2008.
5. Glebov L., High brightness laser design based on volume Bragg gratings, Laser Source and System Technology for Defense and Security II. Proceedings of SPIE, vol. 6216, 621601, 2006.

Jméno a pracoviště vedoucí(ho) diplomové práce:

Ing. Jan Šulc, Ph.D. katedra fyzikální elektroniky FJFI

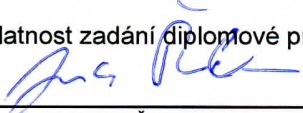
Jméno a pracoviště druhé(ho) vedoucí(ho) nebo konzultanta(ky) diplomové práce:


Ing. Jan Kratochvíl katedra fyzikální elektroniky FJFI

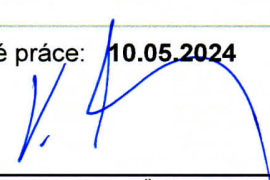
Datum zadání diplomové práce: **27.09.2023**

Termín odevzdání diplomové práce: **10.05.2024**

Platnost zadání diplomové práce: **27.09.2025**


Ing. Jan Šulc, Ph.D.
podpis vedoucí(ho) práce


prof. Dr. Ing. Ivan Richter
podpis vedoucí(ho) ústavu/katedry


doc. Ing. Václav Čuba, Ph.D.
podpis děkana(ky)

I declare that this thesis has been composed by myself and that all the literature used has been cited.

Prohlašuji, že jsem předloženou práci vypracovala samostatně a že jsem uvedla veškerou použitou literaturu.

Prague, 9.5.2024

Dominika Popelová



Název práce:

Generace laserového záření v atmosférickém okně v okolí vlnové délky 2035 nm

Autor: Dominika Popelová

Obor: Fyzikální elektronika

Specializace: Laserová fyzika a technika

Druh práce: Diplomová práce

Vedoucí práce: Ing. Jan Šulc, Ph.D.

Konzultant: Ing. Jan Kratochvíl

Abstrakt: Tato diplomová práce pojednává o generaci laserového záření v atmosférickém okně v okolí vlnové délky 2035 nm a je zaměřena především na thulium-dopovaná aktivní prostředí a na využití objemové Braggovy mřížky pro selekci vlnové délky.

V teoretické části jsou popsána thuliová aktivní prostředí, metody ladění laserové vlnové délky a možné aplikace záření v okolí vlnové délky 2035 nm. V experimentální části se nachází naměřené spektroskopické i laserové charakteristiky aktivních prostředí Tm:YAG, Tm:GGAG, Tm:YLF, Tm:YAP a Tm:KYW. Pomocí objemové Braggovy mřížky bylo dosaženo generace laserového záření v okolí vlnové délky 2035 nm.

Klíčová slova: Thuliové lasery, atmosférické okno, objemové Braggovy mřížky

Title:

Generation of laser radiation in the atmospheric window around the wavelength of 2035 nm

Author: Dominika Popelová

Branch: Physical Electronics

Specialization: Laser Physics and Technology

Thesis: Master's thesis

Supervisor: Ing. Jan Šulc, Ph.D.

Consultant: Ing. Jan Kratochvíl

Abstract: This master's thesis focuses on the generation of laser radiation in the atmospheric window around the wavelength of 2035 nm, with a particular emphasis on thulium-doped active media and the utilization of volume Bragg gratings for wavelength selection. The theoretical part covers thulium active media, methods of laser wavelength tuning, and potential applications of radiation around the wavelength of 2035 nm. The experimental section presents measured spectroscopic and laser characteristics of the active media Tm:YAG, Tm:GGAG, Tm:YLF, Tm:YAP, and Tm:KYW. Generation of laser radiation in the region around the wavelength of 2035 nm was achieved using a volume Bragg grating.

Key words: Thulium lasers, atmospheric window, volume Bragg gratings

Acknowledgement

I would like to express my sincerest gratitude to Ing. Jan Šulc, Ph.D. for the supervision of this thesis, a wealth of invaluable advice, patience and support. I am also grateful to Ing. Jan Kratochvíl for the consultation of this thesis. Furthermore, I would like to express my gratitude to prof. Ing. Helena Jelínková, DrSc., for her valuable advice during the final revisions of the thesis. I would also like to thank my friends and family for their unwavering support during the writing of this thesis.

Dominika Popelová

Contents

1	Introduction	10
2	Generation of radiation in the region around 2 μm	12
2.1	Thulium lasers	13
2.1.1	Tm:YAG	14
2.1.2	Tm:GGAG	15
2.1.3	Tm:YLF	15
2.1.4	Tm:YAP	16
2.1.5	Tm:KYW	17
2.1.6	Tm-doped materials parameters summary and comparison	18
3	Tuning elements for wavelength selection	20
3.1	Prisms	20
3.2	Diffraction gratings	21
3.2.1	Surface diffraction gratings	22
3.2.2	Volume Bragg gratings	23
3.3	Birefringent tuners	24
3.4	Etalons	26
4	Possible applications of radiation around 2035 nm	28
4.1	Free-space optical communications	28
4.2	LIDAR	29
4.3	Laser rangefinders	30
5	Experiments conducted by other researchers	31
5.1	Generation of radiation at 2044 nm in Ho:YAG active medium	31
5.2	Thulium-doped fiber MOPA emitting at the wavelength of 2036 nm	32
6	Experimental setup	33
6.1	Active media	33
6.2	Resonators and optical elements	34
6.3	Pumping	40
6.4	Description of spectroscopic measurements	41
6.5	Description of laser measurements	42

7	Experimental results	44
7.1	Characteristics of the pumping diode	44
7.2	Reflectivity and transmission spectra of optical elements	45
7.3	Results of spectroscopic measurements	47
7.3.1	Absorption spectra	47
7.3.2	Fluorescence spectra	49
7.3.3	Calculation of emission cross-sections	50
7.3.4	Fluorescence lifetimes	51
7.3.5	Evaluation of spectroscopic measurements	52
7.4	Laser characteristics	53
7.4.1	Lasers with semi-hemispherical resonator	53
7.4.1.1	Tm:YAG laser	53
7.4.1.2	Tm:GGAG laser	54
7.4.1.3	Tm:YLF laser	55
7.4.1.4	Tm:YAP laser	56
7.4.1.5	Tm:KYW laser	57
7.4.1.6	Laser spectra	58
7.4.1.7	Summary of the lasers with semi-hemispherical resonator	59
7.4.2	Lasers with V-shaped resonator	61
7.4.2.1	Tm:YAG laser	61
7.4.2.2	Tm:GGAG laser	61
7.4.2.3	Tm:YLF laser	62
7.4.2.4	Tm:YAP laser	62
7.4.2.5	Laser spectra	63
7.4.2.6	Summary of lasers with V-shaped resonator	63
7.4.3	Lasers with VBG	65
7.4.3.1	Tm:YAG laser	65
7.4.3.2	Tm:GGAG laser	66
7.4.3.3	Tm:YLF laser	66
7.4.3.4	Tm:YAP laser	66
7.4.3.5	Laser spectra	67
7.4.3.6	Summary of the lasers with VBG	68
7.4.4	Other experiments of Tm:YAG laser with VBG	70
7.4.4.1	Cooling	70
7.4.4.2	Generation in the CW regime	71
7.4.4.3	Short semi-hemispherical resonator	72

7.4.4.4 Q-switching	72
8 Conclusion	75
List of tables	77
List of figures	78
References	82

1 Introduction

Lasers play an important role in scientific research and technological advancements because of their unique properties, including high intensity, coherence, monochromaticity, and low beam divergence. These properties allow for a broad range of applications in various fields, including medicine, industry, scientific research, and the military. There is currently growing interest in laser systems that emit radiation in regions of atmospheric windows. Radiation in these wavelength ranges can be transmitted over long distances due to the minimal absorption by various gases (like water vapour, CO₂, etc.) present in the atmosphere. This property enables the use of these lasers for example in the remote sensing, LIDAR, and free-space communications. This thesis focuses on the generation of radiation within one of the atmospheric windows, specifically at a wavelength of 2035 nm.

The wavelength 2035 nm belongs to the short-wavelength infrared (SWIR) region of radiation, which ranges from 1.4 μm to 3 μm [1]. This spectral range contains atmospheric windows as well as regions of high absorption by water vapour and other gases in the atmosphere, as shown in Fig. 1a. The first significant atmospheric window is around the wavelength of 1.6 μm . This region of the spectrum is easy to produce with erbium lasers and is now widely used. An alternative

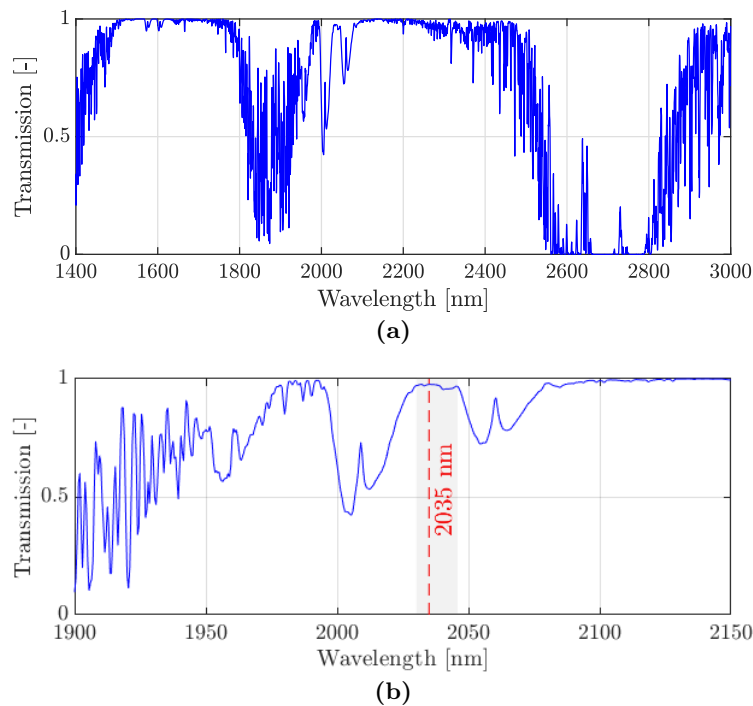


Fig. 1: Transmission of the atmosphere in the SWIR range (a) and detail around 2 μm (b). The data were measured by Caltech Optical Observatories.

to this atmospheric window is the region between approximately 2 and 2.2 μm , where several narrower atmospheric windows separated by water absorption peaks occur.

In the graph on the Fig. 1b can be seen that there is an increase in transmission in the region around 1980-2000 nm, however, observable absorption lines still exist in this spectral range. With an increased resolution of the data, these absorption lines would be stronger. The first region of high atmospheric transmission is observed between approximately 2030 and 2045 nm, followed by a broader region starting at around 2080 nm. The former has several advantages over the latter. Firstly, radiation near 2 μm can be generated using thulium-doped active media, which can be pumped by laser diodes operating at a wavelength of approximately 0.8 μm . Thulium active media and diodes designed for pumping are widely available. To produce radiation in the 2.1 μm range, holmium-active media are used. However, these require pumping at the 1.9 μm wavelength generated primarily by thulium lasers or laser diodes, which are very expensive. This leads to a higher complexity and a lower availability of these laser systems. Another advantage of generating radiation at shorter wavelengths around 2 μm is the higher sensitivity of InGaAs detectors compared to longer wavelengths.

To our knowledge, a thulium active medium with a fluorescence peaking at 2035 nm has not yet been found, which would be the simplest solution. An alternative is to use a tuning element located in the laser resonator, which allows for a shift in the wavelength of the generated radiation. Such elements include prisms, diffraction gratings, etalons or birefringent filters. This thesis focuses on the use of a volume Bragg grating to generate radiation near the wavelength of 2035 nm by thulium-doped bulk active media.

The research part of this thesis first explores the possibilities of generating radiation in the range of 2 μm wavelength and describes several active media. It also introduces the possibilities of wavelength tuning and stabilisation using tuning elements. Possible applications of radiation in the atmospheric window around the 2035 nm wavelength are then discussed, followed by a description of experiments performed by other authors in this area.

The experimental section of the thesis introduces the active media used for the experiments and their parameters, followed by detailed descriptions of the laser resonators with the used optical elements. Additionally, this section describes the instruments employed for pumping and for measuring the spectroscopic and laser properties, together with a description of the measurements. Finally, the results of spectroscopic and laser measurements for various experimental configurations are presented and compared.

2 Generation of radiation in the region around 2 μm

To achieve laser emission in the region of 2035 nm, it is necessary to find suitable active media with a high gain in this spectral region. This part of the thesis therefore focuses on thulium-doped active media that can be used to generate laser radiation at wavelengths close to 2 μm . These lasers belong to the category of solid-state lasers, which are focused on in this chapter. Furthermore, this category also includes holmium-doped active media generating radiation at the wavelength of 2.1 μm . However, in addition to the solid-state lasers, it is also possible to generate laser radiation in this wavelength region using thulium- and holmium-doped optical fibres, semiconductor lasers, or optical parametric oscillators [2, 3].

The wavelength around 2 μm is important in laser technologies as it is classified as a part of the ‘eye-safe’ wavelength range, which starts at approximately 1.4 μm . The presence of both water absorption peaks and atmospheric windows in this spectral region makes lasers emitting radiation around the 2 μm wavelength suitable for a wide range of uses, including medical and free-space applications. In the medicine, these lasers are mainly used in surgery due to their favourable water absorption properties. The absorption peak near 2 μm limits the penetration depth in biological tissues, facilitating localised heating and controlled tissue cutting. In addition, bleeding during laser cutting is suppressed by coagulation. These characteristics make 2 μm lasers ideal for a variety of surgical procedures [2, 4].

The ‘eye-safe’ nature of 2 μm lasers is important for free-space applications, particularly in LIDAR, as well as for optical communications. These lasers have also become very attractive due to their widespread applications in remote sensing, atmospheric gas detection and molecular spectroscopy. The high-power 2 μm lasers can efficiently serve as pump and seed sources for mid-infrared optical parametric amplifiers, using appropriate nonlinear optical materials [5, 6]. In addition, lasers emitting at the 2 μm wavelength are useful for environmental monitoring, measuring wind speed and detecting water vapour and carbon dioxide concentrations, which are crucial for weather forecasting and climate analysis [2, 4]. Possible applications of the radiation in the atmospheric window around the wavelength of 2035 nm are discussed in detail in the chapter 4.

Thulium belongs to the rare-earth elements in the lanthanide group. In crystals, the ions of this element are trivalent, but under certain conditions they can also be divalent. Rare-earth doped laser gain media typically exhibit relatively narrow spectral lines due to electron transitions occurring between levels within the partially filled 4f shells, which are well shielded by the filled 5s and 5p outer shells [7].

2.1 Thulium lasers

The thulium-doped active media, which can be described as quasi-three-level systems, enable the generation of a laser radiation at a wavelength of approximately 2 μm by a transition from the upper laser level $^3\text{F}_4$ to the thermally populated Stark level of the ground state $^3\text{H}_6$. In addition, radiation at wavelengths of 1.48 μm and 2.3 μm can also be generated [8]. The simplified energy level diagram of the Tm^{3+} ion is depicted in the Fig. 2. The thulium-doped active media can be pumped from the ground state to the energy level $^3\text{H}_4$ using AlGaAs laser diodes at a wavelength of approximately 0.8 μm . Furthermore, the pumping can be done directly to the $^3\text{F}_4$ level with radiation at a wavelength between 1600 and 1800 nm, although commercially available sources generating in this spectral range are limited [2, 10].

In thulium-doped active media, certain energy transfer processes may occur. After being excited to the energy level $^3\text{H}_4$, a thulium ion can undergo a non-radiative de-excitation to the $^3\text{F}_4$ level through the cross-relaxation process (CR), transferring energy to a nearby Tm^{3+} ion originally in the ground state $^3\text{H}_6$, which leads to its transition to the $^3\text{F}_4$ level. This is a 2-for-1 process, where the absorption of one pump photon results in the excitation of two ions. This enables a potential doubling of the energy conversion efficiency, theoretically reaching 82 % instead of 41 % [2]. An inverse process to the cross-relaxation is upconversion (UC), which results in the depletion of the $^3\text{F}_4$ level. This occurs when one ion decays from the $^3\text{F}_4$ level to the $^3\text{H}_6$ level, while another ion is excited from the $^3\text{F}_4$ level to the $^3\text{H}_4$ level. In contrast to the cross-relaxation

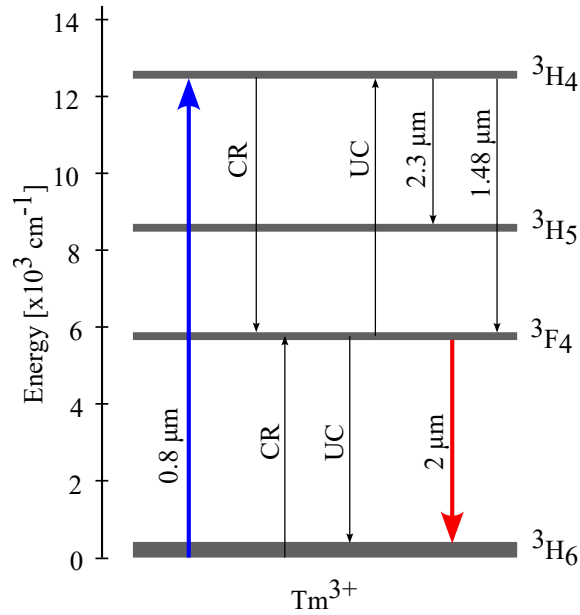


Fig. 2: Simplified diagram of energy levels of a Tm^{3+} ion. CR - cross-relaxation, UC - cooperative upconversion [2, 8, 9].

process, upconversion reduces the laser output power. In addition to these two processes, there can also be reabsorption at the laser wavelength, because the upper sublevels of the ground state are thermally populated. Since the probability of these processes depends on the concentration of a dopant, a certain optimal concentration levels of thulium ions can be found above which the influence of detrimental effects surpass the benefits of cross-relaxation [11].

Different matrices doped with thulium ions offer the possibility of generating radiation in the wavelength range from 1840 nm to 2100 nm. Thulium exhibits a broad and structured emission spectrum in most crystals, allowing tuning over a wide spectral range and also the generation of ultrashort pulses in mode-locked regime [2].

This thesis focuses on active media such as Tm:YAG, Tm:GGAG, Tm:YLF, Tm:YAP, and Tm:KYW, which are described in detail in the following sections.

2.1.1 Tm:YAG

One of the most commonly used matrices for doping with thulium ions is the yttrium aluminium garnet crystal ($\text{Y}_3\text{Al}_5\text{O}_{12}$ or YAG), which belongs to the group of crystals with a cubic lattice structure and a lattice constant of 12.013 Å [12]. Therefore, it is an isotropic material. It can be grown in a good quality and a large size using the Czochralski method. Among its favourable properties are high mechanical strength and good thermal conductivity ($13 \text{ W m}^{-1}\text{K}^{-1}$), which allows for high-power laser operation with a reduced risk of crystal damage [13]. On the other hand, this crystal is prone to forming a strong positive thermal lens, which must be compensated for to achieve high powers and good beam quality [10]. Its thermal coefficient of refractive index dn/dT is $7.8 \cdot 10^{-6} \text{ K}^{-1}$ (@ 1064 nm) [12]. Furthermore, thermally induced birefringence may occur in this crystal under high-power pumping, which may result in depolarisation losses [14]. The YAG crystal also have a relatively high phonon energy of 870 cm^{-1} [15].

The active medium Tm:YAG exhibits a strong absorption peak around a wavelength of 785 nm, which is suitable for diode pumping. The absorption cross-section at 785 nm is $6.5 \cdot 10^{-21} \text{ cm}^2$ [9]. Besides, a wing-pumping method is often used, where the pumping is performed outside the absorption peak, for example in the region of the 805 nm wavelength. Pumping at the wavelength of 785 nm has a disadvantage that it is absorbed over a very short distance in the active medium, leading to high heating near the pumping face, which has a negative effect on the laser performance. Pumping in the area around the 805 nm wavelength increases the absorption length in the crystal while still being effective in producing sufficient inversion of the population. Another method that helps to manage the problems of heating during pumping is the use of a crystal with diffusion bonded undoped end-caps [16].

The emission wavelength of the Tm:YAG laser can be tuned over a wide spectral range of approximately 1.9 to 2.15 μm [17,18]. The maximum power is typically achieved at a wavelength

of 2013 nm, which is also a typical wavelength at which this laser operates without a tuning element [9]. The emission cross-section at this wavelength is $0.22 \cdot 10^{-20} \text{ cm}^2$ [19]. The fluorescence lifetime of the ${}^3\text{F}_4$ energy level depends on the concentration of thulium ions. For a 1 % concentration, the lifetime is 11 ms, while for a 10.3 % concentration, it decreases to 9.1 ms [9].

2.1.2 Tm:GGAG

Another frequently employed garnet matrix is the cubic crystal $\text{Gd}_3\text{Ga}_5\text{O}_{12}$ (GGG), which is known for its high thermal conductivity, good mechanical properties and high damage threshold. In recent years, there has been a growing interest in disordered crystals. An example is the $\text{Gd}_3(\text{Ga}_{1-x}\text{Al}_x)_5\text{O}_{12}$ (GGAG) crystal. This crystal is formed by a random distribution of Ga and Al ions within the GGG crystal. It has a similar structure to the GGG crystal and preserves its favourable thermal properties. This material has a good thermal conductivity of $7.8 \text{ Wm}^{-1}\text{K}^{-1}$ [20]. Additionally, disordered hosts have attracted attention for their broad absorption and emission spectral lines, enabling better overlap between the absorption peaks and the spectrum of the pump diode radiation, which can change with temperature and current. Furthermore, the broadening of the spectral lines is also favourable for ultrashort pulses generation. The GGAG crystals can be grown to high quality using the Czochralski method [11]. The phonon energy of the GGAG crystal is 756 cm^{-1} [15].

The optimum concentration of Tm^{3+} ions in GGAG is likely to be between 1.4 and 6.9 at. %, with a probable value of around 2.4 at. %. This active medium exhibits an absorption peak at a wavelength of 786 nm and the absorption cross-section at this wavelength is $0.38 \cdot 10^{-20} \text{ cm}^2$ with FWHM of 11.5 nm. This value remains constant regardless of the thulium concentration [11]. The laser Tm:GGAG generates radiation around the wavelength of 2000 nm with a possibility of tuning in the range of 1856-2036 nm. For a concentration of thulium ions of 2.67 at. %, the fluorescence lifetime of transition ${}^3\text{F}_4 \rightarrow {}^3\text{H}_6$ is 11.6 ms [21].

2.1.3 Tm:YLF

Another suitable crystal that is widely used for doping with thulium ions is yttrium lithium fluoride (LiYF_4 or YLF). This crystal has a tetragonal structure with space group $I41/a$ and lattice parameters $a=5.17 \text{ \AA}$ and $c=10.82 \text{ \AA}$ [22]. It is therefore uniaxial, and due to its birefringence, it allows for an easy generation of linearly polarised radiation without depolarisation losses. The optical axis is designated as the c-axis, and with respect to it, two different orientations of radiation polarisation can be distinguished. The polarisation $E||c$ is denoted as π , and the polarisation $E \perp c$ (sometimes marked also as $E||a$) is denoted as σ [23]. Regarding the refractive index of this crystal, there is a distinction between the ordinary refractive index n_o for a beam polarised perpendicularly to the c-axis (i.e., in the σ direction) and the extraordinary refractive index n_e for a beam polarised

parallel to the c -axis (i.e., in the π direction) [1].

The main advantage of the crystal YLF is its small negative thermo-optic coefficient dn/dT ($-4.6 \cdot 10^{-6} \text{ K}^{-1}$ for $E||a$, $-6.6 \cdot 10^{-6} \text{ K}^{-1}$ for $E||c$ [24]), which is compensated by thermal expansion induced bulging of the crystal end faces [25]. It enables the generation of high-power laser radiation with a good beam quality. Another notable advantage is the lower phonon energy of 440 cm^{-1} , in comparison to, for example, the YAG crystal with a phonon energy that is approximately twice as high. Consequently, multi-phonon relaxations are much weaker in YLF crystals, making them often preferred for the generation of infrared radiation [26]. However, a disadvantage of this crystal is its lower thermal conductivity of $6 \text{ Wm}^{-1}\text{K}^{-1}$, along with its fragility and low thermal stress fracture limit [26, 27].

The optimal concentration for doping the YLF matrix with thulium ions is approximately 2 at. % [28]. The active medium Tm:YLF is often pumped at the wavelength in the range of 790-795 nm, and has a maximum absorption cross-sections of $0.361 \cdot 10^{-20} \text{ cm}^2$ at 794 nm for σ polarisation and $0.784 \cdot 10^{-20} \text{ cm}^2$ at 779 nm for π polarisation [23]. The output radiation of the Tm:YLF laser can be tuned over a wide spectral range of 1772-2145 nm (with the exception of a small range of 1801-1815 nm) [29]. In a free-running regime without a tuning element, this laser typically emits radiation around a wavelength of 1910 nm [25]. The emission cross-section at this wavelength is $0.369 \cdot 10^{-20} \text{ cm}^2$ [23]. The output radiation of the Tm:YLF laser is linearly polarised in the sigma direction [28].

Regarding the fluorescence lifetimes for the transition ${}^3F_4 \rightarrow {}^3H_6$, there is a wide range of values in the literature, which range from 15 to 17 ms for Tm³⁺ concentrations between 0.5 at. % and 6 at. % [28–30]. The observed variation in these values can be attributed to the growth conditions of the crystal. The presence of impurities as well as the increasing dopant concentrations result in an energy migration, which causes a decrease in the fluorescence lifetime [29]. A value reported for the radiative lifetime is 15.25 ms [29, 31].

2.1.4 Tm:YAP

Next significant laser host material is yttrium orthoaluminate perovskite (YAlO_3), also known as YAP or YALO. This crystal has an orthorhombic crystal structure with lattice constants of $a=5.329 \text{ \AA}$, $b=7.370 \text{ \AA}$, and $c=5.179 \text{ \AA}$ [32]. It is also birefringent, but unlike YLF, it is biaxial, characterized by three refractive indices corresponding to the three principal axes of the crystal, a , b , and c . Apart from its birefringence, it shares similar properties with YAG since both crystals are derived from the same $\text{Y}_2\text{O}_3\text{-Al}_2\text{O}_3$ system [14]. These properties include high mechanical strength, hardness, and excellent thermal conductivity ($11 \text{ Wm}^{-1}\text{K}^{-1}$) [9, 32]. However, similarly to YAG, YAP has a tendency to form a strong positive thermal lens. Its thermo-optic coefficient dn/dT for individual axes is $7.7 \cdot 10^{-6} \text{ K}^{-1}$ ($E||a$), $11.7 \cdot 10^{-6} \text{ K}^{-1}$ ($E||b$), and $8.3 \cdot 10^{-6} \text{ K}^{-1}$ ($E||c$)

[24]. This material has a relatively low phonon energy of 570 cm^{-1} , which reduces the probability of nonradiative transitions and improves laser efficiency [33].

The optimal concentration for doping thulium ions into the YAP matrix is typically between 1 and 4 at. % [9]. The active medium Tm:YAP is usually pumped around the wavelength of 794 nm. The strongest absorption peak for pump polarization $E||a$ is located at this wavelength, with an absorption cross-section of $8.64 \cdot 10^{-21}\text{ cm}^2$. For pump polarizations along the b and c axes, absorption peaks are found at a wavelength of 793 nm, with absorption cross-sections of $9.22 \cdot 10^{-21}\text{ cm}^2$ and $6.80 \cdot 10^{-21}\text{ cm}^2$, respectively [32]. These values were reported for a thulium ion concentration of 6 at. %, but may vary slightly at different concentrations [33]. Given that the strongest absorption peak occurs for the pump polarisation along the b axis, this orientation is often preferred over orientations along the a and c axes [32].

Furthermore, the strongest fluorescence is also observed for the polarisation along the b axis. The fluorescence peak is located around the wavelength of 1860 nm, with an emission cross-section of $0.433 \cdot 10^{-20}\text{ cm}^2$ [32]. The wavelength of the radiation generated by the Tm:YAP laser is dependent on the specific resonator, primarily on the choice of mirrors, and typically ranges from 1965 nm to 2020 nm, often around 1990 nm [14,34]. However, with the use of tuning elements, this laser can be tuned over an even wider range of 1869-2036 nm [34]. The fluorescence lifetime for the transition from the 3F_4 to the 3H_6 level decreases from 6.06 ms to 1.93 ms as the concentration of thulium ions increases from 2 at. % to 7.5 at. % [33].

2.1.5 Tm:KYW

The last discussed interesting matrices are double tungstates, such as potassium yttrium tungstate ($\text{KY}(\text{WO}_4)_2$ or KYW). It is a monoclinic crystal with a centrosymmetric space group $C2/c^1$. It is thus biaxial and its crystallographic axes are a, b, and c, with lattice constants $a=10.625\text{ \AA}$, $b=10.339\text{ \AA}$, $c=7.549\text{ \AA}$, and $\beta = 130.7^\circ$. The optical properties of this crystal are described with the use of orthogonal optical axes N_g , N_m , and N_p . The angle between the a axis and N_m axis is $\gamma = 59^\circ$, and the angle between c and N_g axis is $\delta = 18.5^\circ$. The b axis coincides with the N_p axis (Fig. 3) [35].

An advantage of this crystal is the broadening of its absorption lines due to strong electron-phonon interaction, which eliminate the necessity for precise pump wavelengths [36]. Additionally, it has been demonstrated that an N_g -cut KYW crystal is nearly athermal, with only a weak positive thermal lens. This is due to its positive anisotropic thermal expansion, which compensates for the negative change in refractive index with temperature [37]. On the other hand, the power of lasers

¹The KYW crystal can be described within both the space groups $C2/c$ and $I2/c$. In this thesis, the crystal is described using the $C2/c$ space group.

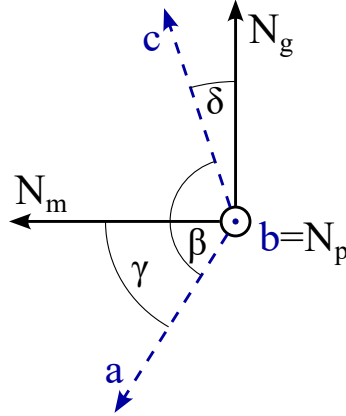


Fig. 3: Orientation of crystallographic axes a , b and c and optical axes N_m , N_p and N_g for the KYW crystal. Modified from [35].

with a KYW matrix is limited by its lower thermal conductivity of $3 \text{ Wm}^{-1}\text{K}^{-1}$. This crystal has a relatively high phonon energy of 905 cm^{-1} [38].

The anisotropy of thulium-doped KYW crystals is significant, as the absorption spectrum for pump polarisation $E||N_g$ is much less intense than the absorption spectrum for $E||N_m$ and $E||N_p$ polarisations. The absorption cross-section for polarisation $E||N_m$ peaks at a wavelength of 802 nm with a value of $5.4 \cdot 10^{-20} \text{ cm}^2$ and for polarization $E||N_p$ at a wavelength of 794 nm with a value of $6.4 \cdot 10^{-20} \text{ cm}^2$, while for $E||N_g$ its value is only around $0.8 \cdot 10^{-20} \text{ cm}^2$ at 802 nm. Consequently, the crystal geometry and pumping configuration are crucial [36]. The Tm:KYW active medium is typically pumped at wavelengths around 802 nm [39].

In the literature, numerous experiments on tuning Tm:KYW lasers have been reported. The widest tuning range observed is 1834-2111 nm, with maximum power at a wavelength of 1944 nm in continuous wave (CW) regime [40]. Additionally, tuning of mode-locked femtosecond Tm:KYW lasers has been performed in the range of 1979-2074 nm [41]. In free-running mode without a tuning element, this laser typically emits radiation around a wavelength of 1950 nm [42]. The active medium exhibits a high emission cross-section, its maximum value is $1.15 \cdot 10^{-20} \text{ cm}^2$ (@ 1910 nm) [39]. The lifetime of the active medium Tm:KYW at the ${}^3\text{F}_4$ energy level is short, ranging from approximately 1.5 to 1.34 ms, depending on the concentration of thulium ions from 0.7 at. % to 3.3 at. % [36]. A radiative lifetime of 1.47 ms has been reported in [43].

2.1.6 Tm-doped materials parameters summary and comparison

Tab. 1 contains the parameters of the mentioned thulium-doped active media. It also includes the refractive indices of the active media used in the experimental part of the thesis for calculating Fresnel losses and emission cross-sections. These refractive indices were obtained using the

Sellmeier equation [1]

$$n(\lambda) = \sqrt{1 + \sum_i \frac{A_i \lambda^2}{\lambda^2 - B_i}}, \quad (1)$$

which describes the wavelength-dependent refractive index of a medium and A_i and B_i are corresponding Sellmeier coefficients found in the literature [11, 38, 44–46].

Given the limited number of published articles on the active medium Tm:GGAG, several of its parameters, including the thermo-optic coefficient, radiative lifetime, and emission cross-section, remain unknown.

Tab. 1: Parameters of the thulium-doped active media. n - refractive index, dn/dT - thermo-optic coefficient, κ - thermal conductivity, E_{ph} - phonon energy, λ_p - typical pump wavelength, λ_l - typical laser emission wavelength, Δ_λ - tuning range, τ_f - fluorescence lifetime of the transition ${}^3F_4 \rightarrow {}^3H_6$, τ_r - radiative lifetime, σ_a - maximum absorption cross section, σ_e - maximum emission cross section. These values were reported for room temperature.

	Tm:YAG	Tm:GGAG	Tm:YLF	Tm:YAP	Tm:KYW
Crystal structure	Cubic	Cubic	Tetragonal	Orthorhombic	Monoclinic
n [-] @ 785 nm/2000 nm	1.82/1.8	1.9/1.89	1.45/1.44 (n_o), 1.47/1.46 (n_e)	1.93/1.93 (a), 1.92/1.92 (b), 1.91/1.91 (c)	2.07/2.04 (N_g), 2.02/1.99 (N_m), 1.98/1.96 (N_p)
dn/dT [10^{-6} K^{-1}] @ 1064 nm	7.8	-	-4.6 (σ), -6.6 (π)	7.7 (a), 11.7 (b), 8.3 (c)	-12.4 (N_g), -8.9 (N_m), -14.6 (N_p)
κ [$\text{Wm}^{-1}\text{K}^{-1}$]	13	7.8	6	11	3
E_{ph} [cm^{-1}]	870	756	440	570	905
λ_p [nm]	785	786	790-795	794	802
λ_l [nm]	2013	2000	1910	1990	1950
Δ_λ [nm]	1900-2150	1856-2036	1772-2145	1869-2036	1834-2111
τ_f [ms]	9.1-11	11.6	15-17	1.93-6.06	1.34-1.5
τ_r [ms]	12.3	-	15.25	4.6	1.47
σ_a [10^{-20} cm^2]	0.65	0.38	0.36 (σ), 0.78 (π)	0.86 (a), 0.92 (b), 0.68 (c)	5.4 (N_m), 6.4 (N_p)
σ_e [10^{-20} cm^2]	0.22	-	0.37	0.43	1.15
Ref.	[9, 12, 13, 15–19]	[11, 15, 20, 21]	[23–31]	[9, 14, 24, 32–34]	[35–38, 40, 42, 43]

3 Tuning elements for wavelength selection

Many laser active media exhibit a broad gain curve. These include primarily vibronic solid-state lasers such as Ti:sapphire or alexandrite lasers. In the spectral range under investigation, the Tm:YAG laser is an example. For certain applications, it is necessary to limit the spectral range of generation to a specific wavelength at which the laser will operate [7, p. 297].

Certain other active media may have gain at multiple transitions. In such cases, the laser operates at a transition where the threshold condition is met first. However, it is possible to induce larger losses for this laser transition, resulting in the generation of radiation at a different wavelength [1, 47].

In both cases, the wavelength of the laser radiation can be selected by inserting an optical tuning element into the resonator. These elements include prisms oriented at appropriate angles, diffraction gratings, volume Bragg gratings, etalons, or birefringent tuners [48, p. 25].

This chapter provides a description of the individual tuning elements. A disadvantage of this method is that the wavelength tuning is limited to the gain bandwidth of the active medium. In order to generate radiation at a wavelength that cannot be achieved with the available active media, it is necessary to consider the generation of radiation by non-linear effects.

3.1 Prisms

A prism is one of the suitable elements for wavelength tuning. It is typically made of optically transparent highly-dispersive dielectric material (glass, crystal or ceramic). Its properties make it useful in optics for various purposes, such as changing the orientation of an image or deflecting a beam. Combinations of multiple prisms are extensively used, for example, as beam splitters or polarizers [49, p. 199].

One of the main features of a prism is its ability to deflect a beam from its original path. If a beam enters the prism at an angle θ (Fig. 4a), and the apex angle of the prism is α , the equation for deviation angle δ , which can be calculated using Snell's law, is [49, p. 200]

$$\delta = \theta + \sin^{-1}[(\sin \alpha)\sqrt{n^2 - \sin^2 \theta} - \sin \theta \cos \alpha] - \alpha. \quad (2)$$

It can be observed in the equation (2) that the deviation angle increases as the refractive index grows, at a constant angle of incidence θ and apex angle α . Another important property of a prism is that it is a dispersive medium, which means that its refractive index depends on frequency. In the visible spectrum, the refractive index of most transparent materials increases with the frequency of radiation, resulting in an increased deviation angle. This effect is referred to as normal dispersion. As a result, blue light is deflected more than red light (Fig. 4b) [49, p. 200].

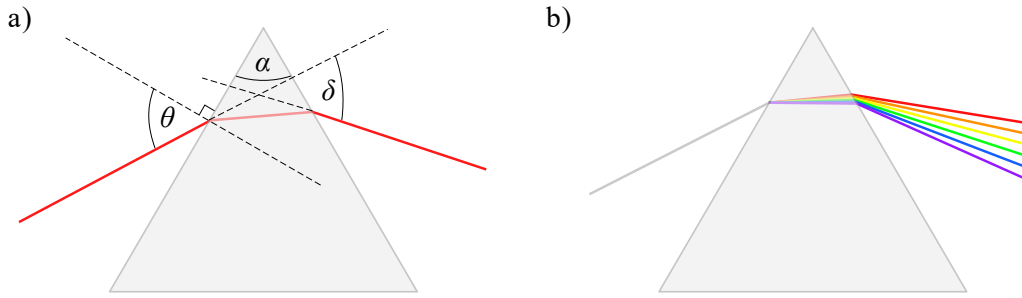


Fig. 4: Passage of radiation through a prism.

However, in the infrared spectrum, resonance occurs if the radiation frequency is close to the natural frequency of atomic vibrations in molecules, leading to the energy absorption. In this spectral range, anomalous dispersion occurs, rendering conventional transparent prisms unsuitable for use in the infrared spectrum [49, p. 82]. If radiation in the ultraviolet spectrum interacts with dielectric materials, electron transitions from the valence band to the conduction band occur, which also results in strong absorption of radiation [1]. A suitable material for the manufacture of prisms that can be used in the UV, VIS or IR is CaF_2 with a transmission in the range of 0.2 to 9 μm [50].

In order to adjust the wavelength of the laser, the experimental setup shown in Fig. 5 can be used. An appropriately chosen prism is placed in the resonator at a suitable angle, and one of the end mirrors is shifted so that only the desired wavelength is reflected perpendicularly [47, p. 285].

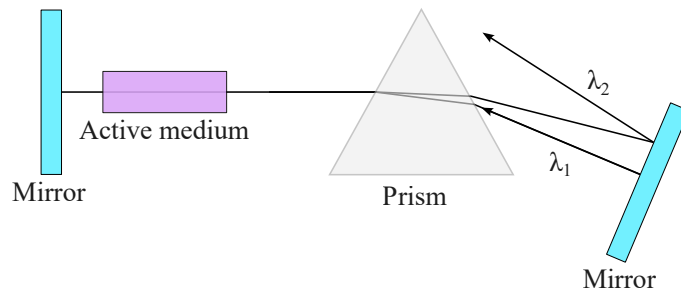


Fig. 5: Setup of a laser with a prism for wavelength tuning [47, p. 285].

3.2 Diffraction gratings

A diffraction grating is an optical element which diffracts incident waves by periodically modulating their amplitude or phase. This modulation is achieved by periodically varying the refractive index or thickness of the grating. The resulting diffraction pattern is dependent on the wavelength of the incoming wave. There are different types of diffraction gratings. Reflective gratings have a reflective surface, while transmissive gratings allow the incident beam to pass through to the other side. Furthermore, gratings can be classified as surface gratings, where diffraction occurs

on or near the surface, and volume gratings, where diffraction occurs within the volume of the element [1].

Diffraction gratings have several important parameters, one of which is diffraction efficiency. It is the ratio of the power of the radiation in a given diffraction order to the power of the incident radiation. The diffraction efficiency depends on the grating itself, the wavelength of the beam and its angle of incidence. Another important parameter is the line density, which determines the angular dispersion [51]

$$D = \frac{d\theta_m}{d\lambda} \quad , \quad (3)$$

which is the angular separation per unit wavelength. It is also important for a diffraction grating to have a high damage threshold, which is determined by the absorption of radiation in the material. It is therefore advantageous for diffraction gratings, especially for applications with pulsed lasers, to have low absorption losses. Other important parameters to consider include spectral resolution, polarisation dependence, thermal properties and dimensions of the grating [1, 51].

3.2.1 Surface diffraction gratings

In the case of surface gratings, reflective gratings are more common. These have a periodic relief on the surface which causes a phase modulation of the incident wave. These gratings are typically made of a metal such as gold, silver or aluminium. Transmissive gratings can produce modulation either by relief or holographic pattern. These gratings are usually made of a dielectric material (e.g. glass) [1].

When a beam is directed onto a surface grating, it is diffracted into various orders at angles determined by the grating equation [52]

$$\sin \theta_m = \sin \theta_i + m \frac{\lambda}{\Lambda} \quad , \quad (4)$$

where λ is the wavelength of the incoming wave, Λ is the period of the grating, m is the order of diffraction, θ_i is the incident wave angle, and θ_m is the angle of the wave diffracted into the m -th order. Due to the dependence of the output angles on the wavelength, the incoming polychromatic beam is diffracted into its individual spectral components. All wavelengths are contained in the zeroth diffraction order at the same angle. Unlike prisms, the deviation of the beam diffracted by a diffraction grating is higher at longer wavelengths [1, 51, 52].

The type of surface grating with the highest diffraction efficiency is the blazed grating, which has a surface formed by a sawtooth-shaped relief with a blaze angle. The slope of this surface profile has to be optimised for a specific incident angle and wavelength [1].

For tuning the laser wavelength, reflective surface gratings in Littrow configuration are used, in which the diffracted beam (often the first order) is reflected along the same path as the incident beam (Fig. 6) [1, 48]. The incident beam has to be perpendicular to the relief faces so that the

angle of incidence is equal to the blaze angle. In this case, the grating equation 4 is transformed to

$$\sin \theta_b = \frac{m\lambda}{2\Lambda}, \quad (5)$$

where θ_b is a blaze angle of the grating [51].

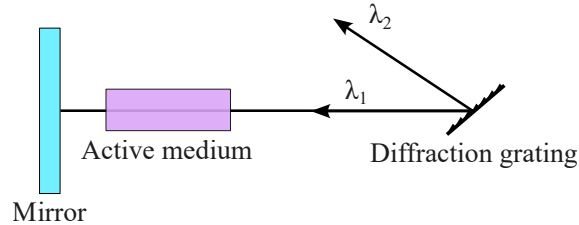


Fig. 6: Setup of a laser with a diffraction grating in Littrow configuration for wavelength tuning [47, p. 285]

3.2.2 Volume Bragg gratings

A volume Bragg grating is an optical element made of transparent material with a periodic modulation of the refractive index. Unlike surface diffraction gratings, which are created on the surface of a material, in this case, the Bragg grating is inscribed into the volume of a bulk material. One of the main properties of a volume Bragg grating is its high reflectivity for a very narrow range of wavelengths around the central wavelength which satisfies the Bragg condition [1]:

$$\frac{2\pi}{\Lambda} = 2 \cdot \frac{2\pi n}{\lambda} \cos \theta, \quad (6)$$

where Λ is the grating period, λ is the wavelength of a radiation in vacuum, n is the refractive index of the material and θ is the angle of propagation of the beam relative to the perpendicular direction to the Bragg grating [1].

A volume Bragg grating is typically created by exposing a photosensitive material to ultraviolet radiation in a form of an interference pattern, followed by thermal development. One of the materials suitable for inscribing a Bragg grating is photo-thermo-refractive (PTR) glass. This is a $\text{Na}_2\text{O-ZnO-Al}_2\text{O}_3\text{-SiO}_2$ glass doped with silver, cerium and fluorine. This material is transparent to radiation in the range 350-2500 nm and its diffraction efficiency exceeds 95 %. Its main advantage is the high stability of the Bragg grating when exposed to UV, VIS, IR, X-rays and gamma radiation [53].

Volume Bragg gratings are classified into two types: reflecting (Fig. 7a) and transmitting (Fig. 7b). Reflecting Bragg gratings diffract the beam λ_d on the same side as the incident beam λ_i enters the material. Transmitting Bragg gratings diffract the beam on the same side as the transmitted beam λ_t leaves the material. In general, Bragg gratings can be oriented at any angle in the material [53].

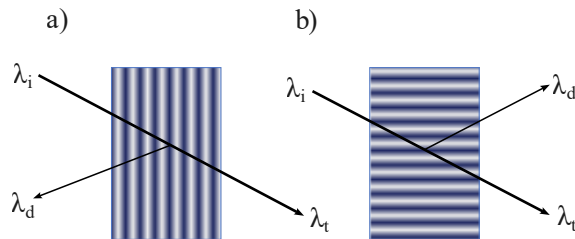


Fig. 7: Reflecting (a) and transmitting (b) volume Bragg grating.

Compared to conventional optical elements like prisms and surface diffraction gratings, volume Bragg gratings exhibit significantly different dispersive properties. If a beam is directed into a conventional optical element at a constant angle, the beams of individual wavelengths propagate at different angles after interacting with the material. Altering the angle of incidence of the beam will result in corresponding changes in the output angles. However, if a beam irradiates a volume Bragg grating at an angle called the Bragg angle θ , only the beam with a wavelength satisfying the Bragg condition (6) will be diffracted. For other wavelengths, the material behaves like a plane-parallel plate of glass. For different angles of incidence, a beam with a different wavelength can be diffracted. Depending on the period and thickness (several mm) of the grating, high spectral selectivity (tens of pm) and high angular selectivity (below 1 mrad) can be achieved [1, 53, 54].

Volume Bragg gratings can be used in various applications. If a reflective form of a Bragg grating is used in the resonator of a solid-state laser as an output mirror, it can effectively narrow the laser spectrum [55]. Furthermore, volume Bragg gratings are also used in laser diodes to stabilise the wavelength, which would otherwise depend on temperature [56]. It is also used in regenerative amplifiers (e.g. Nd:YLF) to suppress background noise [57]. Due to their high angular selectivity, volume Bragg gratings can be applied for the selection of any transverse mode of a laser [58]. In addition to these applications, it is possible to use volume Bragg gratings for spectral beam combining and beam deflection. Chirped volume Bragg gratings, which have a gradually changing grating period, are used also for stretching and compressing of laser pulses [54].

3.3 Birefringent tuners

The birefringent tuner is another component suitable for tuning the laser wavelength. It is made of an anisotropic material (e.g. quartz or KDP) in the form of a plane-parallel plate placed between two polarizers with their axes parallel to the plane of incidence of the beam (Fig. 8). The optical axis of the birefringent material is oriented in the plane of the plate, and the plate is placed inside the resonator at the Brewster angle with respect to the incident beam. Due to this angle, the p-polarised beam passes through the element without reflection. If the Fresnel losses for s-polarisation are sufficiently high, it is possible to use the tuner without polarizers [47, p. 286].

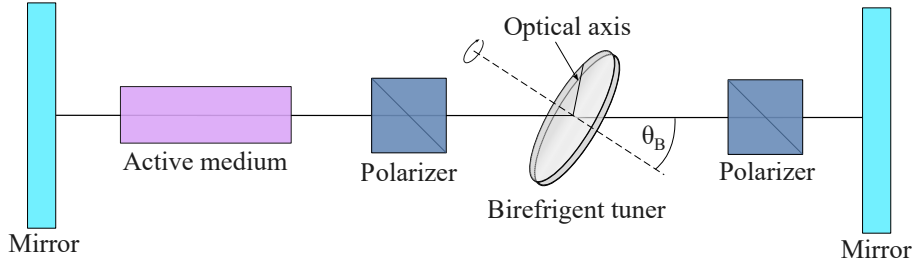


Fig. 8: Setup of a laser with a birefringent tuner and polarizers for wavelength tuning [47, p. 286].

If the optical axis of the birefringent tuner is oriented at any angle in the plane of the plate which is neither perpendicular nor parallel to the electric field vector of the beam, the beam will contain both ordinary and extraordinary components with the propagation direction depending on the angle between the optical axis and the electric field vector. A phase shift occurs between these components [47, p. 286]:

$$\Delta\Phi = \frac{2\pi}{\lambda}(n'_e - n_o)L_e, \quad (7)$$

where n_o and n'_e are the refractive indices for the ordinary and extraordinary beam, and L_e is the thickness of the plate along the path of the beam. It is essential to note that the refractive index n'_e is not equivalent to the extraordinary refractive index of the material n_e . Rather, it is a combination of the ordinary and extraordinary refractive indices. For instance, in the case of a uniaxial negative crystal where $n_e > n_o$, the refractive index n'_e can be expressed as [1]

$$n'_e = \frac{1}{\sqrt{\frac{\cos^2 \varphi}{n_o^2} + \frac{\sin^2 \varphi}{n_e^2}}}, \quad (8)$$

where φ is the angle between propagation direction in the birefringent material and its optical axis.

At the output, these beam components typically produce radiation with elliptical polarisation and therefore losses at the second polarizer will occur. However, if the phase difference corresponds to an integer multiple of 2π , the polarisation of the beam remains unchanged and, in the case of ideal polarizers, the beam passes through without loss. In this case, the equation

$$\frac{2\pi}{\lambda}(n'_e - n_o)L_e = 2\pi l, \quad (9)$$

where l is an integer, can be written. This equation can be used to determine the wavelengths at which the transmission is at its maximum. To shift the transmission curve, the tuner can be rotated about an axis perpendicular to the surface of the plate. The incident angle remains unchanged, but the orientation of the optical axis relative to the beam polarisation changes, which modifies the refractive index n'_e . The tuning range is determined by the thickness of the plate and its birefringence. Thinner birefringent tuners have a larger tuning range [47, p. 287].

If a single birefringent tuner is used, the transmission curve can be approximately described by a sinusoidal function. To achieve a curve with narrower transmission peaks, multiple birefringent tuners can be used in series. The configuration, where the thickness of each plate is half that of the previous plate, is called a Lyot filter. The configuration allows for achieving narrow transmission peaks with a large period [1].

3.4 Etalons

An alternative method for adjusting the laser wavelength is to use an etalon. It is composed of a transparent plane-parallel plate, typically made of fused silica, or two flat semitransparent mirrors separated by an air gap (Fabry-Pérot etalon) or by a medium with a refractive index n . This etalon acts as a resonator with its transmission periodically changing with the frequency of the incident radiation. By increasing the reflectivity R_1 and R_2 of the etalon surfaces, it is possible to narrow the spectral width of the etalon mode and thus increase the finesse F of the etalon, which is the ratio of the frequency spacing between two subsequent etalon modes to their FWHM [1]. According to [47, p. 145], following equation applies to finesse:

$$F = \frac{\pi(R_1 R_2)^{1/4}}{1 - (R_1 R_2)^{1/2}}. \quad (10)$$

Fig. 9 illustrates the longitudinal modes that the laser can generate, both before and after the insertion of the etalon. Before inserting the etalon into the laser resonator with a length of d ,

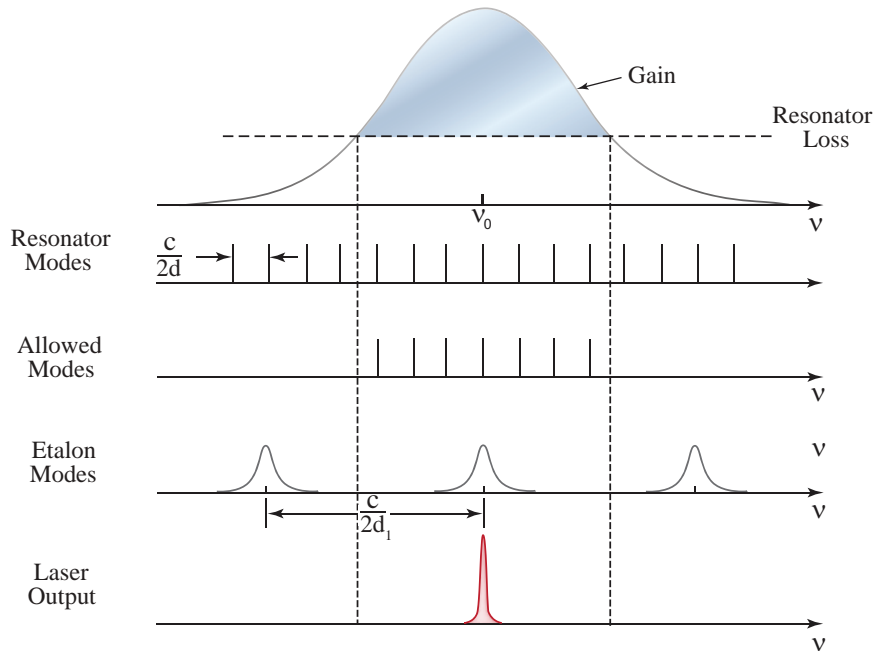


Fig. 9: Possible generated longitudinal laser modes before and after inserting an etalon [48, p. 13].

longitudinal modes that fall within the gain bandwidth can be generated. The frequencies of these modes are such that the resonator length is equal to an integer multiple of half-wavelengths. If an etalon with a length d_1 , containing only one mode within the gain bandwidth, is inserted into the laser resonator and this mode overlaps with a resonator mode, only one longitudinal mode of the laser is generated [48, p. 12]. For frequencies at which the etalon achieves maximum transmission, the following equation holds [47, p. 292]:

$$\nu_m = \frac{mc_0}{2nd_1 \cos \theta'}, \quad (11)$$

where c_0 is the speed of light in vacuum, θ' is the angle of refraction of the beam inside the etalon, and m is an integer.

Fig. 10 shows a schematic of a laser resonator with an inserted etalon for wavelength tuning. In order to achieve maximum transmission at the desired frequency, a suitable etalon tilt angle θ has to be chosen.

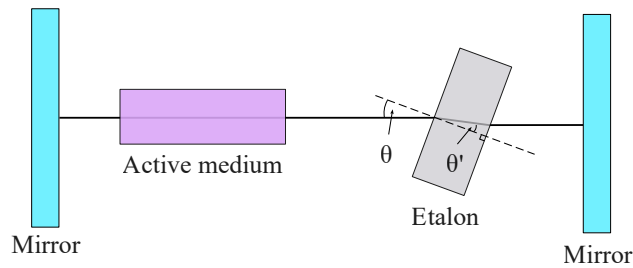


Fig. 10: Setup of a laser with an etalon for wavelength tuning.

4 Possible applications of radiation at the wavelength around 2035 nm

4.1 Free-space optical communications

Lasers operating at wavelengths within an atmospheric window can be used in free-space optics (FSO) to transmit data through unobstructed space via laser beams, eliminating the need for optical fibres. Although fibre-optic cables are widely used in network infrastructure, their associated costs remain prohibitively high. Furthermore, the process of laying optical fibres is often associated with delays. Another disadvantage is the low operability of the system, which presents challenges, for instance, in the case of customer relocation. An alternative option is to use radio frequency (RF) technologies, which, however, provide a maximum bit rate of only 622 Mbps. Another disadvantage of radio waves is that they can be more easily eavesdropped. Besides, there are copper-based technologies that are widely available, although they have a limited data rate of 2 to 3 Mbps. Free-space optical communications provide a viable alternative to these conventional technologies, allowing for optical data transmission at speed of up to 2.5 Gbps over considerable distances, spanning several kilometres [59].

A communication system that uses FSO optics consists of a laser transmitter with a telescope and a receiver on both ends, ensuring bidirectional transmission. At the source, the laser beam is modulated with data for transmission. At the destination, the beam is detected by a photodetector and the data are demodulated [59].

Communication via FSO offers several advantages. Firstly, it has a wide bandwidth and higher transmission speed compared to optical fibres, where light propagates more slowly. In addition, FSO communication requires much lower costs and is easier to deploy than optical fibres. However, this technology is not without challenges. Line of sight is required to establish a connection between the source and destination, and any obstacle along the way will result in a signal loss. Additionally, weather conditions, such as fog, can pose a problem as small particles of water can cause light absorption, scattering, and reflection. Even under optimal conditions, absorption can occur in the atmosphere due to dispersed water droplets. For this reason, lasers that generate radiation in the atmospheric window, where absorption is substantially lower, are preferred [59].

Most FSO systems use radiation in the near-infrared (NIR, $\approx 750\text{-}1400$ nm) and short-wavelength infrared (SWIR, $\approx 1400\text{-}3000$ nm) regions because they are commonly used for optical fibres and the components are widely available. However, the NIR wavelength region poses a risk to the eye as it can reach the retina. In contrast, the SWIR region is relatively eye-safe, making radiation in the atmospheric window region around 2035 nm suitable for this application [1, 60].

4.2 LIDAR

Due to the ability of radiation within the atmospheric window to propagate through the air over long distances, these lasers can have an application in the technology known as LIDAR (Light Detection and Ranging), which is used, for example, to measure a distance and speed of objects and create 3D images of them, as well as to quantify other parameters such as the concentration of various gases in the atmosphere. LIDAR works by sending a laser beam towards a target and then detecting the reflected or scattered radiation. One category is time-of-flight LIDAR, which sends short pulses towards the target and measures the time it takes for the pulse to return, which is used to determine the distance to the target. In addition, it is possible to record changes in the wavelength of the incoming radiation, which can be used to determine the relative speed of the object with respect to the observer because of the Doppler effect. A block diagram of this type of LIDAR is shown in Fig. 11. A laser, powered by a laser power supply, generates radiation that passes through focusing optics and subsequently arrives at the target. From there, it is reflected back and captured by other focusing optics. It passes through a filter that selects the desired wavelength before being detected by a photodetector, which sends the signal to a computer. The whole system can be rotated by motors [1, 61].

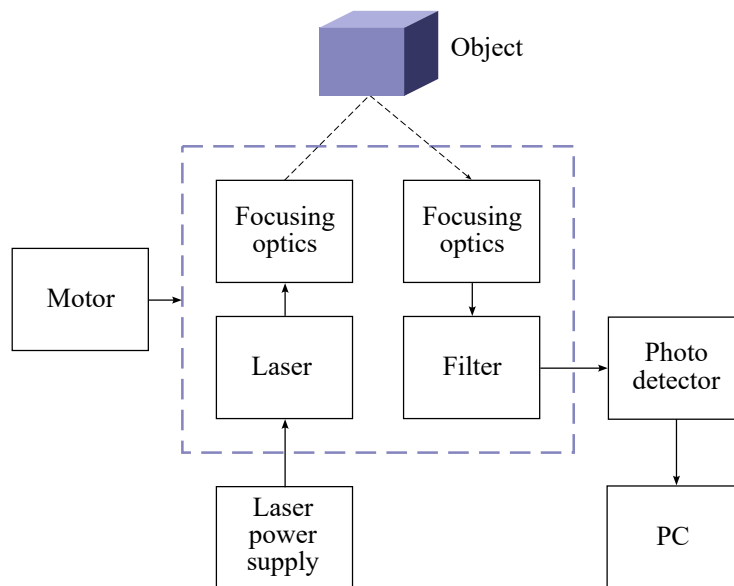


Fig. 11: Block diagram of LIDAR using the time-of-flight method [61].

Second category is coherent LIDAR, which uses heterodyne detection. This involves mixing coherent radiation emitted from the source with radiation reflected from the object. Information about the object is then obtained from the beat note that occurs during the interference of signals. This method does not require short pulses and is considerably more sensitive than the time-of-flight

method [62].

LIDAR, which records radiation reflected or scattered from solid objects, is utilized, for instance, for topographic mapping, autonomous vehicle navigation, or security surveillance (airborne LIDAR). However, it is not only solid objects that can be detected by this method. There are many other aspects utilized in LIDAR that serve to measure various quantities. Radiation can be scattered also from small particles in the atmosphere, enabling the measurement of wind speed (e.g., for wind turbines) and turbulence (in aviation). Furthermore, LIDAR can be used for remote atmospheric composition analysis. In this method, the reflected radiation is used to measure the absorption of radiation by various gases in the atmosphere using Differential Absorption LIDAR (DIAL). The measured absorption can then be used to determine the concentration of the gases. This technique can be used, for example, to measure the concentration of CO₂, which has an absorption peak at a wavelength of 2.05 μm [1, 63].

4.3 Laser rangefinders

Radiation around the wavelength of 2035 nm also has a potential application in laser rangefinders, which are used to measure a distance to a specific object. Similarly to LIDAR, laser rangefinders can be also based on the time-of-flight method. Short pulses are emitted and the time it takes for the pulse to return after reflection from the object is used to calculate the distance. Another method used by rangefinders is the phase-shift method. This method involves emitting high-frequency sinusoidal intensity modulation radiation instead of laser pulses. The reflected modulated signal is recorded by the detector, and the distance to the object is determined from the phase shift of the modulation. However, a problem arises because a change in distance of $c/2f$ corresponds to a phase change of 2π . To overcome this problem, radiation is emitted at several different frequencies. Laser rangefinders have many applications. They can be used to measure distances on construction sites, in geodetic measurements or in military technologies (for example, for reconnaissance purposes) [1].

5 Experiments conducted by other researchers

To date, there have been only a few experiments performed by other researchers in which radiation within the atmospheric window around the wavelength of 2035 nm was generated. Only two experiments were found in the literature. One utilized a solid-state Ho:YAG active medium, which generated radiation at a wavelength of 2044 nm. In the second experiment, radiation at 2036 nm was generated by a thulium-doped fibre laser. These two experiments will now be described in detail.

5.1 Generation of radiation at 2044 nm in Ho:YAG active medium

One of the performed experiments of the generation of radiation near the wavelength of our interest, is that of L. Gorajek and J. Kwiatkowski in 2022 [64]. The experiment focused on generating laser radiation at a wavelength of 2044 nm using a Ho:YAG active medium. Fig. 12 shows the experimental setup. The active medium was pumped by a thulium fibre laser (TDFL) through a folding mirror (DP1). To stabilize the laser wavelength at 2044 nm, a volume Bragg grating (VBG) was placed in the folded arm of the resonator to avoid high power pump radiation. Output couplers (OC) with various transmittances (6%, 10%, 20% and 30%) and a radius of curvature of 200 mm were used at the end of the resonator. To generate Q-switched pulses, an acousto-optic modulator (AOM) was placed between the active medium and the output coupler. A dichroic beam splitter (DP2) at the output was used to separate the laser radiation from the pump radiation [64].

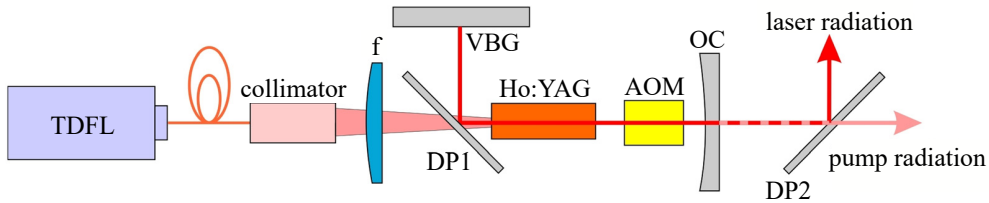


Fig. 12: Experimental setup of a Ho:YAG laser emitting at 2044 nm [64].

The laser characteristics were measured for a 96 mm long resonator in the free-running regime. A maximum output power of more than 9 W and a maximum slope efficiency of 59 % were obtained with an output mirror reflectivity of 10 %. In the Q-switching regime, a resonator of 115 mm length was used with an output mirror reflectivity of 20 %. Pulses with a maximum energy of 2.2 mJ, a minimum duration of 50 ns, and a maximum peak power of 44 kW were achieved at an acousto-optic modulator frequency of 2 kHz and a pump power of 17 W. The output radiation was linearly vertically polarised, and its spectrum was centred at 2044 nm in both regimes [64].

5.2 Thulium-doped fiber MOPA emitting at the wavelength of 2036 nm

Although the main focus of this thesis is on the generation of radiation using solid-state lasers, it is also necessary to highlight the research carried out by C. Roman et al. on a MOPA (Master Oscillator Power Amplifier) fibre laser emitting radiation at 2036 nm [65]. The laser system was composed of a seed laser (master oscillator) and a one-stage high-power amplifier (Fig. 13). The seed laser consisted of a double-clad thulium-doped fibre (TDF) that was pumped by two diodes at a wavelength of 793 nm. It also had two fibre gratings, one with high reflection (HR) of 99 % and the other with low reflection (LR) of 12 %. The seed laser produced radiation at a wavelength of 2036 nm and delivered a power of 10 W with a slope efficiency of 41 %. The high-power amplifier was composed of a mode field adapter (MFA) and a 7 m double-clad TDF pumped by 6 diodes through a pump combiner (PC). The amplifier produced an output power of 973 W with a pump power of 1640 W, giving a slope efficiency of 53 % at maximum output power [65].

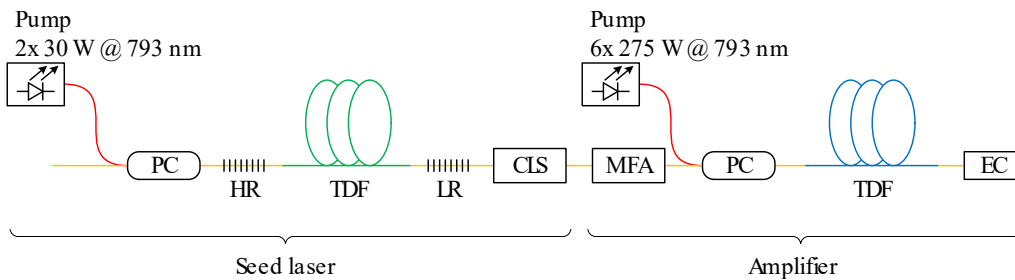


Fig. 13: Experimental setup of a MOPA fibre laser [65].

6 Experimental setup

This section of the thesis describes the optical elements used in the construction of the lasers, the equipment for measuring their output characteristics and the experimental setup schemes.

6.1 Active media

The following active media were available for the experimental part of this work: Tm:YAG, Tm:GGAG, Tm:YLF, Tm:YAP and Tm:KYW. Their basic parameters are summarised in Tab. 2. The Tm:YAG crystal was available in two variants. One of them is in the shape of a plate and was used for the spectroscopic characterisation of the material. The second crystal, which was used for laser construction, is in the form of a cylinder 7 mm long, of which 4 mm is the undoped part for cooling and 3 mm is the doped part. Only the Tm:YAP crystal has anti-reflective coatings. As the crystals Tm:YLF, Tm:YAP and Tm:KYW are birefringent, the experiments were performed for both polarisation of the pumping radiation.

Tab. 2: Parameters of the active media used in the experiments.

Active medium	Concentration of Tm ³⁺	Shape	Size	Anti-reflection coatings	Orientation
Tm:YAG	5 at. % Tm/Y	plan-parallel plate	thickness 0.813 mm	NO	-
Tm:YAG	4 at. % Tm/Y	cylinder	length 3 mm, diameter 3 mm	NO	-
Tm:GGAG	5.11 at. % Tm/Gd	plan-parallel plate	thickness 3.53 mm	NO	-
Tm:YLF	4 at. % Tm/Y	cylinder	length 6 mm, diameter 3 mm	NO	a-cut
Tm:YAP	4 at. % Tm/Y	cylinder	length 3 mm, diameter 3 mm	YES	a-cut
Tm:KYW	4.6 at. % Tm/Y	quadrilateral prism	length 2.5 mm, cross-section 3 mm×3 mm, end face tilt 1°	NO	N _g -cut

6.2 Resonators and optical elements

Semi-hemispherical resonators

First, a semi-hemispherical resonator² was constructed for each active medium. The experimental setup of this type of resonator is depicted in the Fig. 14. These resonators were composed of a flat pump mirror and a spherical output coupler. The parameters of all used mirrors are listed in the Tab. 3. In this type of resonator, the mirror M_a corresponds to the mirror M_1 from the table. For the output coupler M_b , two mirrors M_3 and M_4 were used. The length L of the resonator for each active medium was approximately 80 mm, but the exact length was adjusted for each measurement to achieve the highest possible power. The active medium was positioned approximately 3 mm after the pump mirror. The purpose of construction of this type of resonator was to characterize its output radiation in order to identify the most appropriate active media for constructing a laser with a volume Bragg grating and producing radiation at the wavelength of approximately 2035 nm. In the Fig. 15, an example of this type of constructed resonator with a Tm:GGAG crystal is shown.

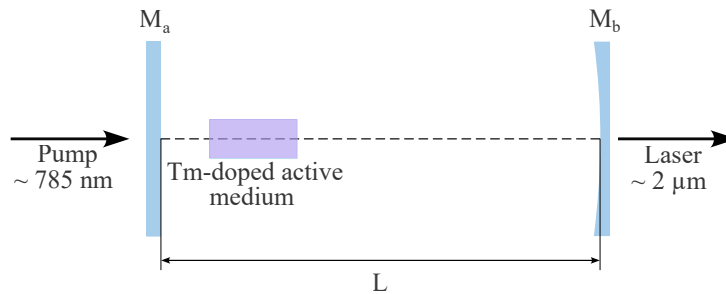


Fig. 14: Experimental setup of a laser with a semi-hemispherical resonator.

V-shaped resonators

The second type of resonator is shown in the Fig. 16. This V-shaped resonator was composed of flat mirror M_a , spherical output coupler M_b and folding mirror M_c . The mirror M_a also corresponds to the mirror M_1 from the Tab. 3. For the output coupler M_b , the mirrors M_3 and M_5 were used and the lengths L between the folding mirror and the mirror M_b were approximately 130 and 80 mm, or shorter in certain experiments. The folding mirror M_c , which is placed in the resonator at the angle of 50° , corresponds to the mirror M_2 . This resonator was constructed as

²The term “hemispherical resonator” is defined as a resonator with one flat mirror and one spherical mirror with a radius of curvature corresponding to the length of the resonator. As the resonators constructed in this experiment were shorter than the radius of curvature of the mirrors, they are described as “semi-hemispherical”.

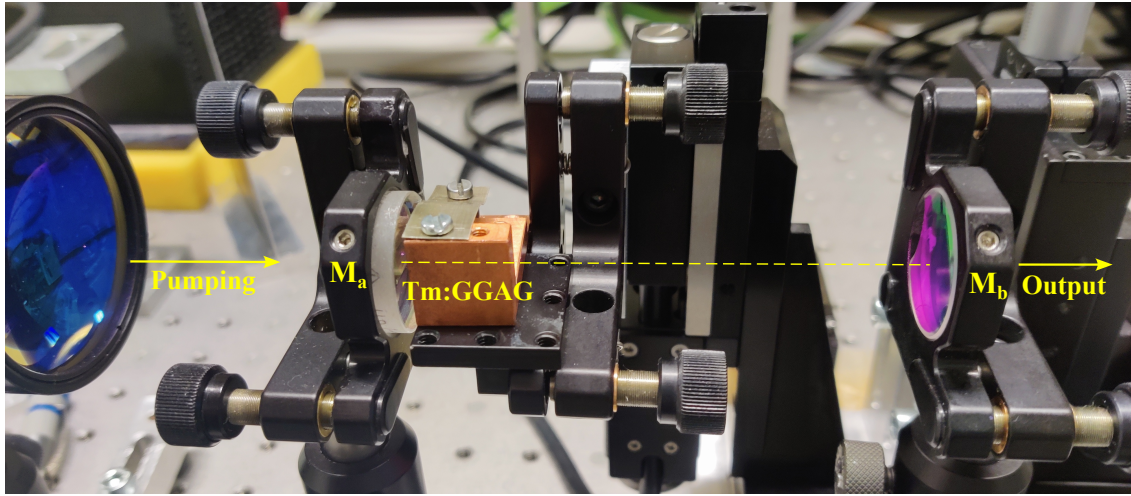


Fig. 15: Photo of the experimental arrangement of a laser Tm:GGAG with a semi-hemispherical resonator.

Tab. 3: Table of all mirrors used for the construction of resonators; r - radius of curvature, R - reflectivity, T - transmission.

Mirror	r	R/T
M ₁	∞ (flat)	HR @ 1.9-2.15 μm , HT @ 0.8/1.71 μm
M ₂	∞ (flat)	HR @ 2036 nm, HT @ 790+1700 nm, $\alpha=50^\circ$
M ₃	150 mm	R=97 % @ 2 μm
M ₄	150 mm	R=92 % @ 2 μm
M ₅	100 mm	R=99.8 % @ 2 μm

an intermediate step between the semi-hemispherical resonator and a resonator with a volume Bragg grating in order to detect changes in the output power and the wavelength of the emitted radiation caused by the presence of the mirror M_c. This type of resonator was also useful for

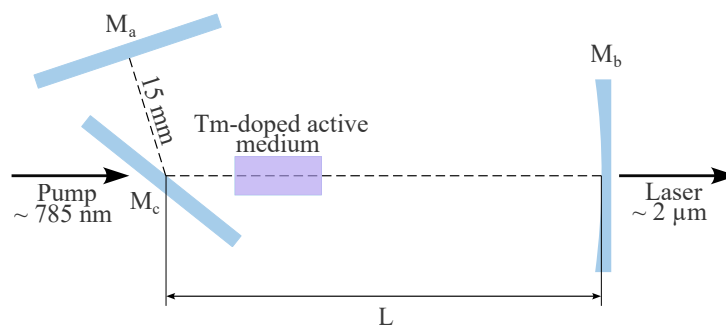


Fig. 16: Experimental setup of the second type of resonator.

easier setting of the resonator with the volume Bragg grating. An example of this resonator with a crystal Tm:YLF is shown in the Fig. 17.

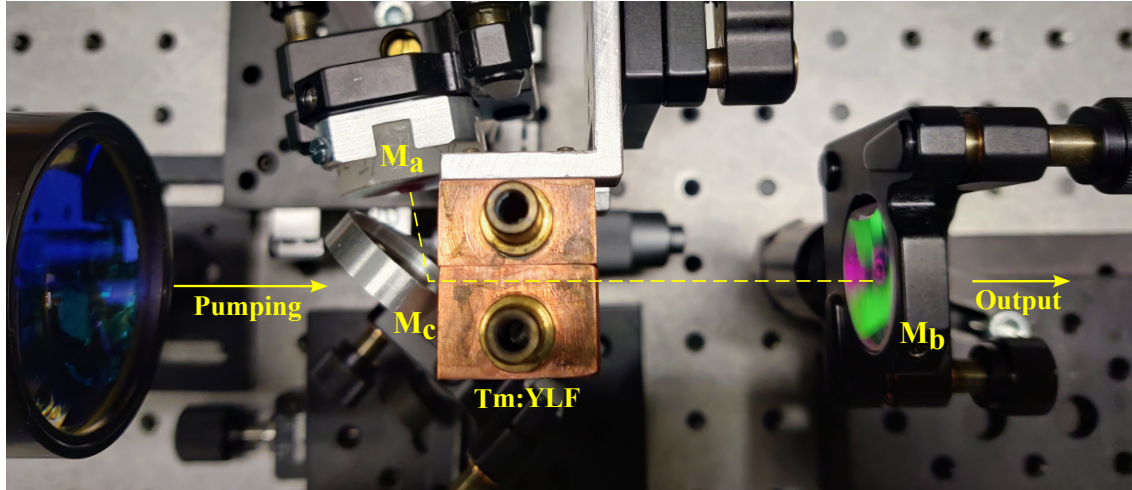


Fig. 17: Photo of the experimental arrangement of a laser Tm:YLF with a V-shaped resonator.

Resonators with VBG

The main goal of this thesis was to construct a laser emitting radiation at the wavelength of around 2035 nm. For adjusting the wavelength of the laser, a reflective volume Bragg grating RBG-2036-99 from OptiGrate (hereafter VBG) with a centre wavelength of 2036.2 nm and a spectral bandwidth (FWHM) of approximately 1 nm was used. Its dimensions are $6.5 \text{ mm} \pm 0.25 \text{ mm} \times 6.5 \text{ mm} \pm 0.25 \text{ mm}$, with a thickness of 4.1 mm and a grating tilt of <1.5 degrees in the glass medium. The diffraction efficiency of this grating is $>99 \%$. The grating is shown in the Fig. 18.

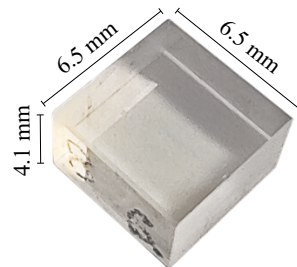


Fig. 18: Volume Bragg grating.

The Fig. 19 shows the resonator with the VBG, which replaced the mirror M_1 from the second type of the resonator. The other mirrors and lengths L remained the same as in the previous type

of resonator. In these experiments, the laser output was both behind the mirror M_b and behind the VBG. An example of the resonator with the VBG is shown in the Fig. 20.

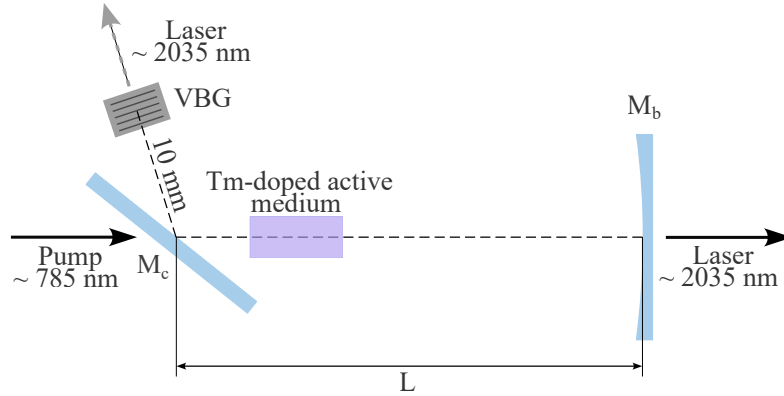


Fig. 19: Experimental setup of the third type of resonator.

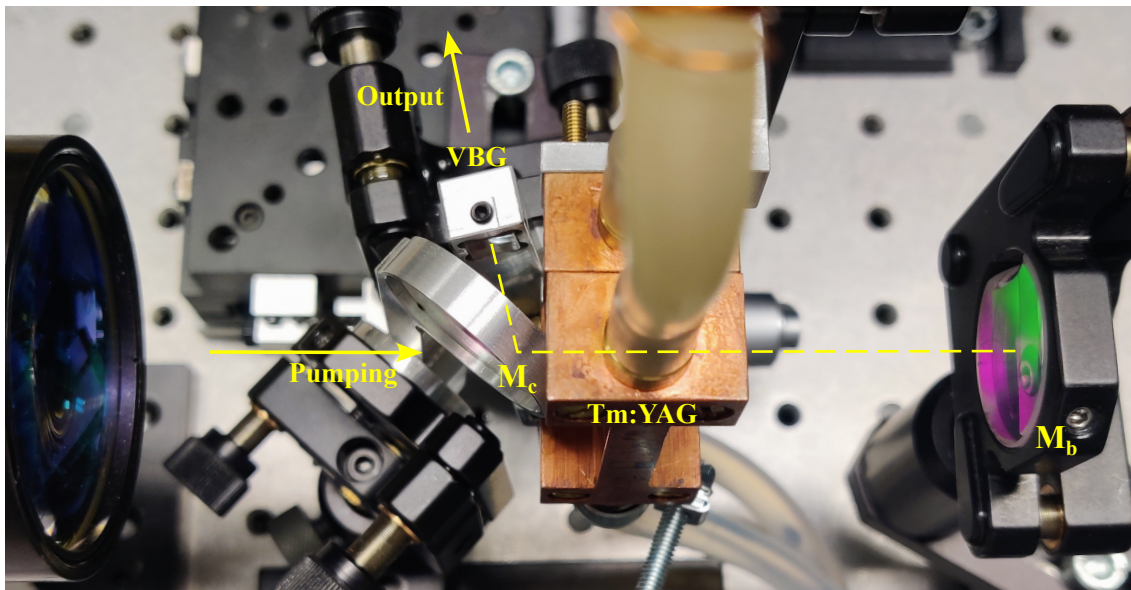


Fig. 20: Photo of the experimental arrangement of the laser Tm:YAG with VBG.

Tm:YAG with VBG

Based on the results of the laser measurements with the VBG, it was decided to further improve the measurements using only the Tm:YAG active medium. The improvement consisted especially in the cooling of the active medium. It was cooled by water at the temperatures of 10, 15 and 20 °C.

Further experiments as CW regime, construction of a short resonator and Q-switching with the active medium Tm:YAG were also performed. The resonator constructed for the CW regime

is also depicted in Fig. 19 with the use of the mirror M_5 and the length $L = 80$ mm. For the short resonator, mirror M_5 was chosen as the pumping mirror, while a VBG was used as the output coupler. The length of the resonator was set to $L=17.5$ mm. Fig. 21 presents the experimental arrangement of the resonator and Fig. 22 shows a photo of this experiment.

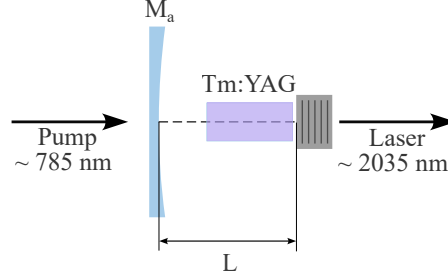


Fig. 21: Experimental setup of the short semi-hemispherical resonator with a VBG.

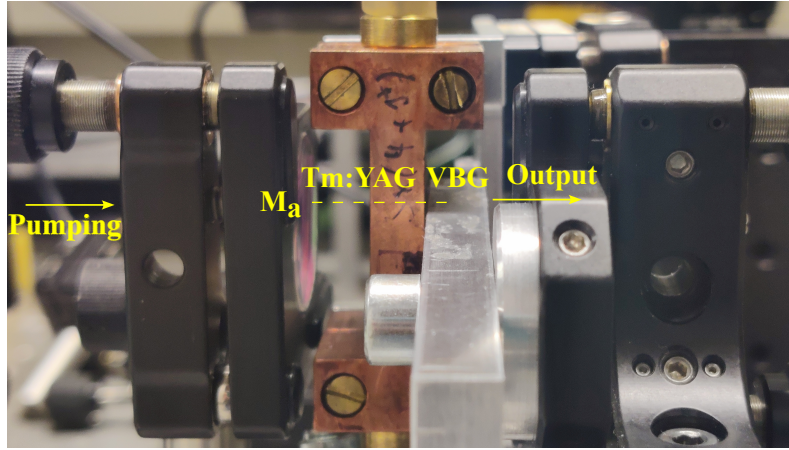


Fig. 22: Photo of the experimental setup of the short semi-hemispherical resonator with VBG.

For the Q-switching, the resonator is shown in the Fig. 23. The mirror M_b corresponds also to the mirror M_5 and the length L remained 80 mm. The Q-switching was reached by use of a Pockels cell made of LiNbO_3 , which was 25 mm long with a cross-section of 6 mm \times 6,5 mm with anti-reflective coatings for the wavelength of 2 μm . The voltage on the Pockels cell was set up by a high-voltage power supply with the maximum of 6 kV. The switching of this source was controlled by a pulse generator Zopan PGP-5A. A photo of the constructed resonator for the Q-switching regime is shown in the Fig. 24.

In the Q-switching regime, it is necessary to set an appropriate voltage on the Pockels cell. In this experimental arrangement, the voltage was applied perpendicularly to the direction of propagation of the beam. For its value $V_{1/4}$, a following relation can be written [7]:

$$V_{1/4} = \frac{\lambda d}{4r_{22}n_o^3l}, \quad (12)$$

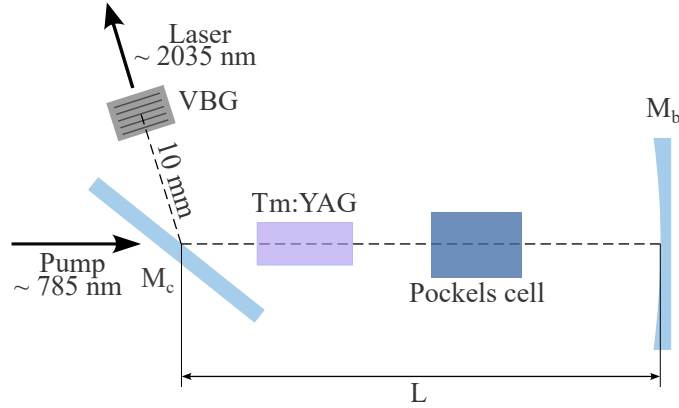


Fig. 23: Experimental setup of the resonator constructed for the Q-switching.

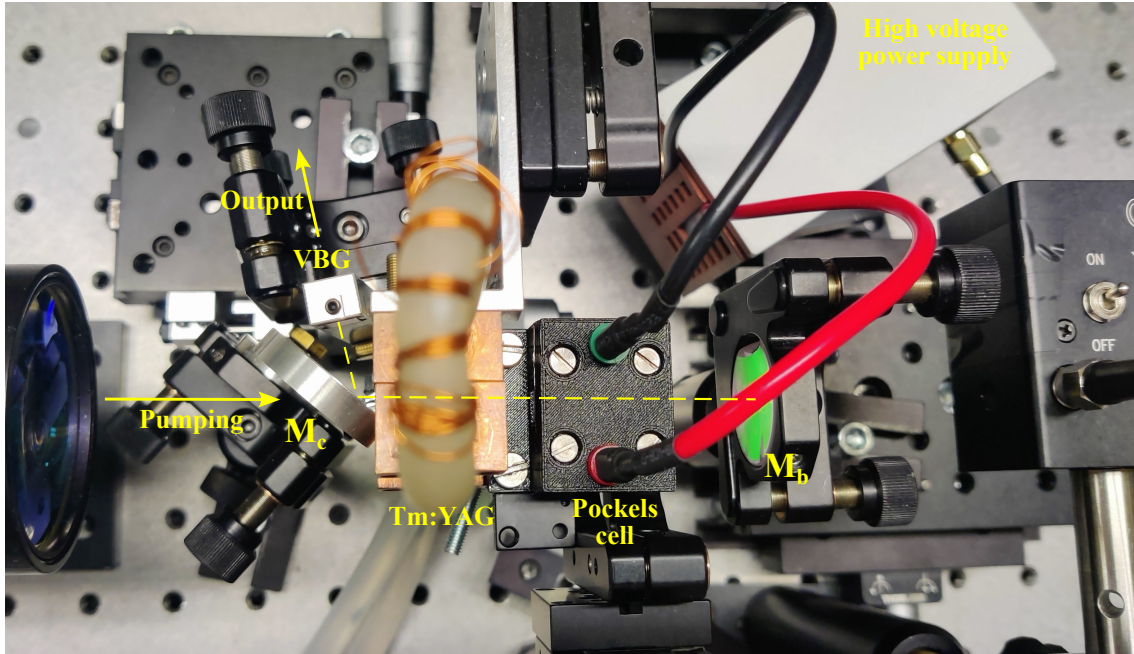


Fig. 24: Photo of the experimental arrangement of a Q-switched laser Tm:YAG with a VBG.

where λ is a wavelength of the radiation, d is the distance between electrodes, r_{22} is an electro-optic coefficient, n_o is an ordinary refractive index of the crystal and l is its length. For this experiment, these constants are listed in the Tab. 4. The calculated value of the voltage is $V_{1/4}=2.22$ kV, whereas the actual value of the voltage set on the Pockels cell is 2.517 kV. The mirror M_c serves as a polarizer.

Measured reflectivity spectra of all used mirrors as well as the transmission spectra of the VBG and the Pockels cell are presented in the chapter 7.2. The measurement was performed using the Shimadzu UV-3600 spectrophotometer with a spectral range of 185-3200 nm.

Tab. 4: Table of constants for calculation of a voltage applied on the Pockels cell.

Constant	Value
λ	2035 nm
d	6 mm
l	25 mm
n_o @ 2035 nm	2.1956
r_{22} @ 2100 nm	5.2 pm/V

6.3 Pumping

For the longitudinal pumping of thulium-active media, a laser diode LIMO HLU30F400-790 (hereafter LIMO) was used. Its parameters are given in Tab. 5. The radiation of the diode was guided into a fibre with a diameter of 400 μm and then focused into the active medium by 1:1 optics consisting of two achromatic doublets with a focal length $f = 75$ mm. Measured characteristics of this laser diode are presented in the section 7.1.

The wavelength of emitted radiation of the laser diode was measured by a Stellarnet Blue-Wave spectrometer with a spectral range of 200-1150 nm. The power of the laser diode LIMO as well as the absorbed pump power was measured using a Thorlabs PM100A power meter and a Thorlabs S425C-L sensor covering the spectral range of 0.19 to 20 μm and power levels ranging from 2 mW to 50 W. The temporal evolution of the diode radiation was recorded using a FDS1010 Si photodiode suitable for the wavelength range of 350-1100 nm with a 65 ns rise/fall time. The signal was displayed at the Tektronix TDS3052B oscilloscope with a bandwidth of 500 MHz and a sampling rate of 5 GS/s.

Tab. 5: Parameters of the laser diode LIMO provided by the manufacturer.

Laser diode	LIMO HLU30F400-790
CW output power	30 W
Center wavelength	790 nm
Spectral width	<5 nm
Temperature drift of λ	0.3 nm/K
Threshold current	8 A
Typical operation current	48 A
Typical slope efficiency	0.75 W/A
Operation temperature	15-30 $^{\circ}\text{C}$
Fibre core diameter	400 $\mu\text{m} \pm 2\%$

6.4 Description of spectroscopic measurements

The transmission spectra of the active media and the mirrors were measured using a Shimadzu UV-3600 spectrophotometer with a spectral range of 185-3200 nm. For birefringent active media such as Tm:YAP, Tm:YLF and Tm:KYW, an absorption linear polarizer from Edmund Optics was placed in the spectrophotometer before the measurement and the transmission spectra were measured for both perpendicular polarisations of the incident radiation. The absorption coefficient α was then calculated from the transmittance $T = \frac{I}{I_0}$ using the Lambert-Beer law for attenuation in the material:

$$I = I_0 e^{-\alpha l}, \quad (13)$$

where I_0 is the intensity of the incident radiation on the material, I is the intensity of the transmitted radiation, and l is the length of the material.

For measuring fluorescence spectra, the active media were pumped by a diode LIMO in CW regime at a wavelength of 785 nm and the spectra were measured using a spectrometer StellarNet Red-Wave with a spectral range of 1500-2200 nm and a resolution of 2.8 nm. In the case of anisotropic media, the polarizer from Edmund Optics was placed in front of the spectrometer and the fluorescence spectra were measured for both polarisations.

The fluorescence lifetime was measured using the confocal method in order to reduce the reabsorption of radiation [66]. The experimental setup is shown in Fig. 25. The pump radiation from the diode was focused into the active medium. The fluorescence radiation from the active medium was then focused onto a Thorlabs FD05D photodiode that has a spectral range of 0.9-2.6 μm . The measurements were taken using a Tektronix TDS3052B oscilloscope with a bandwidth of 500 MHz and a sampling rate of 5 GS/s. A 100 μm pinhole was mounted on the photodiode

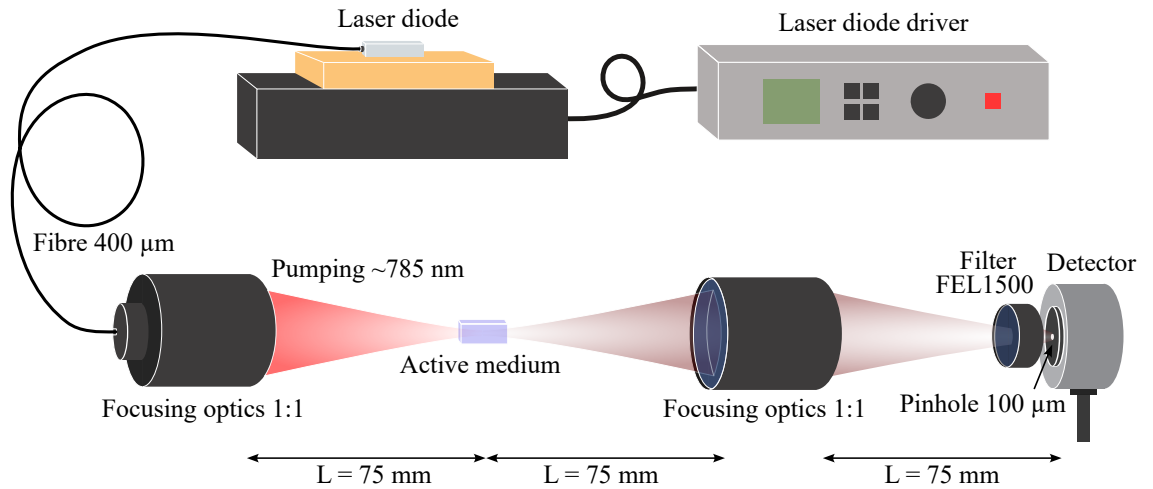


Fig. 25: Experimental setup for a fluorescence lifetime measurement.

and a filter (FEL 1500) was placed in front of the detector to remove the pump radiation from the beam. The temporal evolution of the fluorescence intensity after switching off the pump radiation can be described by an equation

$$I(t) = I_0 e^{-t/\tau_f}, \quad (14)$$

where I_0 is the initial fluorescence intensity. The fluorescence lifetime τ_f was determined by fitting the recorded temporal radiation profile with this function.

6.5 Description of laser measurements

Measurements of the laser characteristics were performed for the thulium-doped active media listed in the section 6.1. Different settings of the diode were chosen for the pumping. Most of the measurements were performed for different temperatures of the diode in order to find the optimum pumping wavelength. For some active media, various pump pulse lengths were set.

For the Tm:GGAG active medium, it was necessary to scan the sample in order to identify the location where the laser radiation with the highest power is generated due to its inhomogeneity. The scanning process utilized two stepper motors which were controlled by the 8SMC5-USB Stepper & DC Motor Controller from Standa. The XILab software was used to set the motor positions, and scanning was performed using a Matlab script. The experimental setup is shown in the Fig. 26.

The photodiode PDA30G-EC, suitable for the spectral range of 1-2.9 μm , and the above mentioned oscilloscope Tektronix were used to record the output radiation of the laser. The output power was measured using a wattmeter PM100A and a power probe Thorlabs S401C with a filter FEL1500 with a transmission in the range of 1500-2200 nm and a transmittance of about 70 %. The camera Spiricon Pyrocam IV was used to record the beam profile. This camera is suitable for a wavelength range of 1.06 μm - 10 μm , has a chip size of 25.6 mm \times 25.6 mm and a pixel size of 80 μm \times 80 μm . The laser emission spectrum was also measured using the StellarNet Red-Wave spectrometer, which has previously been employed for the measurement of fluorescence spectra. However, the spectrometer resolution of 2.8 nm does not permit the precise measurement of the shape of laser emission spectra. Nevertheless, it is possible to determine their peaks.

The absorbed power was calculated as the difference on measured pump power incident on crystal and unabsorbed pump power after passing the crystal, corrected for Fresnel losses at the crystal/air interface. For birefringent crystals, the laser characteristics were measured for both perpendicular orientations of crystals with respect to the polarisation of the pump radiation.

During the Q-switching regime, the energy of a pulse was measured by an energy probe Coherent J-10MB-LE with a responsivity of 1.306×10^4 V/J. For recording a temporal profile of pulses, a fast photodiode ET-5000 from Electro-Optics Technology with a rise time of 28 ps suitable for

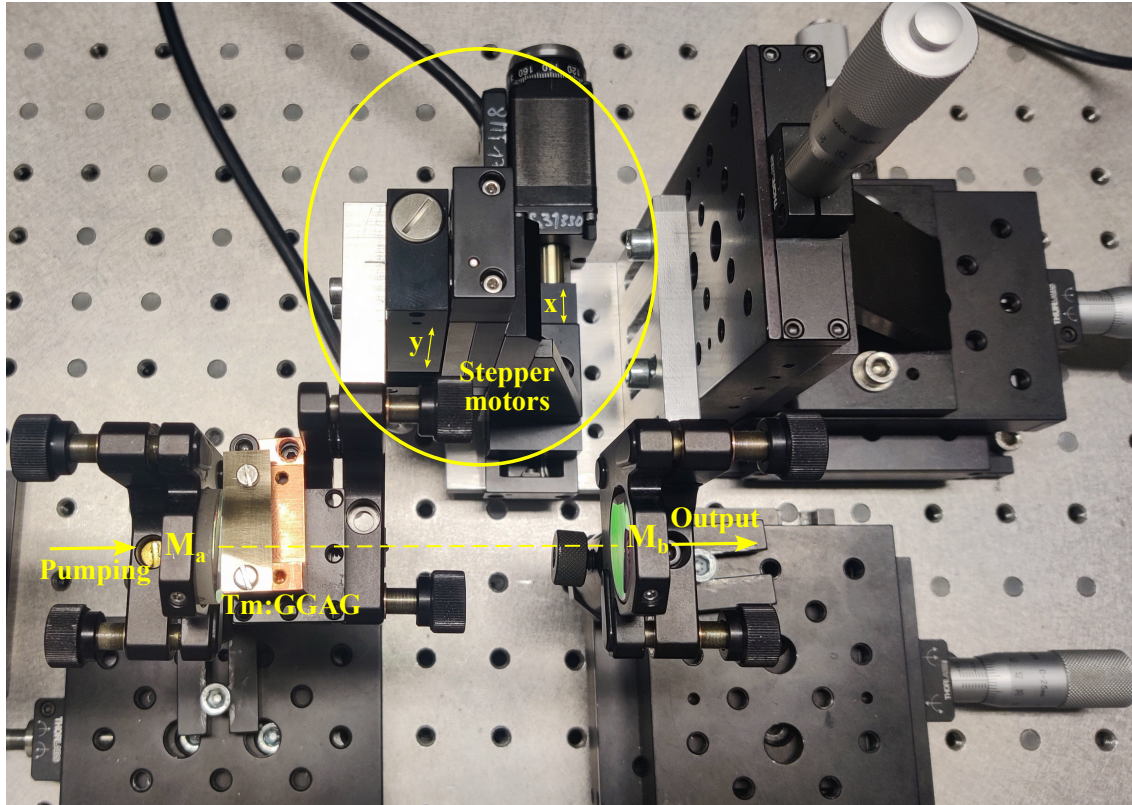


Fig. 26: Photo of the experimental arrangement of a laser Tm:GGAG with stepper motors for scanning.

a spectral range 900-2100 nm was used. The recorded signal was displayed at an oscilloscopes Tektronix DPO 4104B-L with a 1 GHz bandwidth and a sampling rate of 5GS/s and LeCroy SDA 813Zi with a bandwidth of 13 GHz and a sampling rate of 40 GS/s. Other characteristics as the spectrum of the output radiation or the beam profile were measured with the same devices as during the free-running regime.

7 Experimental results

7.1 Characteristics of the pumping diode

A mean output power and a wavelength of the diode radiation were measured as a function of diode current for pulses of 5 ms (Fig. 27) and 10 ms (Fig. 28), both with a duty cycle of 10 %. The emitted radiation was partially vertically polarised when the fibre loop was twisted once and positioned horizontally. The ratio of the vertical to horizontal polarisation components in the diode output radiation, as determined by a polarizer, was approximately 3:1.

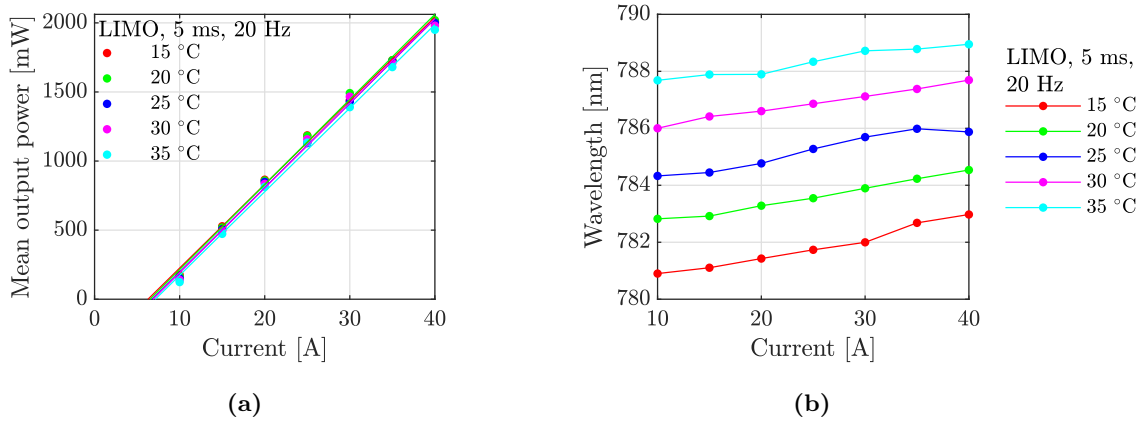


Fig. 27: Mean output power (a) and wavelength (b) as a function of diode current for a 5 ms current pulse and for different diode temperatures.

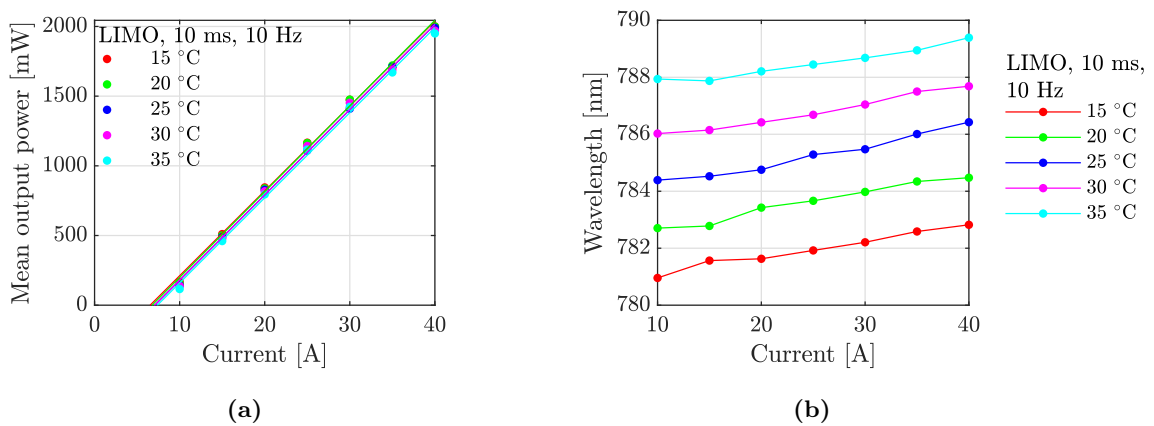


Fig. 28: Mean output power (a) and wavelength (b) as a function of diode current for a 10 ms current pulse and for different diode temperatures.

7.2 Reflectivity and transmission spectra of optical elements

The transmission spectra of all the mirrors used to construct the resonators were measured and subsequently recalculated into reflectivity spectra. Fig. 29 shows the reflectivity spectrum of pumping mirror M_1 for both the pumping and laser wavelength regions. Fig. 30 presents the spectra of the output mirrors M_3 and M_4 for the laser wavelength. The spectrum of output mirror M_5 , which was also used as a pumping mirror in the last experiment, is presented in Fig. 31, displaying both ranges.

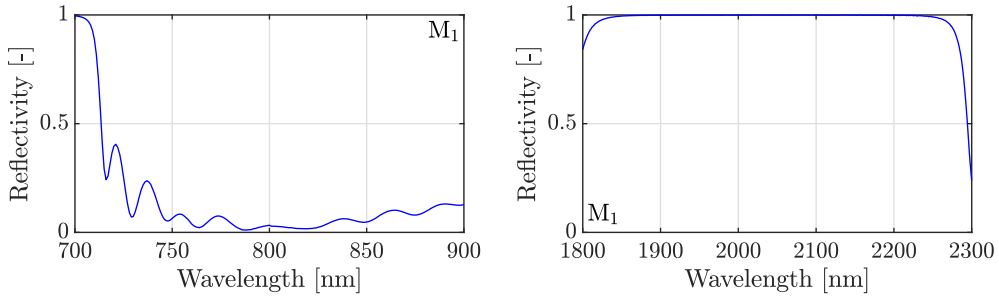


Fig. 29: Reflectivity of the mirror M_1 .

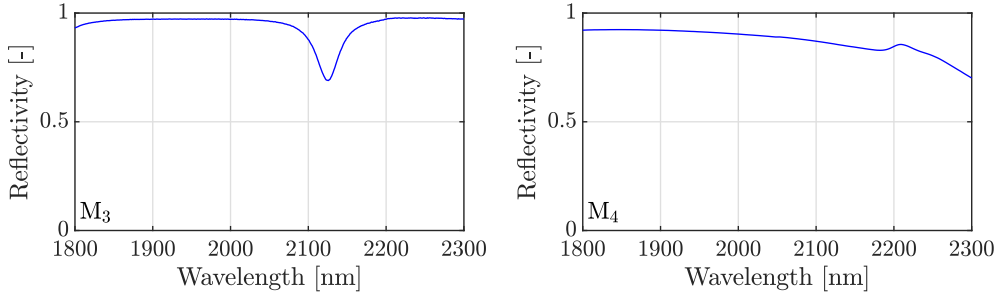


Fig. 30: Reflectivity of the mirrors M_3 and M_4 .

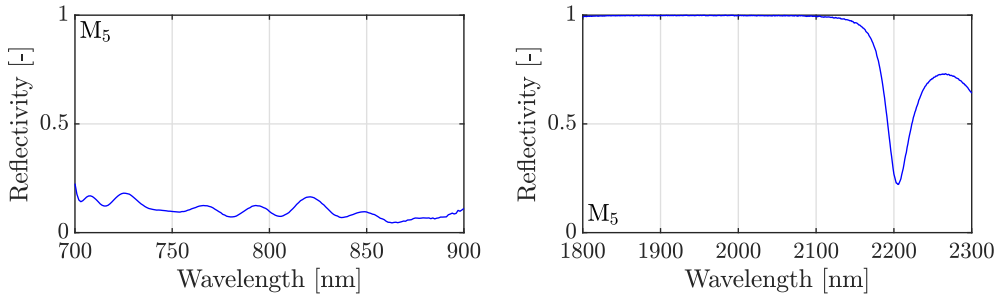


Fig. 31: Reflectivity of the mirror M_5 .

Fig. 32 shows the reflectivity dependence of mirror M_2 at an incidence angle for a wavelength of 2036 nm and for both radiation polarisations, s and p. A tunable laser, EKSPLA NT 252, was employed as the source of polarised radiation at the specified wavelength. The reflectivity was determined for the given angle of incidence as the ratio of the mean power of the reflected and incident radiation.

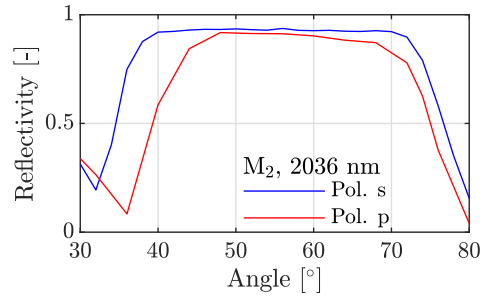


Fig. 32: Reflectivity of mirror M_2 with respect to the angle of incidence for wavelength 2036 nm for polarisations s and p.

The transmission spectrum of the VBG was measured over a wide range from 700 to 2300 nm and then in more detail in the narrower range from 2030 to 2040 nm (Fig. 33). The transmission spectrum of the Pockels cell used for Q-switching was also measured (Fig. 34).

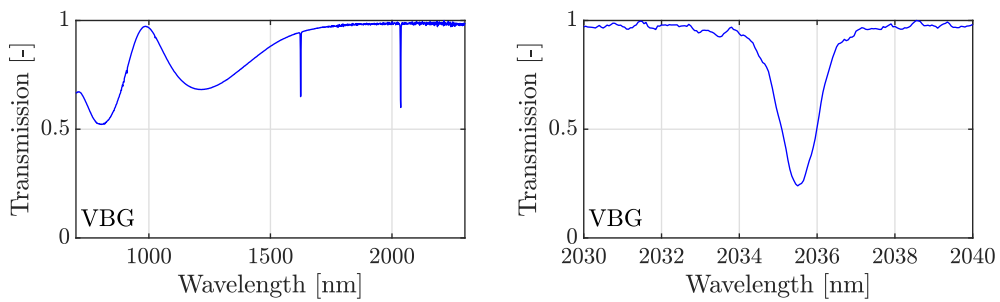


Fig. 33: Transmission spectrum of the VBG.

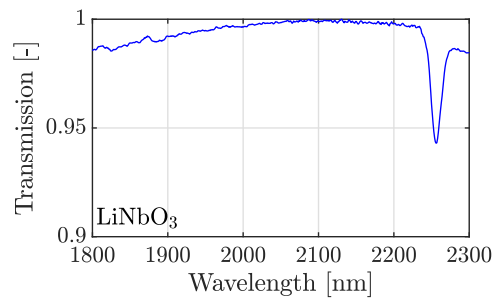


Fig. 34: Transmission spectrum of anti-reflective coated LiNbO₃ crystal used for Pockels Cell.

7.3 Results of spectroscopic measurements

7.3.1 Absorption spectra

Fig. 35-39 show the absorption spectra of Tm:YAG, Tm:GGAG, Tm:YLF, Tm:YAP, and Tm:KYW crystals. The spectra were calculated from the measured transmission spectra using the Lambert-Beer law (13). Two different ranges of possible pumping regions, around 780 nm and around 1700 nm, corresponding to pump and lasing regions of Tm^{3+} ions, are presented. The polarisation-resolved spectra are plotted for the birefringent crystals Tm:YLF, Tm:YAP and Tm:KYW.

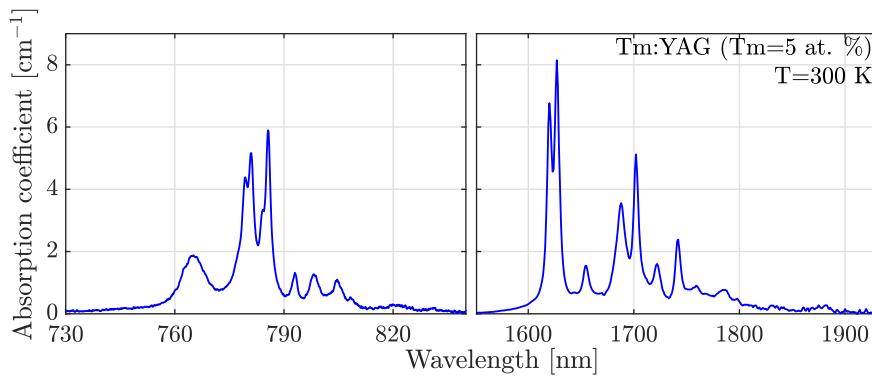


Fig. 35: Absorption spectrum of Tm:YAG.

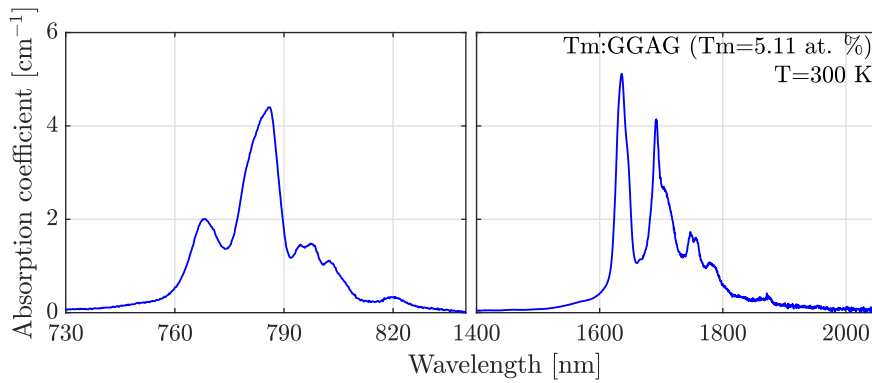


Fig. 36: Absorption spectrum of Tm:GGAG.

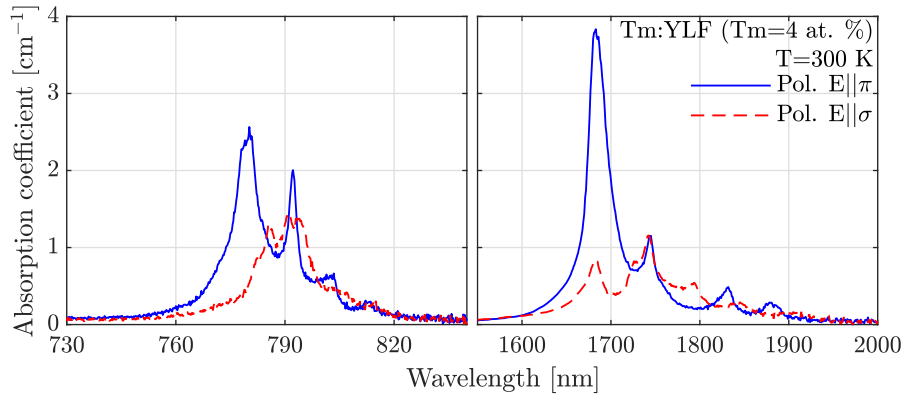


Fig. 37: Absorption spectrum of Tm:YLF.

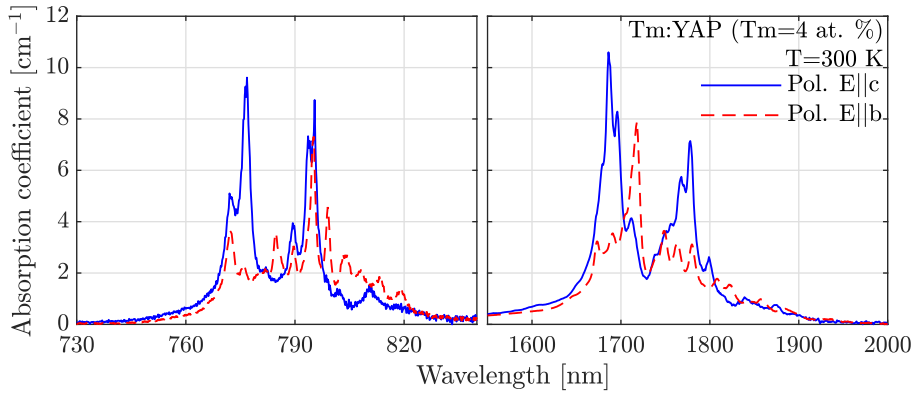


Fig. 38: Absorption spectrum of Tm:YAP.

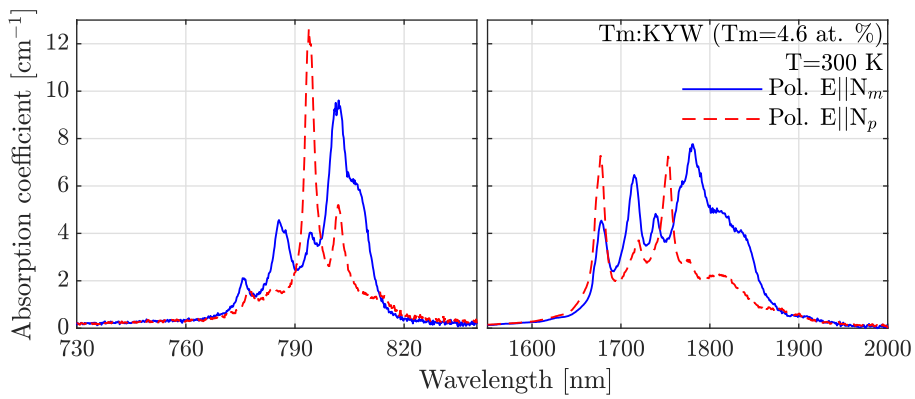


Fig. 39: Absorption spectrum of Tm:KYW.

7.3.2 Fluorescence spectra

Figures 40-42 depict the fluorescence spectra of the crystals measured by the StellarNet Red-Wave spectrometer. The graphs indicate that the Tm:YAG and Tm:GGAG crystals are more suitable for generating radiation around 2035 nm than the other crystals, as they exhibit relatively high fluorescence in this region.

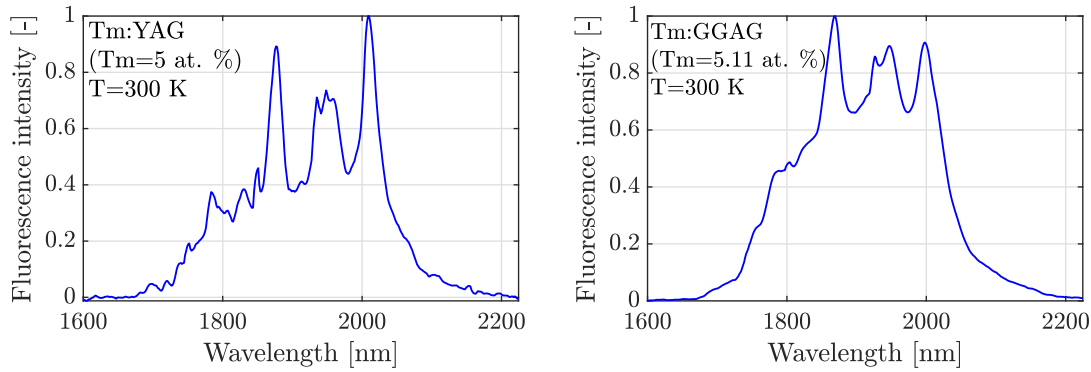


Fig. 40: Fluorescence spectra of Tm:YAG and Tm:GGAG.

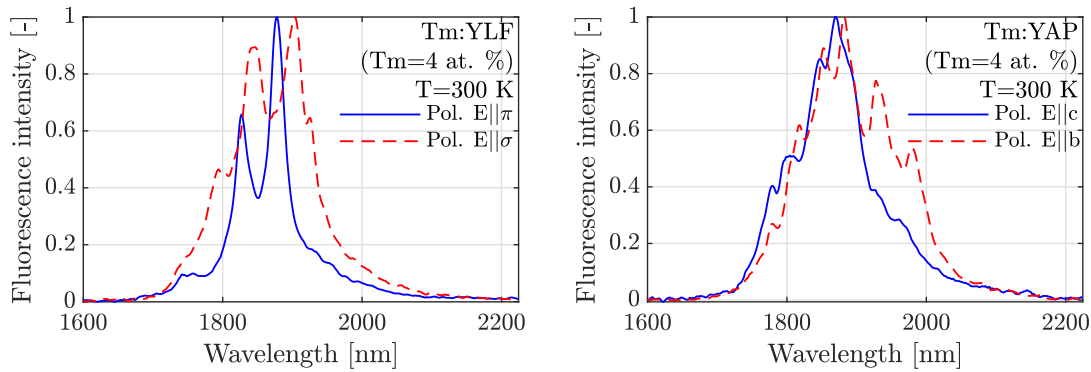


Fig. 41: Fluorescence spectra of Tm:YLF and Tm:YAP.

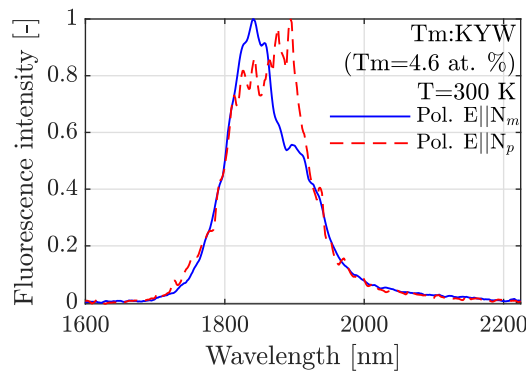


Fig. 42: Fluorescence spectra of Tm:KYW.

7.3.3 Calculation of emission cross-sections

The fluorescence spectra were subsequently used to calculate the emission cross-section using the Füchtbauer-Ladenburg equation [66]

$$\sigma_e(\lambda) = \frac{\lambda^5}{8\pi f_j \tau_r c n^2} \frac{I(\lambda)}{\int I(\lambda) \lambda d\lambda}, \quad (15)$$

where $I(\lambda)$ is the fluorescence intensity at wavelength λ , f_j is the fraction of the population on the upper level j given by the Boltzmann distribution (set to 1), τ_r is the radiative lifetime, c is the speed of light in vacuum, and n is the refractive index of the active medium.

For the calculation of the emission cross-sections, the parameters from Tab. 1 (page 19) were employed. However, the maxima of the calculated emission cross-sections were higher than the values reported in the literature. It is therefore possible that the utilized radiative lifetimes are shorter than they are in reality, which would result in an increase in the emission cross-section. To overcome this problem, the spectra were multiplied by a constant factor so that the maxima of the emission cross-sections corresponded to those reported in the literature (given also in the Tab. 1). From these spectra, it is possible to determine the values beyond the known maxima. Fig. 43 shows the calculated emission cross-sections as a function of wavelength for all active media. In the case of birefringent crystals, the measured fluorescence spectra for two individual orientations were averaged to calculate the emission cross-section. As the radiative lifetime and emission cross-section of the Tm:GGAG active medium are not known, a fluorescence lifetime of 11.6 ms, as reported in the literature, was employed for the calculation.

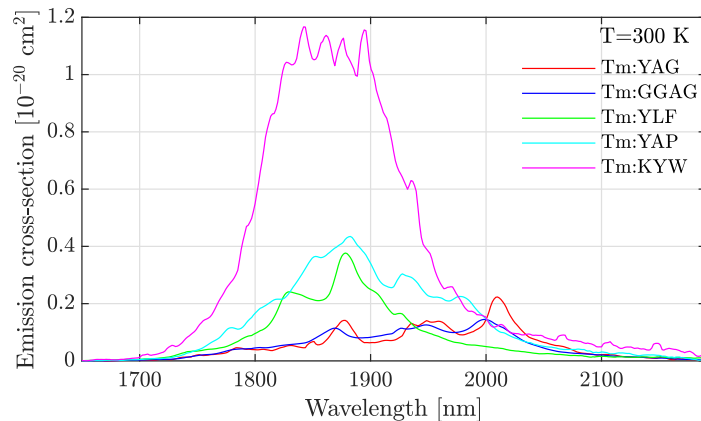


Fig. 43: Emission cross-sections of the thulium-doped active media.

7.3.4 Fluorescence lifetimes

Fig. 44-46 show the recorded temporal profiles of fluorescence intensity for each crystal after switching off the pump radiation. The data are fitted with the function (14). The fluorescence lifetimes of the transition ${}^3F_4 \rightarrow {}^3H_6$, provided in the respective graphs, were determined from the fit parameters.

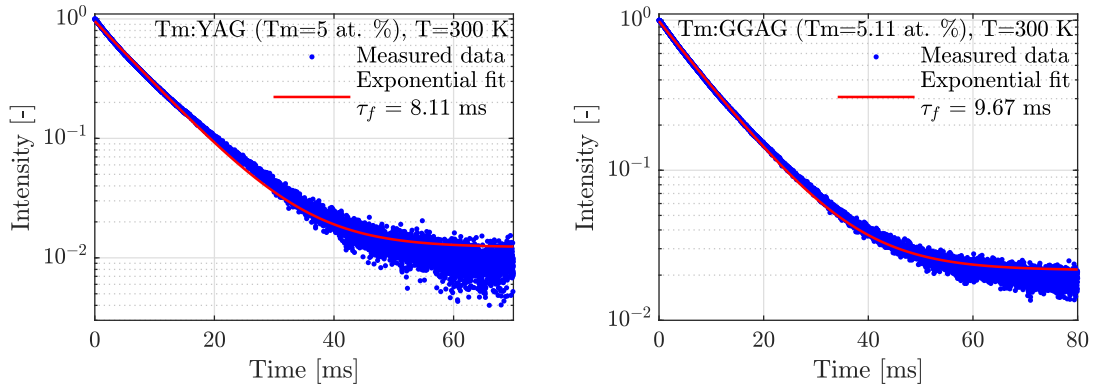


Fig. 44: Fluorescence decay of Tm:YAG and Tm:GGAG.

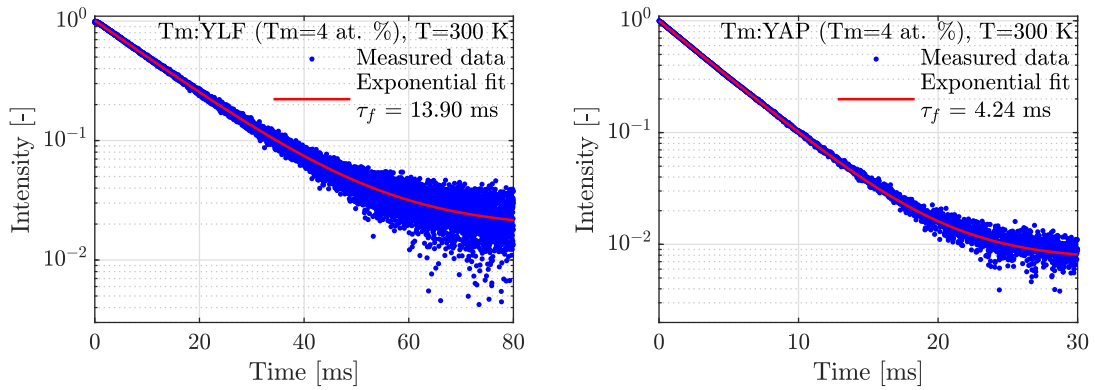


Fig. 45: Fluorescence decay of Tm:YLF and Tm:YAP.

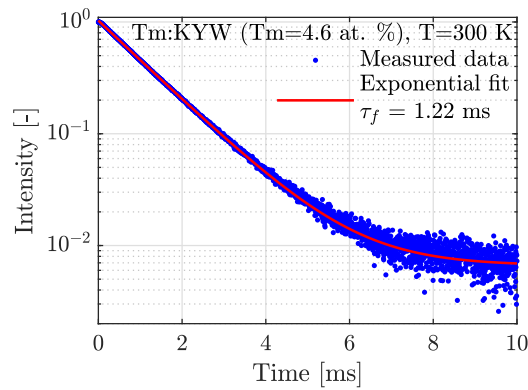


Fig. 46: Fluorescence decay of Tm:KYW.

7.3.5 Evaluation of spectroscopic measurements

Based on the knowledge of the emission cross-section σ_e and the fluorescence lifetime τ_f , the threshold power of the laser P_{th} can be calculated according to the equation [7, p. 120]:

$$P_{th} = \left(\frac{\delta - \ln R}{2} \right) \frac{Ah\nu_L}{\eta\sigma_e\tau_f}, \quad (16)$$

where δ are losses in the resonator, R is the reflectivity of the output mirror, A is the cross-section of the active medium, h is the Planck constant, ν_L is the frequency of the laser radiation, and η is the product of all efficiency factors. In this equation, it can be seen that the threshold power of the laser is inversely proportional to the product of σ_e and τ_f .

Fig. 47 shows the dependence of the product $\sigma_e \cdot \tau_f$ on the wavelength for all active media. The emission cross-sections were calculated in section 7.3.3, and the fluorescence lifetimes were obtained from the fit parameters in section 7.3.4. The graph indicates that the laser Tm:YAG achieves the highest value of the product in the wavelength region around 2035 nm. Therefore, it should have the lowest threshold power. The laser Tm:GGAG follows closely behind. The lasers Tm:YLF and Tm:YAP follow in order, with the laser Tm:KYW exhibiting the lowest values of the product $\sigma_e \cdot \tau_f$, thus demonstrating the highest expected threshold power.

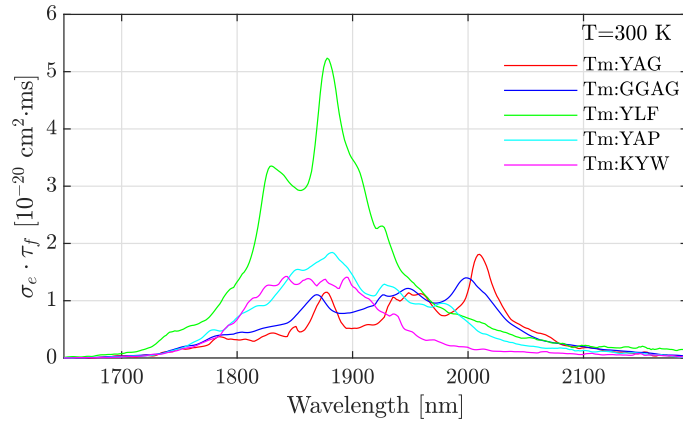


Fig. 47: Calculated product $\sigma_e \cdot \tau_f$ for the thulium-doped active media.

7.4 Laser characteristics

7.4.1 Lasers with semi-hemispherical resonator

For each of the lasers with semi-hemispherical resonator, Tm:YAG, Tm:GGAG, Tm:YLF, Tm:YAP, and Tm:KYW, the power characteristics, emission spectra, and beam profiles of the generated laser radiation were measured. The crystals were pumped with 10 ms or 5 ms long pulses with a duty cycle of 10 %. Based on the position of the absorption peaks in chapter 7.3.1, several pump wavelengths near the absorption peak were tested for each active medium. However, the tuning of the pump wavelength was constrained by the operation temperature range of the diode to prevent its damage. In the case of birefringent crystals, the active media were pumped in the two perpendicular orientations with respect to the partial vertical polarisation of the diode radiation. This section presents the power characteristics of individual lasers, followed by a comparison of the spectra of the generated radiation, and finally, a summary of the results for the lasers with semi-hemispherical resonator.

7.4.1.1 Tm:YAG laser

The dependence of the mean output power of the Tm:YAG laser on the absorbed power is shown in Fig. 48a for the 97 % output mirror and in Fig. 48b for the 92 % output mirror. In the case of 97 % reflectivity mirror, different wavelengths of the pump radiation were selected. From the graph, it can be observed that the highest power was achieved for 10 ms pump pulses at a wavelength of 786 nm, reaching 265 mW. In this case, the highest slope efficiency of 19.4 % was also achieved. When using a more open output mirror, the mean output power decreased to 75 mW, and the slope efficiency decreased to 9.5 %. Beam profiles for maximum output power are also depicted in the graphs. In both cases, the laser emitted radiation in the fundamental

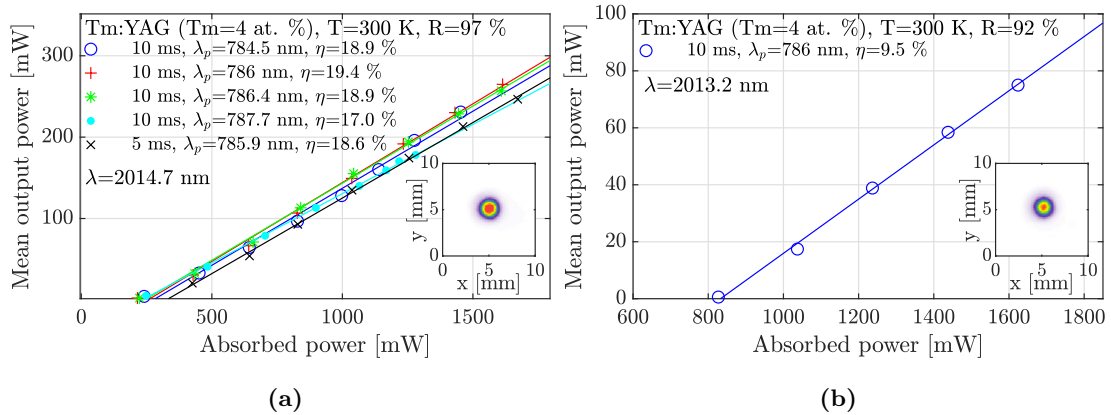


Fig. 48: Characteristics of the Tm:YAG laser with a 97 % reflectivity (a) and a 92 % reflectivity (b) output mirror.

transverse mode TEM_{00} .

7.4.1.2 Tm:GGAG laser

In contrast to the other crystals, it was necessary to scan the Tm:GGAG active medium due to its non-homogeneity. This scanning helped determine the optimal position for the laser generation in the crystal. During this process, the crystal was pumped with 5 ms pulses at a frequency of 20 Hz at a wavelength of 786.4 nm. The output power of the generated laser radiation was measured depending on the position in the crystal. Fig. 49a displays the scan of the entire active medium with a step size of 0.2 mm in both horizontal and vertical directions. The red areas on the graph indicate higher output power compared to the blue areas. Following this, the area around the position $x=2$ mm and $y=3$ mm, where the radiation has the highest power, was more accurately scanned. Fig. 49b shows the scan with a step size of 0.05 mm in both directions. Laser experiments were then performed with the crystal positioned where the highest power was measured, i.e. at $x=1.65$ mm and $y=3.3$ mm.

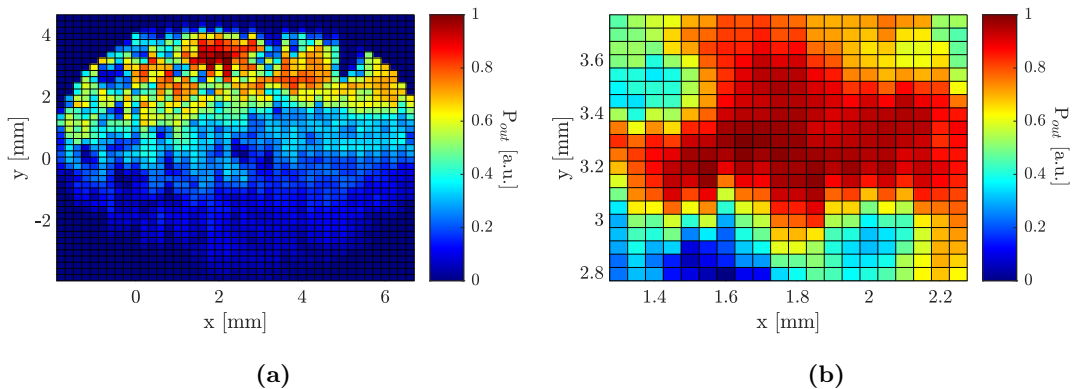


Fig. 49: Scan of the entire Tm:GGAG crystal (a) and a detailed view of a position of a maximum output power (b). P_{out} - mean output power of the laser radiation normalised to the maximum value.

The generation of laser radiation was achieved with this crystal only for the mirror with a reflectivity of 97 %. As can be seen in the Fig. 50, higher powers and slope efficiencies were achieved with a pumping pulse length of 5 ms and a repetition rate of 20 Hz. The maximum measured mean output power reached 142 mW with a slope efficiency of 11.2 % for a pumping wavelength of 785.9 nm. The laser beam mode approached the fundamental transverse mode TEM_{00} .

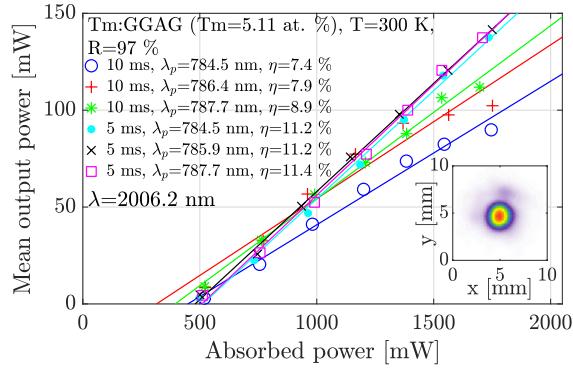


Fig. 50: Characteristics of the Tm:GGAG laser with an output coupler with a reflectivity of 97 %.

7.4.1.3 Tm:YLF laser

Starting with the first of the birefringent crystals, Tm:YLF, laser characteristics were measured for both pump beam polarisations and for both output mirrors with reflectivities of 97 % and 92 %. The pump pulse duration was set to 10 ms. In the case of the 97 % reflectivity mirror, better results were achieved for the $E||\pi$ pump polarisation (Fig. 51a). The maximum average output power reached 317 mW for a pump wavelength of 784.6 nm, with a slope efficiency of 37.5 %. For the $E||\sigma$ pump polarisation, the maximum average output power was 272 mW, with a slope efficiency of 31.9 % for a pump wavelength of 784.5 nm (Fig. 51b).

When using the more open mirror with a reflectivity of 92 %, the results for both pump polarisations were very similar. For the $E||\pi$ polarisation, the maximum average output power reached 300 mW, with a slope efficiency was 40.8 % for a pump wavelength of 784.5 nm (Fig. 52a). For the $E||\sigma$ polarisation, the results were slightly better, with a maximum power of 305 mW and

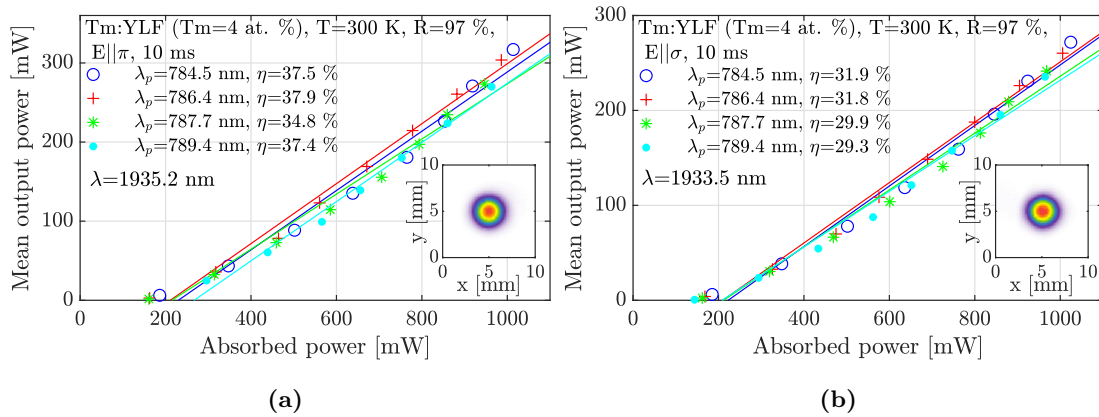


Fig. 51: Characteristics of the Tm:YLF laser with a 97 % reflectivity output mirror for a polarisation $E||\pi$ (a) and $E||\sigma$ (b).

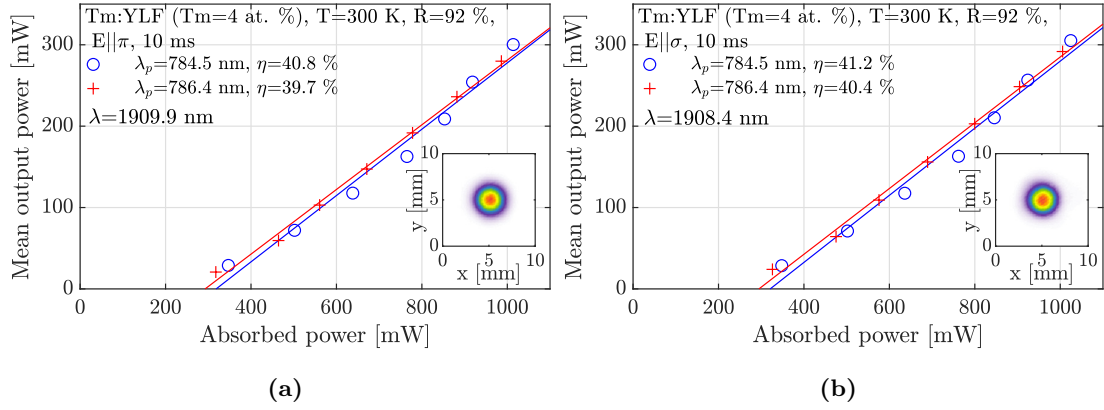


Fig. 52: Characteristics of the Tm:YLF laser with a 92 % reflectivity output mirror for a polarisation E|| π (a) and E|| σ (b).

a slope efficiency of 41.2 % (Fig. 52b). In all configurations, the laser emitted radiation in the fundamental transverse mode TEM₀₀.

7.4.1.4 Tm:YAP laser

In the case of the Tm:YAP laser, the radiation characteristics were again measured for both pump beam polarisations, namely E||c and E||b. The crystal was pumped with pulses of 10 ms duration and a repetition frequency of 10 Hz. When the output mirror with a reflectivity of 97 % was employed, the maximum average output power of 159 mW and a slope efficiency of 17.5 % were achieved for the E||c pump polarisation at a pumping wavelength of 786.4 nm (Fig. 53a). For the E||b polarisation, the output power reached a maximum of 224 mW, with a slope efficiency of 24.3 % for a pumping wavelength of 784.5 nm (Fig. 53b). Even higher slope efficiency of 26 % were achieved when the active medium was pumped at a wavelength of 786.4 nm.

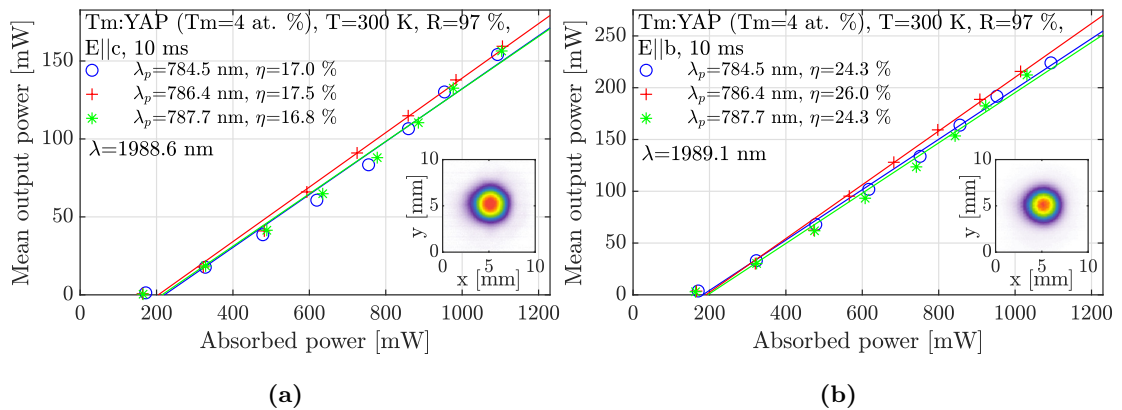


Fig. 53: Characteristics of the Tm:YAP laser with a 97 % reflectivity output mirror for a polarisation E||c (a) and E||b (b).

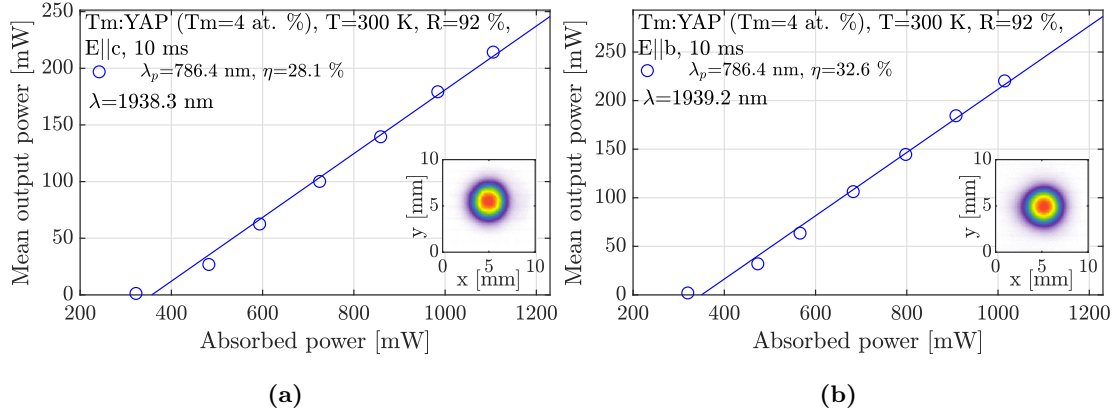


Fig. 54: Characteristics of the Tm:YAP laser with a 92 % reflectivity output mirror for a polarisation E||c (a) and E||b (b).

A pumping wavelength of 786.4 nm was selected for the output mirror with a reflectivity of 92 %. The maximum average output power reached 214 mW with a slope efficiency of 28.1 % for the E||c pump polarisation (Fig. 54a). In the case of the E||b polarisation, the maximum output power increased to 220 mW, with a slope efficiency of 32.6 % (Fig. 54b).

7.4.1.5 Tm:KYW laser

In comparison to the previous crystals, lower powers were achieved for the last crystal Tm:KYW. The characteristics of the laser radiation using an output mirror with a reflectivity of 97 % are shown in Fig. 55. For the E|| N_m pump polarisation, the maximum output power reached only 2.4 mW with a slope efficiency of 0.7 % for pumping radiation at a wavelength of 786.4 nm (Fig. 55a). For the E|| N_p polarisation, the maximum power achieved was 2.6 mW, with a slope efficiency of 0.6 % for pumping at a wavelength of 791.1 nm (Fig. 55b). Longer pumping wavelengths were chosen for this crystal orientation due to the shape of the absorption spectrum, which peaks at a wavelength of 793.8 nm (Fig. 39). The use of a more open output mirror resulted in a slight increase in the power of the laser radiation. For the E|| N_m pump polarisation, the maximum power reached 7.6 mW with a slope efficiency of 2.4 % when pumping at a wavelength of 786.4 nm (Fig. 56a). For the E|| N_p polarisation, the maximum achieved power was 6.1 mW with a slope efficiency of 1.9 % at a pumping wavelength of 791.1 nm (Fig. 56b). When pumping at 789.5 nm, the slope efficiency increased to 2.7 %, but the laser generation threshold also significantly increased. Tm:KYW lasers also generated radiation in the fundamental transverse mode TEM₀₀.

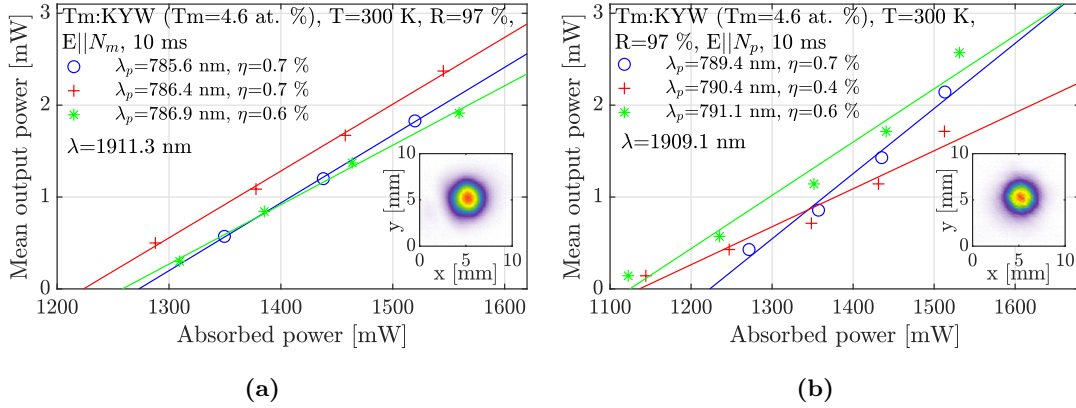


Fig. 55: Characteristics of the Tm:KYW laser with a 97 % reflectivity output mirror for a polarisation $E||N_m$ (a) and $E||N_p$ (b).

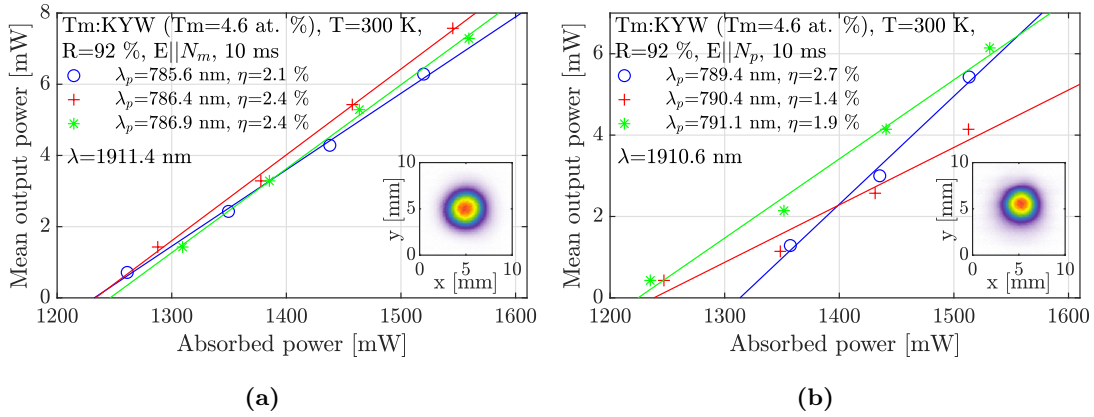


Fig. 56: Characteristics of the Tm:KYW laser with a 92 % reflectivity output mirror for a polarisation $E||N_m$ (a) and $E||N_p$ (b).

7.4.1.6 Laser spectra

A comparison of the laser spectra for semi-hemispherical resonators with output mirrors with reflectivities of 97 % and 92 % is shown in Fig. 57 and 58. From the spectra, it can be seen

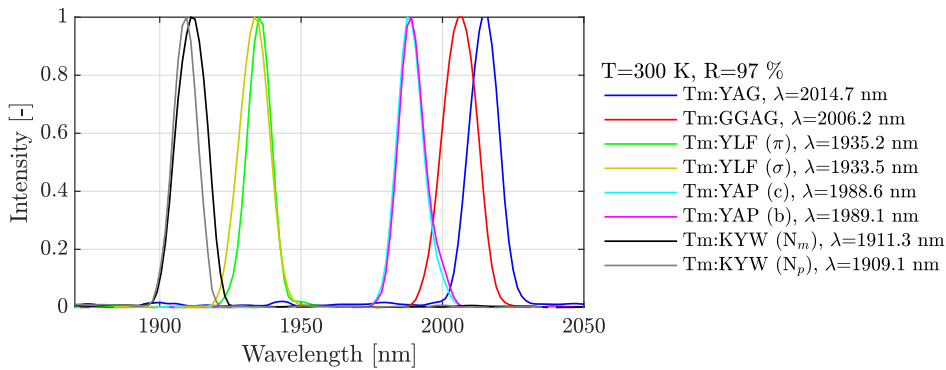


Fig. 57: Spectra of laser radiation of semi-hemispherical Tm lasers for a 97 % reflectivity output coupler.

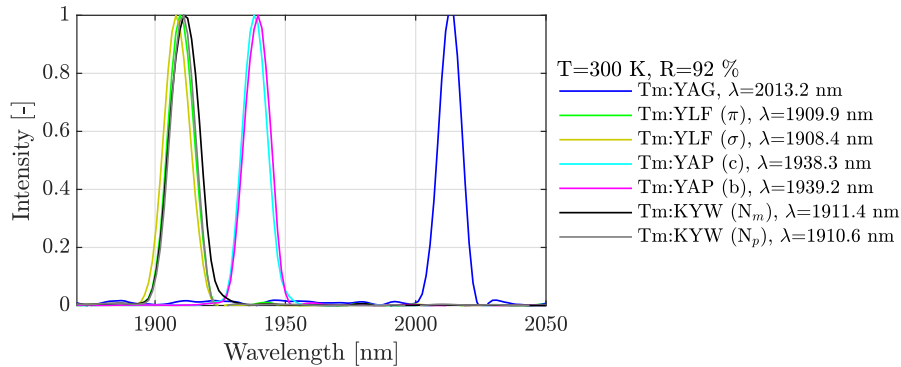


Fig. 58: Spectra of laser radiation of semi-hemispherical Tm lasers for a 92 % reflectivity output coupler.

that the Tm:YAG laser generates radiation at a wavelength of 2014.7 nm with a 97 % reflectivity output mirror, which is closest to the desired wavelength of 2035 nm. It can also be seen that using a more open mirror (92 %) results in a shorter wavelength of generated radiation for lasers Tm:YLF and Tm:YAP, which is probably caused by increased losses in the resonator.

7.4.1.7 Summary of the lasers with semi-hemispherical resonator

Tab. 6 presents a summary of the best results in terms of power for each active medium utilised, considering two output mirrors with reflectivities of 97 % and 92 %, and in the case of birefringent crystals, also for both orientations with respect to the polarisation of the pump radiation. Generally, the Tm:YLF laser exhibited the best performance with regard to both output power and slope efficiency. The maximum mean output power reached 317 mW for the 97 % reflectivity output mirror with pump polarisation $E||\pi$. The Tm:YAG crystal also yielded relatively good results, with a maximum of 265 mW, and the Tm:YAP crystal reached a maximum of 224 mW. In the case of the Tm:GGAG crystal, however, the output power was lower, which may be caused by its inhomogeneity. Although the crystal was scanned, the position where laser emission occurred may have shifted slightly during the mirrors adjustments. However, the lowest output power was observed for the Tm:KYW crystal.

The laser measurement results for threshold power correspond to the estimation based on the product of emission cross-section and fluorescence lifetime (Fig. 47, page 52). For the Tm:YAG crystal at the wavelength around 2 μm , the value of this product was the highest, which means that this laser has the lowest threshold power at this wavelength. These results are in accordance with the results of laser experiments. The Tm:GGAG crystal, which closely followed Tm:YAG, exhibited approximately double the threshold power during laser measurements, but it can be attributed to the crystal quality. Fig. 47 also demonstrates that around 2 μm , the Tm:YLF and Tm:YAP crystals achieved comparable results. However, both crystals exhibit a maximum of

the $\sigma_e \cdot \tau_f$ product at shorter wavelengths, corresponding to laser generation around 1930 nm for Tm:YLF and around 1990 nm for Tm:YAP. At approximately 2 μm , the Tm:KYW laser exhibited the lowest $\sigma_e \cdot \tau_f$ product, as its maximum was below 1.9 μm . This approximately corresponds to laser generation around 1910 nm during laser measurements. Due to its short fluorescence lifetime, it exhibited the highest threshold power.

The Tab. 6 also indicates that for some active media, the use of a more open output mirror resulted in a decrease in output power (e.g., for Tm:YAG), while for others, it increased (e.g., Tm:KYW). By utilising additional mirrors with varying reflectivities, it would be possible to identify the optimal reflectivity for each active medium (and crystal orientation, if applicable).

Based on the results, for further measurements, only the Tm:YAG, Tm:GGAG, Tm:YLF, and Tm:YAP crystals were selected. The Tm:KYW active medium was no longer used due to its low output power.

Tab. 6: The best results for lasers with semi-hemispherical resonator in terms of output power. R - reflectivity of the output coupler M_b , Δt - pump pulse duration, P_{max} - maximum mean output power, P_{th} - threshold absorbed power, η - slope efficiency with respect to absorbed power, λ - wavelength of the laser radiation. All measured values were obtained during a pumping with duty cycle of 10 %.

Active medium	R [%]	Δt [ms]	Pump polarisation	P_{max} [mW]	P_{th} [mW]	η [%]	λ [nm]
Tm:YAG	97	10	-	265	255	19.4	2015
	92	10	-	75	833	9.5	2013
Tm:GGAG	97	5	-	142	508	11.2	2006
Tm:YLF	97	10	E π	317	230	37.5	1935
		10	E σ	272	222	31.9	1934
	92	10	E π	300	318	40.8	1910
		10	E σ	305	321	41.2	1908
Tm:YAP	97	10	E c	159	205	17.5	1989
		10	E b	224	182	24.3	1989
	92	10	E c	214	360	28.1	1938
		10	E b	220	350	32.6	1939
Tm:KYW	97	10	E N_m	2	1224	0.7	1911
		10	E N_p	3	1124	0.6	1909
	92	10	E N_m	8	1235	2.4	1911
		10	E N_p	6	1224	1.9	1911

7.4.2 Lasers with V-shaped resonator

Furthermore, characteristics of the constructed lasers with V-shaped resonator were measured. Starting with this experiment, mirrors with reflectivities of 99.8 % and 97 % was selected as a mirror M_b . All crystals were pumped with radiation at a wavelength of 786.4 nm with a duty cycle of 10 %. Although the output characteristics of these lasers were always measured behind mirror M_b , the powers for maximum pumping were also measured behind the mirror M_c and will be presented. The power of the radiation passing through the mirror M_a was mostly around 1 mW and is neglected here.

7.4.2.1 Tm:YAG laser

The characteristics of the Tm:YAG laser are depicted in Fig. 59a. Utilising mirror M_b with a reflectivity of 99.8 %, a maximum output power of 22 mW and a slope efficiency of 1.9 % were attained. A higher output power of 34 mW was recorded behind the mirror M_c for the maximum pump power. The use of the mirror with a reflectivity of 97 % resulted in a significant increase in output power to 151 mW, accompanied by a corresponding increase in slope efficiency to 13.9 %. However, the power measured behind mirror M_c decreased to 8.1 %.

7.4.2.2 Tm:GGAG laser

The power characteristics of the Tm:GGAG laser are presented in Fig. 59b. Using the mirror M_b with a reflectivity of 99.8 %, a maximum output power of 10 mW and a slope efficiency of 1 % were achieved. However, a power of 18.5 mW was measured behind mirror M_c for maximum pumping. When a more open mirror M_b with a reflectivity of 97 % was used, the power behind mirror M_b increased to 31 mW, with a corresponding increase in slope efficiency to 5.3 %. In contrast, the power measured behind mirror M_c decreased to 3 mW.

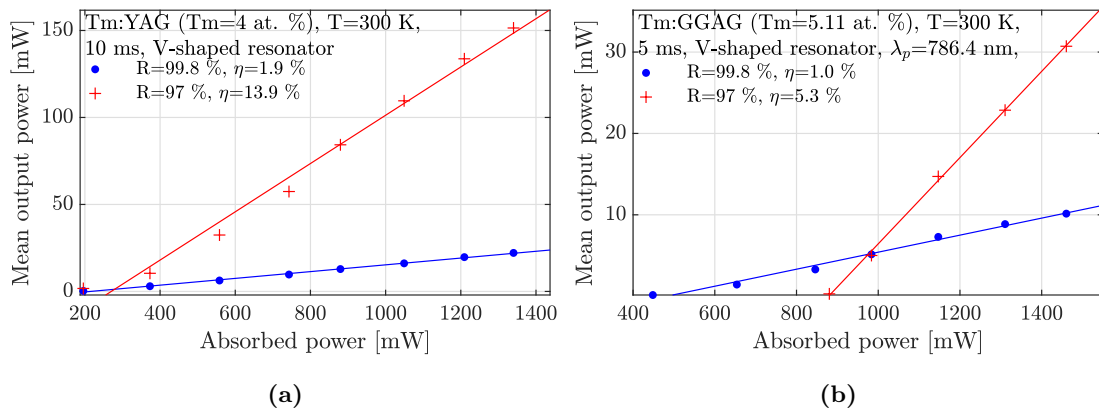


Fig. 59: Characteristics of Tm:YAG (a) and Tm:GGAG (b) lasers with V-shaped resonators.

7.4.2.3 Tm:YLF laser

The dependency of the average output power on the absorbed power for the Tm:YLF laser is depicted in Fig. 60a. When employing the 99.8 % reflectivity mirror M_b , a maximum power of 5 mW behind M_b was achieved for the $E||\pi$ polarisation. The corresponding slope efficiency reached 0.8 %. Behind mirror M_c , a power of 24 mW was measured. For the $E||\sigma$ polarisation, the maximum power behind M_b and its corresponding slope efficiency remained unchanged, while behind M_c , the power increased to 26.7 mW.

With the 97 % reflectivity mirror, M_b , there was an increase in power behind this mirror. For the $E||\pi$ polarisation, the output power reached approximately 11 mW, and the slope efficiency increased to 7.5 %. For the $E||\sigma$ polarisation, the power further increased to 50 mW, with a slope efficiency of 8.8 %. The powers behind mirror M_c decreased to 3.8 mW for $E||\pi$ and 4.5 mW for $E||\sigma$.

7.4.2.4 Tm:YAP laser

The graph of the mean output power in relation to the absorbed power for the Tm:YAP laser is presented in Fig. 60b. When the mirror M_b with a reflectivity of 99.8 % was utilised, the maximum power behind M_b reached only 7 mW for the $E||c$ polarisation. The corresponding slope efficiency was 2 %. The power behind mirror M_c was observed to be 18.9 mW. In the case of the $E||b$ polarisation, there was a slight increase in the maximum power behind M_b to 12 mW, while behind M_c , the power decreased to 8 mW. Slope efficiency decreased to 1.1 %.

When the mirror M_b with a reflectivity of 97 % was employed, there was a notable increase in power behind this mirror. For the $E||c$ polarisation, the mean output power reached 125 mW and the slope efficiency increased to 19 %. In the case of the $E||b$ polarisation, the power increased to 134 mW, accompanied by a slope efficiency of 23 %. The output powers behind mirror M_c were 11.6 mW for $E||c$ and 12.4 mW for $E||b$ polarisation of the pump radiation.

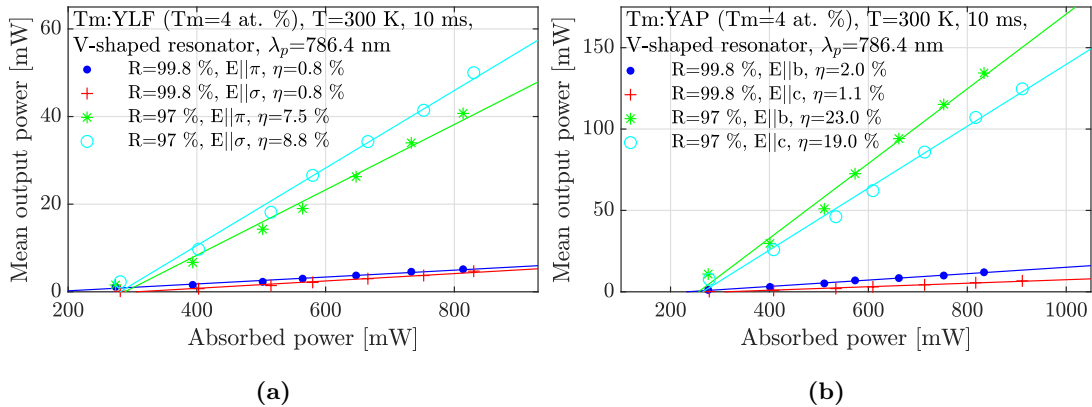


Fig. 60: Characteristics of Tm:YLF (a) and Tm:YAP (b) lasers with V-shaped resonators.

7.4.2.5 Laser spectra

In Fig. 61, a comparison of the spectra of the generated laser radiation for mirror M_b with a reflectivity of 99.8 % is presented. In Fig. 62, the comparison is shown for a mirror with a reflectivity of 97 %. In the former, it is noticeable that the Tm:YLF laser produced radiation at various wavelengths. However, their intensity decreases with increasing wavelengths.

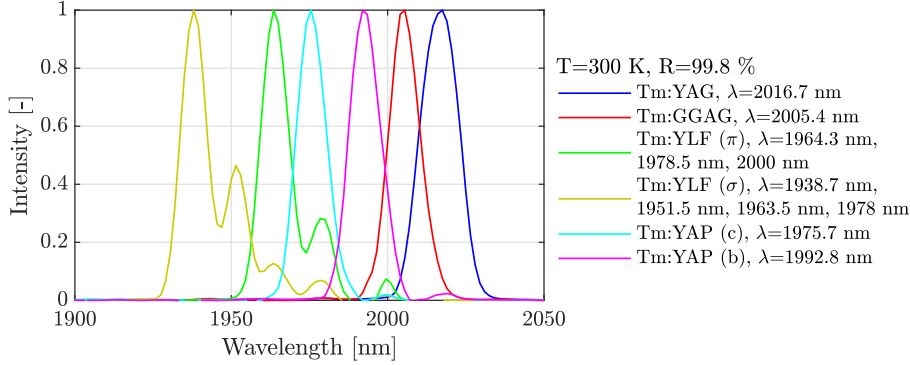


Fig. 61: Comparison of spectra of the lasers with V-shaped resonators for a 99.8 % reflectivity mirror M_b .

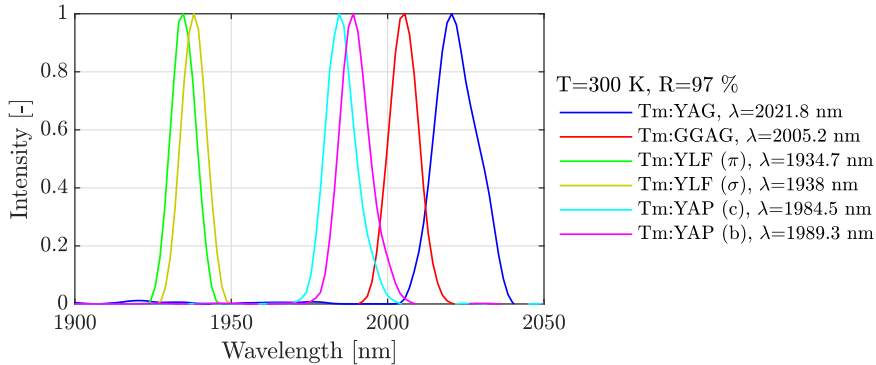


Fig. 62: Comparison of spectra of the lasers with V-shaped resonators for a 97 % reflectivity mirror M_b .

7.4.2.6 Summary of lasers with V-shaped resonator

Tab. 7 presents a summary of the results obtained for lasers with V-shaped resonator. Generally, better results were obtained using the mirror M_b with a reflectivity of 97 %. The highest power of 151 mW was achieved for the Tm:YAG laser. Additionally, the Tm:YAP laser also yielded promising results, particularly for the $E||b$ pump polarisation. In the case of the Tm:YLF laser, the power decreased significantly compared to the laser with semi-hemispherical resonator. Low powers were also achieved with the Tm:GGAG crystal, which is again probably attributed to its non-homogeneity. With regard to the wavelength, the radiation of the Tm:YAG laser approaches

the most to the desired wavelength of 2035 nm, which, when combined with its best achieved output power, provides a favourable opportunity for laser generation with VBG.

Tab. 7: The best results for lasers with V-shaped resonator. R - reflectivity of the mirror M_b , Δt - pump pulse duration, $P_{max}^{M_b}$ - maximum mean output power behind the mirror M_b , $P_{max}^{M_c}$ - maximum mean output power behind the mirror M_c , P_{th} - threshold absorbed power, η - slope efficiency, λ - wavelength of the laser radiation. All measured values were obtained during a pumping with duty cycle of 10 %.

Active medium	R [%]	Δt [ms]	Pump polarisation	$P_{max}^{M_b}$ [mW]	$P_{max}^{M_c}$ [mW]	P_{th} [mW]	η [%]	λ [nm]
Tm:YAG	99.8	10	-	22	34.0	215	1.9	2017
	97	10	-	151	8.1	270	13.9	2022
Tm:GGAG	99.8	5	-	10	18.5	483	1.0	2005
	97	5	-	31	3.0	879	5.3	2005
Tm:YLF	99.8	10	E π	5	24.0	171	0.8	1964
		10	E σ	5	26.7	306	0.8	1939
	97	10	E π	41	3.8	288	7.5	1935
		10	E σ	50	4.5	281	8.8	1938
Tm:YAP	99.8	10	E c	7	18.9	311	2.0	1976
		10	E b	12	8.0	233	1.1	1992
	97	10	E c	125	11.6	265	19.0	1985
		10	E b	134	12.4	257	23.0	1989

7.4.3 Lasers with VBG

This section will present the power characteristics, beam profiles, and radiation spectra of lasers with the VBG. Since a higher output power was measured behind the Bragg grating when using the more closed mirror M_b with a reflectivity of 99.8 %, the presented power characteristics were measured also behind the VBG. However, for the 97 % mirror, the output characteristics were measured behind this mirror, because the output power was higher there. In these experiments, the active media were pumped with radiation at a wavelength of 786.4 nm with a repetition rate of 10 Hz.

7.4.3.1 Tm:YAG laser

On Fig. 63a, the dependence of the output power of the Tm:YAG laser with VBG using mirror M_b with a reflectivity of 99.8 % is depicted. The crystal was pumped with pulses of 10 ms duration and a repetition rate of 10 Hz. A maximum mean output power of 66 mW was achieved behind the VBG, with a slope efficiency of 6.7 %. Behind mirror M_b , the power reached 19 mW, and behind mirror M_c , it was 4.7 mW.

When using mirror M_b with a reflectivity of 97 %, the laser generation ceased shortly after the pumping began. This phenomenon may be attributed to two causes: The first of these is thermal lensing, and the second is a higher reabsorption of laser radiation as a result of a stronger population of the upper sublevels of the ground state with an increasing temperature of the active medium. Therefore, the pump pulse duration was shortened to 5 ms in order to reduce heating of the crystal. Additionally, two resonators of different lengths were tested. In the case of a longer resonator with a total length of 112 mm, a maximum output power of 8.6 mW was achieved with a slope efficiency of 4.9 %. Shortening the resonator increased the power to 12 mW with a slope

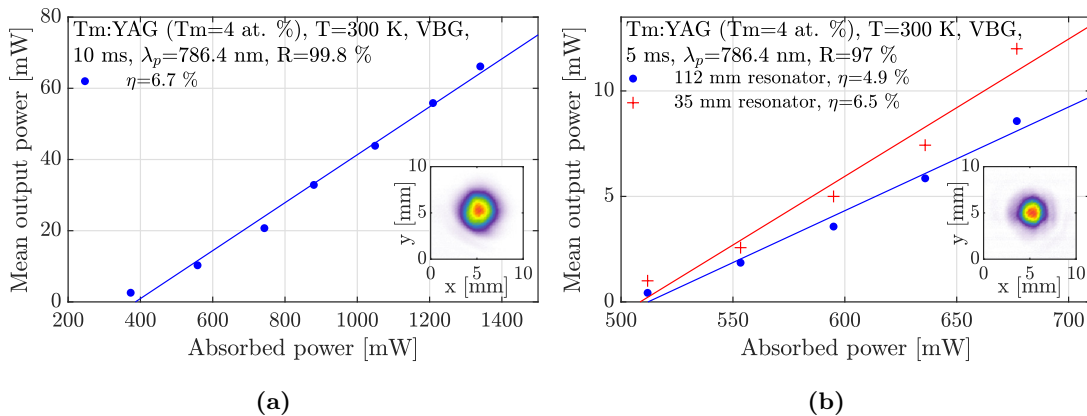


Fig. 63: Characteristics of the Tm:YAG laser with the VBG for a 99.8 % reflectivity (a) and for a 97 % reflectivity (b) of the mirror M_b .

efficiency of 6.5 %. The output power behind the VBG was 4 mW and only 0.5 mW behind M_c . Power characteristics of these lasers are shown in Fig. 63b.

7.4.3.2 Tm:GGAG laser

For the Tm:GGAG active medium with VBG, laser generation was achieved only with mirror M_c with a reflectivity of 99.8 %. The pumping pulse duration was set to 10 ms, and the repetition rate was 10 Hz. The maximum mean output power behind the VBG was 8 mW and the slope efficiency was 1.7 %. The power of the radiation behind M_b was 2 mW, and behind M_c only 0.8 mW.

7.4.3.3 Tm:YLF laser

For the laser with the Tm:YLF active medium and the VBG, the generation of laser radiation was also only achieved when the M_b mirror with a reflectivity of 99.8 % was used. The power characteristics for both crystal orientations are shown in Fig. 64b. For the $E||\pi$ polarisation, a maximum mean output power of 6 mW was achieved behind the VBG, with a slope efficiency of 3.5 %. A power of 1 mW was measured behind the M_b mirror and 1.3 mW behind the M_c mirror. For the second crystal orientation, $E||\sigma$, the output power increased to 30 mW with a slope efficiency of 7.2 %. The power measured behind the M_b mirror was 5 mW and 2.9 mW behind the M_c mirror.

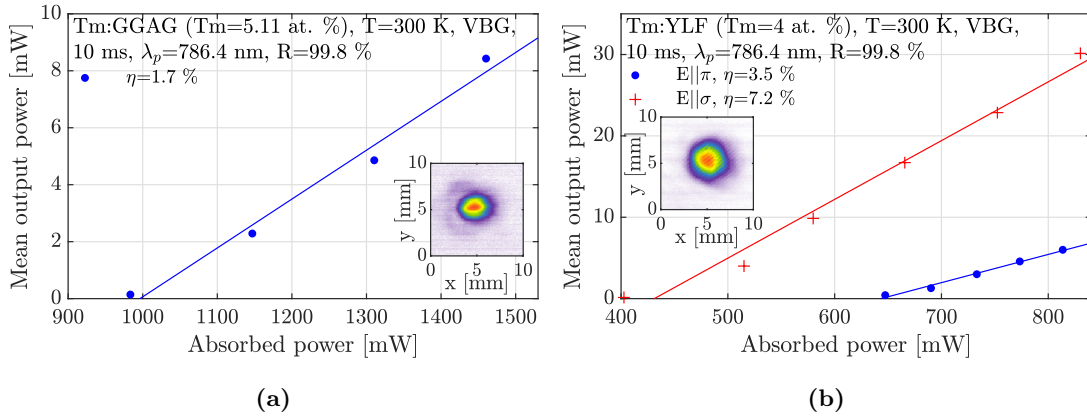


Fig. 64: Characteristics of the Tm:GGAG laser (a) and a Tm:YLF laser (b) with the VBG and the mirror M_b with a reflectivity of 99.8 %.

7.4.3.4 Tm:YAP laser

For the Tm:YAP crystal, laser generation was achieved with both the 99.8 % and the 97 % mirror M_b . Fig. 65a presents the power characteristics for the 99.8 % reflective mirror. A higher power of 37 mW was achieved behind the VBG for the $E||b$ pump polarisation, with a slope

efficiency of 8 %. The radiation power behind mirror M_b was 5 mW, while behind mirror M_c it was only 1.4 mW. For the $E||c$ crystal orientation, the maximum output power decreased to 13 mW with a slope efficiency of 4.8 %. The power behind mirror M_b was 3 mW and behind M_c it was 1.1 mW. In the configuration with a more open mirror of 97 % reflectivity, the power characteristics of this laser are shown in Fig. 65b. In this case, the maximum output power behind M_b was 19 mW, behind the VBG 11 mW, and behind M_c 3.8 mW. The slope efficiency was 10.2 %.

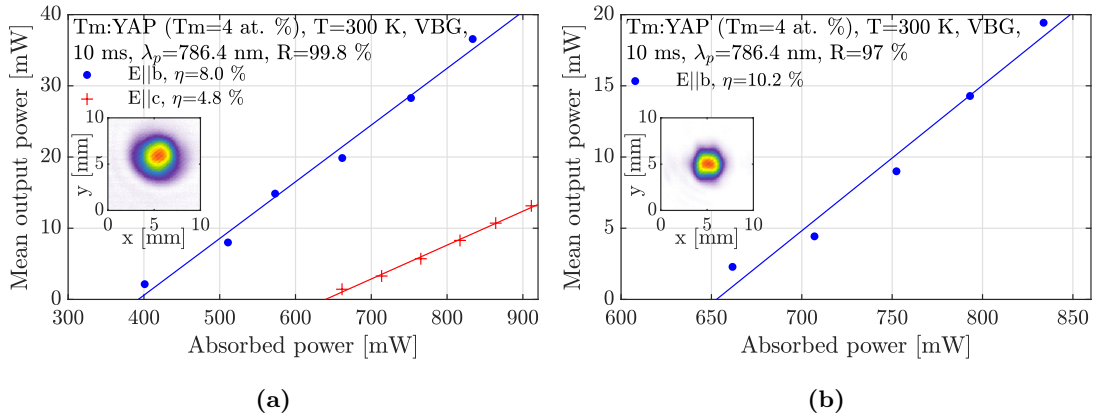


Fig. 65: Characteristics of the Tm:YAP laser with the VBG for a 99.8 % reflectivity (a) and for a 97 % reflectivity (b) of the mirror M_b .

7.4.3.5 Laser spectra

Fig. 66 compares the spectra of laser radiation with the use of the VBG for all crystals. It can be observed that in all cases, generation of the laser radiation around the wavelength of 2035 nm was successful. The observed fluctuations in peak positions within the spectra may be attributed to the spectrometer itself, potentially resulting from small vibrations that may have occurred during its transportation. Volume Bragg gratings manufactured by OptiGrate are designed to stabilize

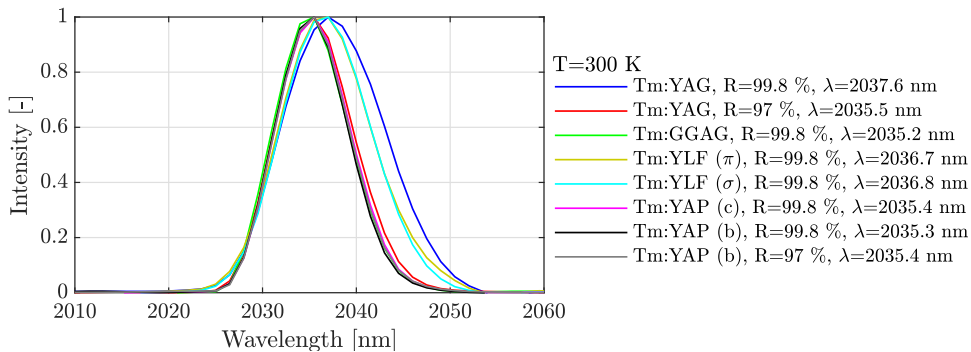


Fig. 66: Spectra of laser radiation with the use of VBG.

the wavelength of laser radiation with a maximum temperature change of 5 pm/K (@ 532 nm).

7.4.3.6 Summary of the lasers with VBG

Tab. 8 presents the results of measuring the characteristics of lasers with the VBG. For all crystals, generation of laser radiation was achieved using the closed mirror with 99.8 % reflectivity. In contrast, achieving laser generation was more challenging with the more open 97 % mirror, and it was only successful for Tm:YAG and Tm:YAP crystals, which had already shown relatively good results in the previous experiments with V-shaped resonators.

Tab. 8: The best results for lasers with the VBG. R - reflectivity of the mirror M_b , Δt - pump pulse duration, $P_{max}^{M_b}$ - maximum mean output power behind the mirror M_b , P_{max}^{VBG} - maximum mean output power behind the VBG, $P_{max}^{M_c}$ - maximum mean output power behind the mirror M_c , P_{th} - threshold absorbed power, η - slope efficiency, λ - wavelength of the laser radiation. All active media were pumped with a repetition rate of 10 Hz.

Active medium	R [%]	Δt [ms]	Pump pol.	$P_{max}^{M_b}$ [mW]	P_{max}^{VBG} [mW]	$P_{max}^{M_c}$ [mW]	P_{th} [mW]	η [%]	λ [nm]
Tm:YAG	99.8	10	-	19	66	4.7	386	6.7	2037.6
	97	5	-	12	3	0.5	509	6.5	2035.5
Tm:GGAG	99.8	10	-	2	8	0.8	996	1.7	2035.2
Tm:YLF	99.8	10	E π	1	6	1.3	643	3.5	2036.7
		10	E σ	5	30	2.9	431	7.2	2036.8
Tm:YAP	99.8	10	E c	3	13	1.1	640	4.8	2035.4
		10	E b	5	37	1.4	393	8.0	2035.3
	97	10	E b	19	11	3.8	653	10.2	2035.4

The highest mean output power reaching 66 mW and the lowest threshold power were achieved for the Tm:YAG laser. This may be attributed to the fact that this laser had already emitted radiation in previous experiments without VBG close to the desired wavelength of 2035 nm. Additionally, the best result was already achieved with this crystal in the experiments with the V-shaped resonators. The Tm:YAP crystal also yielded promising results, particularly for the E||b pump polarisation. This is consistent with expectations, as this crystal generates radiation that is partially polarised along the b-axis. In this orientation, the b-axis is parallel to the folding mirror plane, which has a higher reflectivity for this polarisation. It is noteworthy that the Tm:YLF crystal also demonstrated relatively good performance. This laser, in a semi-hemispherical configuration with a 97 % reflectivity output mirror, emitted radiation around 1935 nm, which indicates tuning of approximately 100 nm. The Tm:GGAG crystal yielded the least promising results, similarly to those observed in the V-shaped resonator case. Based on these results, the Tm:YAG crystal was

selected for further experiments, the outcomes of which are presented in the subsequent sections.

7.4.4 Other experiments of Tm:YAG laser with VBG

7.4.4.1 Cooling

One of the improvements in laser experiments with a Tm:YAG active medium and VBG was the cooling of the crystal. Initially, the active medium was cooled to 15 °C, and a mirror M_b with 99.8 % reflectivity was used. The crystal was pumped with pulses of 10 ms length, at a repetition rate of 10 Hz, and at a wavelength of 786.4 nm. Fig. 67a presents the measured power characteristic behind the VBG. It can be observed that cooling significantly increased the generated power, reaching 102 mW, with a slope efficiency of 11.6 %.

When using a 97 % reflective mirror M_b , cooling helped to eliminate the issues with heating of the crystal, which had previously prevented the laser generation because of the thermal lensing or reabsorption of laser radiation. The effect of different cooling temperatures (10, 15 and 20 °C) was investigated (Fig. 67b). The laser achieved the highest power of 200 mW behind the M_b when the crystal was cooled to 10 °C. The slope efficiency in this case was 22.9 %. A power of 73 mW was measured behind the VBG, and 5 mW behind the M_c mirror.

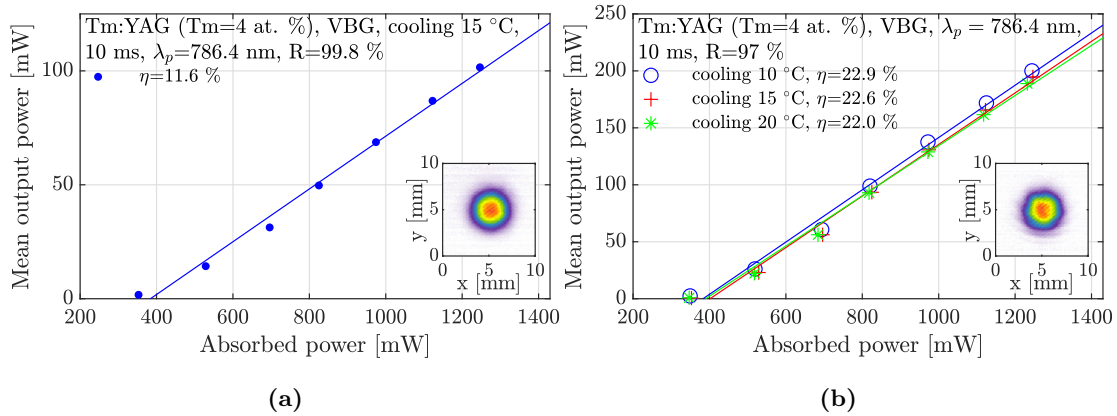


Fig. 67: Power characteristics of the cooled Tm:YAG laser with the VBG for a 99.8 % reflectivity mirror M_b (a) and for a 97 % reflectivity mirror M_b for different cooling temperatures (b).

Further measurements were conducted with a 97 % reflective mirror and crystal cooling to 10 °C for various pumping wavelengths (Fig. 68a). The highest power of 205 mW and the slope efficiency of 23.3 % was achieved for pumping at a wavelength of 786 nm. Fig. 67b shows the spectrum of the output radiation for the laser with a 97 % reflective mirror M_b , using a Tm:YAG crystal cooled to 15 °C and pumped with 10 ms pulses at a wavelength of 786.4 nm. The recorded emission spectrum peaks at a wavelength of 2036.4 nm.

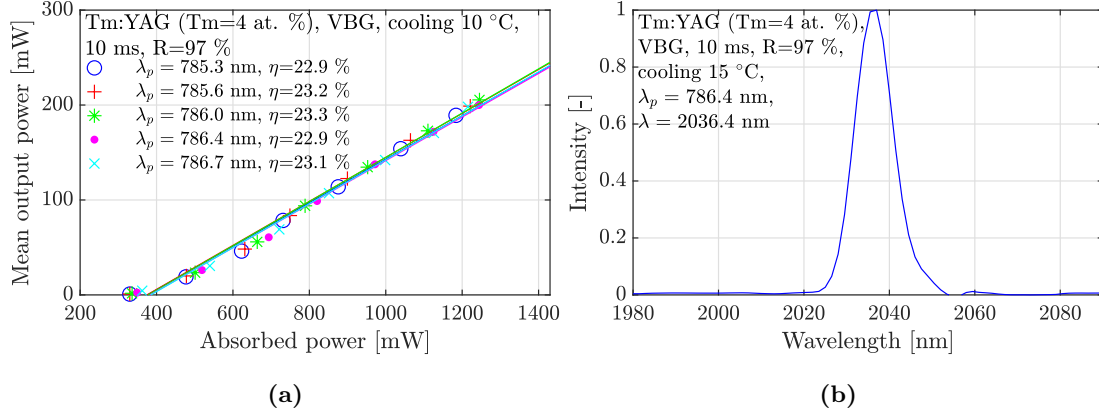


Fig. 68: Power characteristics of the cooled Tm:YAG laser with the VBG for different pump wavelengths (a) and a spectrum of the laser output (b).

7.4.4.2 Generation in the CW regime

Subsequently, the generation of laser radiation was tested for the Tm:YAG crystal with VBG in the CW regime. In this experiment, a mirror M_b with 99.8 % reflectivity was used, and the crystal was cooled to 10 °C. The pumping radiation was set to a wavelength of 784.7 nm. Immediately after the start of the pumping, the power was measured, which is plotted in the graph in Fig. 69a. However, this power subsequently dropped to zero, most likely due to the crystal being strongly heated. The maximum achieved output power was 400 mW. For higher pumping powers, no values could be recorded.

Furthermore, the Tm:YAG active medium was pumped with pulses of 10 ms duration and the gradually increasing duty cycle, and the output power was measured (Fig. 69b). From the graph, it can be observed that the power does not increase linearly; instead, it increases more slowly with

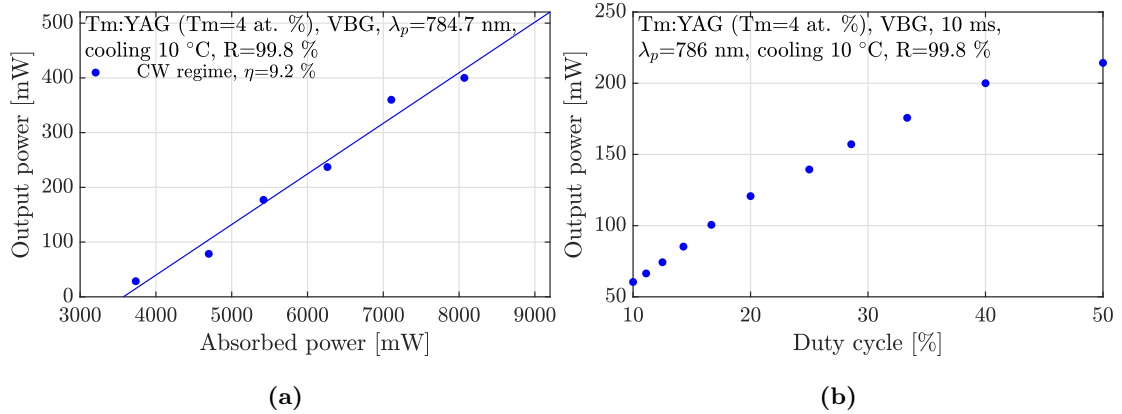


Fig. 69: Power characteristic of the laser Tm:YAG in the CW regime (a) and its output power as a function of a duty cycle (b).

increasing duty cycle. At a 50 % duty cycle, the power began to drop shortly after the pumping was switched on. This again indicates that the crystal is heavily affected by heat. The generation of radiation in CW regime could therefore not be achieved.

7.4.4.3 Short semi-hemispherical resonator

Subsequently, the characteristics of a 17.5 mm short laser Tm:YAG with a semi-hemispherical resonator were measured. The pumping mirror was spherical with 99.8 % reflectivity for a wavelength of 2 μm and 9 % for 786 nm. As an output coupler, the VBG was used (Fig. 22, page 38). The active medium was cooled to 10 $^{\circ}\text{C}$ and pumped with pulses of 10 ms duration and a repetition rate of 10 Hz at a wavelength of 786 nm. Fig. 70a presents the characteristics of this laser. A maximum output power of 156 mW and a slope efficiency of 13 % were achieved. The beam profile corresponding to the fundamental transverse mode TEM_{00} is also shown in the graph. Fig. 70b shows the spectrum of the output radiation, which peaks at a wavelength of 2035.5 nm.

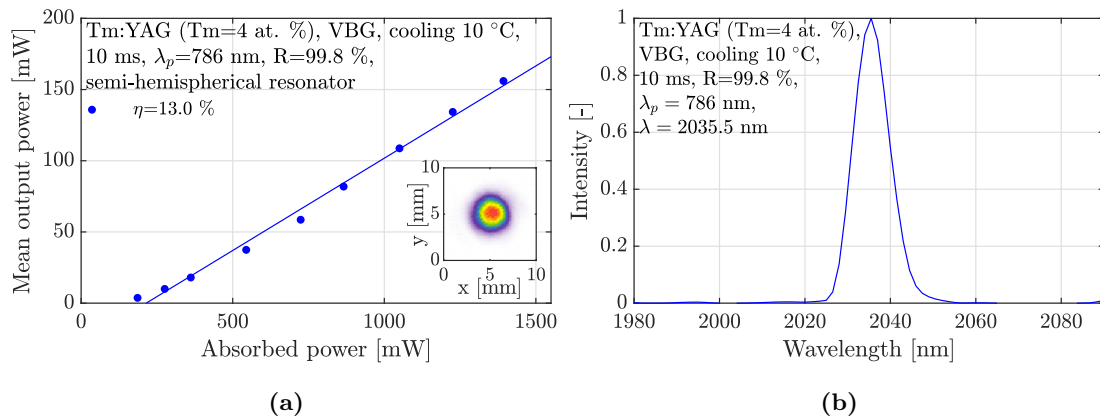


Fig. 70: Power characteristic (a) and spectrum (b) of the laser Tm:YAG with the VBG for a short semi-hemispherical resonator.

7.4.4.4 Q-switching

The last experiment was performed in the Q-switching regime with Tm:YAG active medium cooled to a temperature of 10 $^{\circ}\text{C}$ with the use of the VBG. The crystal was pumped with pulses of 5 ms duration at a repetition rate of 10 Hz. Generation of Q-switched pulses was achieved, although these pulses were not very stable in time. Both the duration of the pulses and the delay of their generation after the triggering pulse exhibited significant fluctuations. In some instances, two pulses were generated consecutively. For various pumping powers, five pulses were consistently recorded, and the range of their durations is plotted in Fig. 71a as a function of the absorbed energy.

Furthermore, a pulse energy was measured again for five different pulses at each pump power. These energies for the given pump power were averaged and plotted in Fig. 71b as a function of absorbed energy. Additionally, the peak power was calculated as the ratio of the average pulse energy to the average pulse duration for the given pump power. The maximum pulse energy reaches a value of 241 μJ , and the maximum peak power is 817 W.

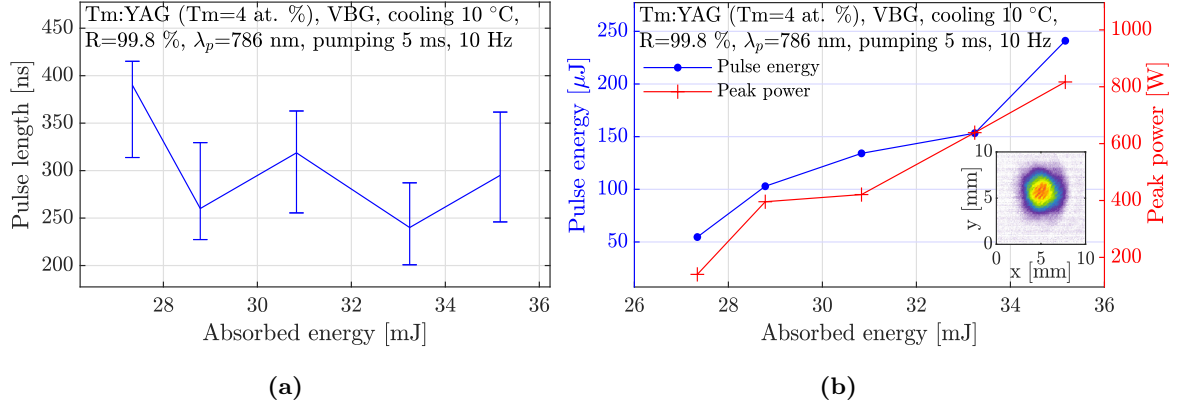


Fig. 71: The dependence of pulse duration (a), pulse energy and peak power (b) on absorbed energy for the Tm:YAG laser with VBG in Q-switching regime.

Fig. 72a displays the shortest generated pulse, which occurred individually, i.e., without being followed by the generation of another pulse. The pulse duration was determined to be 230 ns (FWHM). In Fig. 72b, the spectrum of the generated radiation is depicted, reaching its peak at a wavelength of 2036.5 nm

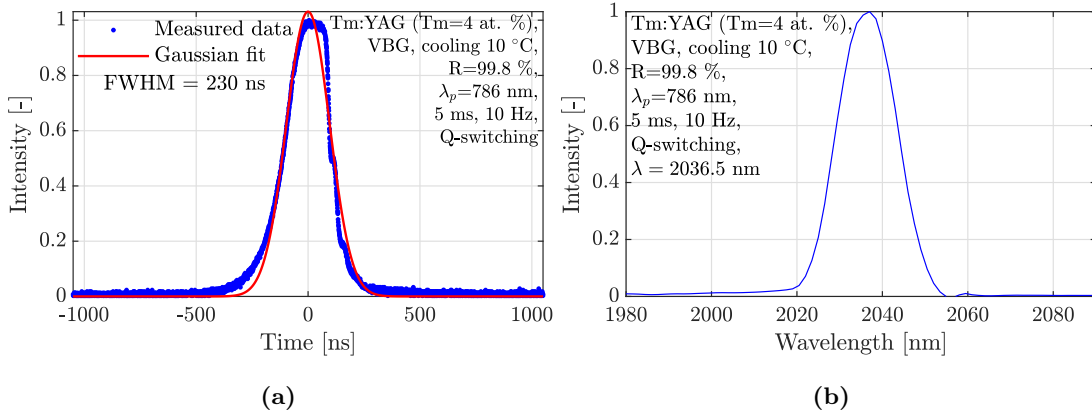


Fig. 72: The temporal profile of the shortest individual pulse (a) and the spectrum of laser radiation (b) for the Tm:YAG laser with VBG in Q-switching regime.

During the measurements, it was observed that some pulses exhibited modulations (a phenomenon known as mode-beating), as shown in the Fig. 73a. By extending the time scale, the modulation frequency of the pulses was determined to be 1.16 GHz (Fig. 73b). This frequency corresponds to the round-trip time in the resonator, allowing the calculation of the optical path length (one half of the round-trip) in the resonator to be 129.3 mm.

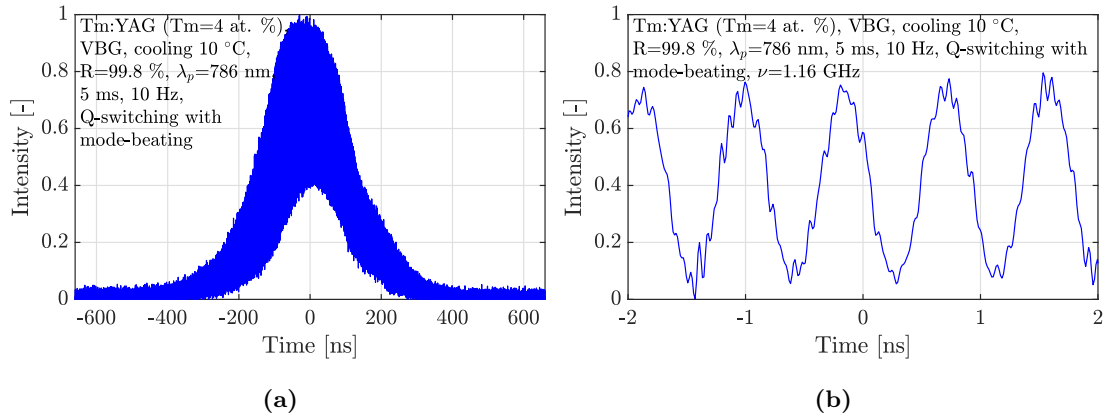


Fig. 73: Q-switched pulse with modulations (a) and a detail of the modulations (b).

8 Conclusion

The objective of this thesis was initially to gain familiarity with the methods of generating laser radiation around the wavelength of 2035 nm and its possible applications, with a particular focus on solid-state lasers utilising thulium-doped active media, as well as on the potential utilisation of volume Bragg gratings. Another objective was to perform basic spectroscopic characterization of available thulium-doped crystals, followed by the design and construction of a diode-pumped laser generating radiation around the wavelength of 2035 nm, and finally, to characterize the generated output radiation and compare different design variants.

The research part of the thesis is presented in chapters 2-5. Chapter 2 focuses on the possibilities of generating laser radiation in the 2 μm region, including a description of thulium-doped active media and matrices such as Tm:YAG, Tm:GGAG, Tm:YLF, Tm:YAP, and Tm:KYW. Chapter 3 introduces various tuning elements suitable for wavelength selection. Chapter 4 further examines potential applications of laser radiation around the wavelength of 2035 nm. Chapter 5 then describes two experiments in which other authors have successfully generated radiation in this spectral region.

The experimental section of the thesis is presented in chapters 6 and 7. Chapter 6 introduces the experimental setup, beginning with a description of the active media. It then describes the constructed laser resonators and all optical elements employed including the VBG. Subsequently, this chapter describes the pumping laser diode and provides a description of spectroscopic and laser measurements, including the measuring instruments.

In chapter 7, the results of the experiments are presented, starting with the characterisation of the pump diode radiation and the measured reflectivities of the optical elements in the resonators. Furthermore, results of the spectroscopic measurement are presented, which comprise absorption and fluorescence spectra of the utilised active media, their measured fluorescence lifetimes, calculated emission cross-sections and estimation of the laser threshold based on the spectroscopic characteristics. Finally, the chapter presents the results of laser experiments, first for semi-hemispherical resonators, then for V-shaped resonators, and subsequently for lasers with VBG. A brief summary is provided for each type of resonator. Furthermore, this chapter includes additional experiments conducted with the Tm:YAG active medium and the VBG. These include cooling of the active medium, generation in the CW regime, construction of a short semi-hemispherical resonator, and Q-switching.

Measurements of the absorption spectra revealed the peak positions, allowing for the determination of suitable pump wavelengths. Unfortunately, the temperature constraints of the pump diode limited the ability to pump some active media within their absorption peaks. The measurements of the fluorescence spectra revealed that the highest fluorescence in the 2035 nm region

is exhibited by Tm:YAG and Tm:GGAG crystals, which is favourable for the generation of laser radiation in this spectral region. Conversely, Tm:YLF, Tm:YAP, and Tm:KYW crystals exhibited lower fluorescence at this wavelength. From the product of the calculated emission cross-section and the measured fluorescence lifetime, it was estimated that the laser with the lowest threshold for generation of radiation around the wavelength of 2035 nm would be Tm:YAG.

Initially, laser measurements were conducted to determine the power that could be generated using a given active medium in a semi-hemispherical configuration, as well as the wavelength of the generated radiation. Based on these results, it was decided that further experiments would be conducted only with Tm:YAG, Tm:GGAG, Tm:YLF, and Tm:YAP crystals. The results for V-shaped resonators revealed how the power and wavelength of the generated radiation changed after inserting the folding mirror. The highest powers were achieved by Tm:YAG and Tm:YAP lasers, while the power for Tm:YLF and Tm:GGAG lasers decreased significantly. Furthermore, lasers with VBG were constructed for all crystals Tm:YAG, Tm:GGAG, Tm:YLF, and Tm:YAP, and radiation around the wavelength of 2035 nm was successfully generated for each active medium. The results of this measurement revealed that the Tm:YAG laser exhibited the highest mean output power of 66 mW and the lowest threshold power. Consequently, this laser was selected for further improvement and other experiments with the VBG.

The improvement of the experiment with the Tm:YAG crystal involved its cooling, which resulted in an average power of generated radiation reaching up to 205 mW and a slope efficiency of 23.3 %. Furthermore, attempts were made to generate laser radiation in CW regime, but despite cooling, the crystal was subjected to significant thermal load, and the power consistently dropped to zero shortly after the start of pumping. Additionally, a short semi-hemispherical resonator with a pumping mirror and output through VBG was constructed. In this experiment, a maximum average power of 156 mW and a slope efficiency of 13 % were achieved. Finally, an experiment was conducted in the Q-switching regime. Pulses with a maximum energy of 241 μ J and a maximum peak power of 817 W were generated and the wavelength of the radiation remained at 2036.5 nm. However, the pulses exhibited temporal instability, with significant fluctuations in duration. The shortest recorded individual pulse had a duration of 230 ns.

The results of the conducted measurements indicate that the combination of thulium-doped crystals and a volume Bragg grating is suitable for generating laser radiation in the atmospheric window around the wavelength of 2035 nm. Regarding the above mentioned, it can be stated that the objectives of this master's thesis have been achieved.

List of Tables

1	Parameters of the thulium-doped active media. n - refractive index, dn/dT - thermo-optic coefficient, κ - thermal conductivity, E_{ph} - phonon energy, λ_p - typical pump wavelength, λ_l - typical laser emission wavelength, Δ_λ - tuning range, τ_f - fluorescence lifetime of the transition ${}^3F_4 \rightarrow {}^3H_6$, τ_r - radiative lifetime, σ_a - maximum absorption cross section, σ_e - maximum emission cross section. These values were reported for room temperature.	19
2	Parameters of the active media used in the experiments.	33
3	Table of all mirrors used for the construction of resonators; r - radius of curvature, R - reflectivity, T - transmission.	35
4	Table of constants for calculation of a voltage applied on the Pockels cell.	40
5	Parameters of the laser diode LIMO provided by the manufacturer.	40
6	The best results for lasers with semi-hemispherical resonator in terms of output power. R - reflectivity of the output coupler M_b , Δt - pump pulse duration, P_{max} - maximum mean output power, P_{th} - threshold absorbed power, η - slope efficiency with respect to absorbed power, λ - wavelength of the laser radiation. All measured values were obtained during a pumping with duty cycle of 10 %.	60
7	The best results for lasers with V-shaped resonator. R - reflectivity of the mirror M_b , Δt - pump pulse duration, $P_{max}^{M_b}$ - maximum mean output power behind the mirror M_b , $P_{max}^{M_c}$ - maximum mean output power behind the mirror M_c , P_{th} - threshold absorbed power, η - slope efficiency, λ - wavelength of the laser radiation. All measured values were obtained during a pumping with duty cycle of 10 %.	64
8	The best results for lasers with the VBG. R - reflectivity of the mirror M_b , Δt - pump pulse duration, $P_{max}^{M_b}$ - maximum mean output power behind the mirror M_b , P_{max}^{VBG} - maximum mean output power behind the VBG, $P_{max}^{M_c}$ - maximum mean output power behind the mirror M_c , P_{th} - threshold absorbed power, η - slope efficiency, λ - wavelength of the laser radiation. All active media were pumped with a repetition rate of 10 Hz.	68

List of Figures

1	Transmission of the atmosphere in the SWIR range (a) and detail around 2 μm (b). The data were measured by Caltech Optical Observatories.	10
2	Simplified diagram of energy levels of a Tm^{3+} ion. CR - cross-relaxation, UC - cooperative upconversion [2, 8, 9].	13
3	Orientation of crystallographic axes a, b and c and optical axes N_m , N_p and N_g for the KYW crystal. Modified from [35].	18
4	Passage of radiation through a prism.	21
5	Setup of a laser with a prism for wavelength tuning [47, p. 285].	21
6	Setup of a laser with a diffraction grating in Littrow configuration for wavelength tuning [47, p. 285]	23
7	Reflecting (a) and transmitting (b) volume Bragg grating.	24
8	Setup of a laser with a birefringent tuner and polarizers for wavelength tuning [47, p. 286].	25
9	Possible generated longitudinal laser modes before and after inserting an etalon [48, p. 13].	26
10	Setup of a laser with an etalon for wavelength tuning.	27
11	Block diagram of LIDAR using the time-of-flight method [61].	29
12	Experimental setup of a Ho:YAG laser emitting at 2044 nm [64].	31
13	Experimental setup of a MOPA fibre laser [65].	32
14	Experimental setup of a laser with a semi-hemispherical resonator.	34
15	Photo of the experimental arrangement of a laser Tm:GGAG with a semi-hemispherical resonator.	35
16	Experimental setup of the second type of resonator.	35
17	Photo of the experimental arrangement of a laser Tm:YLF with a V-shaped resonator.	36
18	Volume Bragg grating.	36
19	Experimental setup of the third type of resonator.	37
20	Photo of the experimental arrangement of the laser Tm:YAG with VBG.	37
21	Experimental setup of the short semi-hemispherical resonator with a VBG.	38
22	Photo of the experimental setup of the short semi-hemispherical resonator with VBG.	38
23	Experimental setup of the resonator constructed for the Q-switching.	39
24	Photo of the experimental arrangement of a Q-switched laser Tm:YAG with a VBG.	39
25	Experimental setup for a fluorescence lifetime measurement.	41
26	Photo of the experimental arrangement of a laser Tm:GGAG with stepper motors for scanning.	43

27	Mean output power (a) and wavelength (b) as a function of diode current for a 5 ms current pulse and for different diode temperatures.	44
28	Mean output power (a) and wavelength (b) as a function of diode current for a 10 ms current pulse and for different diode temperatures.	44
29	Reflectivity of the mirror M_1	45
30	Reflectivity of the mirrors M_3 and M_4	45
31	Reflectivity of the mirror M_5	45
32	Reflectivity of mirror M_2 with respect to the angle of incidence for wavelength 2036 nm for polarisations s and p.	46
33	Transmission spectrum of the VBG.	46
34	Transmission spectrum of anti-reflective coated LiNbO_3 crystal used for Pockels Cell.	46
35	Absorption spectrum of Tm:YAG.	47
36	Absorption spectrum of Tm:GGAG.	47
37	Absorption spectrum of Tm:YLF.	48
38	Absorption spectrum of Tm:YAP.	48
39	Absorption spectrum of Tm:KYW.	48
40	Fluorescence spectra of Tm:YAG and Tm:GGAG.	49
41	Fluorescence spectra of Tm:YLF and Tm:YAP.	49
42	Fluorescence spectra of Tm:KYW.	49
43	Emission cross-sections of the thulium-doped active media.	50
44	Fluorescence decay of Tm:YAG and Tm:GGAG.	51
45	Fluorescence decay of Tm:YLF and Tm:YAP.	51
46	Fluorescence decay of Tm:KYW.	51
47	Calculated product $\sigma_e \cdot \tau_f$ for the thulium-doped active media.	52
48	Characteristics of the Tm:YAG laser with a 97 % reflectivity (a) and a 92 % reflectivity (b) output mirror.	53
49	Scan of the entire Tm:GGAG crystal (a) and a detailed view of a position of a maximum output power (b). P_{out} - mean output power of the laser radiation normalised to the maximum value.	54
50	Characteristics of the Tm:GGAG laser with an output coupler with a reflectivity of 97 %.	55
51	Characteristics of the Tm:YLF laser with a 97 % reflectivity output mirror for a polarisation $E \pi$ (a) and $E \sigma$ (b).	55
52	Characteristics of the Tm:YLF laser with a 92 % reflectivity output mirror for a polarisation $E \pi$ (a) and $E \sigma$ (b).	56

53	Characteristics of the Tm:YAP laser with a 97 % reflectivity output mirror for a polarisation $E c$ (a) and $E b$ (b).	56
54	Characteristics of the Tm:YAP laser with a 92 % reflectivity output mirror for a polarisation $E c$ (a) and $E b$ (b).	57
55	Characteristics of the Tm:KYW laser with a 97 % reflectivity output mirror for a polarisation $E N_m$ (a) and $E N_p$ (b).	58
56	Characteristics of the Tm:KYW laser with a 92 % reflectivity output mirror for a polarisation $E N_m$ (a) and $E N_p$ (b).	58
57	Spectra of laser radiation of semi-hemispherical Tm lasers for a 97 % reflectivity output coupler.	58
58	Spectra of laser radiation of semi-hemispherical Tm lasers for a 92 % reflectivity output coupler.	59
59	Characteristics of Tm:YAG (a) and Tm:GGAG (b) lasers with V-shaped resonators.	61
60	Characteristics of Tm:YLF (a) and Tm:YAP (b) lasers with V-shaped resonators.	62
61	Comparison of spectra of the lasers with V-shaped resonators for a 99.8 % reflectivity mirror M_b .	63
62	Comparison of spectra of the lasers with V-shaped resonators for a 97 % reflectivity mirror M_b .	63
63	Characteristics of the Tm:YAG laser with the VBG for a 99.8 % reflectivity (a) and for a 97 % reflectivity (b) of the mirror M_b .	65
64	Characteristics of the Tm:GGAG laser (a) and a Tm:YLF laser (b) with the VBG and the mirror M_b with a reflectivity of 99.8 %.	66
65	Characteristics of the Tm:YAP laser with the VBG for a 99.8 % reflectivity (a) and for a 97 % reflectivity (b) of the mirror M_b .	67
66	Spectra of laser radiation with the use of VBG.	67
67	Power characteristics of the cooled Tm:YAG laser with the VBG for a 99.8 % reflectivity mirror M_b (a) and for a 97 % reflectivity mirror M_b for different cooling temperatures (b).	70
68	Power characteristics of the cooled Tm:YAG laser with the VBG for different pump wavelengths (a) and a spectrum of the laser output (b).	71
69	Power characteristic of the laser Tm:YAG in the CW regime (a) and its output power as a function of a duty cycle (b).	71
70	Power characteristic (a) and spectrum (b) of the laser Tm:YAG with the VBG for a short semi-hemispherical resonator.	72
71	The dependence of pulse duration (a), pulse energy and peak power (b) on absorbed energy for the Tm:YAG laser with VBG in Q-switching regime.	73

72	The temporal profile of the shortest individual pulse (a) and the spectrum of laser radiation (b) for the Tm:YAG laser with VBG in Q-switching regime.	73
73	Q-switched pulse with modulations (a) and a detail of the modulations (b).	74

References

- [1] PASCHOTTA, R.: *Encyclopedia of Laser Physics and Technology*, Wiley-VCH, 2008, ISBN 9783527408283.
- [2] SCHOLLE, K., LAMRINI, S., KOOPMANN, P., FUHRBERG, P.: 2 μm laser sources and their possible applications, *Frontiers in Guided Wave Optics and Optoelectronics*, 2 2010, doi: <https://doi.org/10.5772/39538>.
- [3] SOROKINA, I. T., VODOPYANOV, K. L., eds.: *Solid-state mid-infrared laser sources*, vol. 89 of *Topics in Applied Physics*, Springer-Verlag, Berlin, 2003, ISBN 3-540-00621-4.
- [4] ŠULC, J., JELÍNKOVÁ, H.: Solid-state lasers for medical applications, *Lasers for Medical Applications: Diagnostics, Therapy and Surgery*, 1 2013, pp. 127–176, doi:<https://doi.org/10.1533/9780857097545.2.127>.
- [5] JABCZYNSKI, J. K., GORAJEK, L., ZENDZIAN, W., KWIATKOWSKI, J., JELÍNKOVÁ, H., ŠULC, J., NĚMEC, M.: High repetition rate, high peak power, diode pumped Tm:YLF laser, *Laser Physics Letters*, 10 2008, **vol. 6**, p. 109, doi:<https://doi.org/10.1002/lapl.200810107>.
- [6] LI, Y., ZHANG, J., JIA, Z., LIU, Y., NIE, H., ZHANG, B., TAO, X.: Growth, thermal and spectroscopic properties, and continuous-wave laser performance of Tm,Ho:GGAG crystal for 2 μm lasers, *Journal of Crystal Growth*, 2023, **vol. 601**, p. 126948, ISSN 0022-0248, doi:<https://doi.org/10.1016/j.jcrysgro.2022.126948>.
- [7] KOECHNER, W.: *Solid-State Laser Engineering*, vol. 1, Springer Berlin Heidelberg, 1988, ISBN 978-3-662-15145-7, doi:<https://doi.org/10.1007/978-3-662-15143-3>.
- [8] ANDROZ, G., BERNIER, M., FAUCHER, D., VALLÉE, R.: 2.3 W single transverse mode thulium-doped ZBLAN fiber laser at 1480 nm, *Optics express*, 3 2008, **vol. 16**, pp. 16019–16031, doi:<https://doi.org/10.1364/OE.16.016019>.
- [9] BURYI, O., SUGAK, D., UBIZSKII, S., IZHININ, I., VAKIV, M., SOLSKII, I.: The comparative analysis and optimization of the free-running Tm³⁺:YAP and Tm³⁺:YAG microlasers, *Applied Physics B*, 08 2007, **vol. 88**, pp. 433–442, doi:<https://doi.org/10.1007/s00340-007-2718-3>.
- [10] EICHHORN, M.: Quasi-three-level solid-state lasers in the near and mid infrared based on trivalent rare earth ions, *Appl Phys B*, 2008, **vol. 93**, pp. 269–316, doi:<https://doi.org/10.1007/s00340-008-3214-0>.
- [11] KRATOCHVÍL, J., BOHÁČEK, P., ŠULC, J., NĚMEC, M., JELÍNKOVÁ, H., FIBRICH, M., TRUNDA, B., HAVLÁK, L., JUREK, K., NIKL, M., PRAJZLER, V.: Tm:GGAG disordered

-
- garnet crystal for 2 μm diode-pumped solid-state laser, *Laser Physics Letters*, 9 2021, **vol. 18**, p. 115802, doi:<https://doi.org/10.1088/1612-202X/ac2519>.
- [12] YUAN, D., JIA, Z., LI, Y., WU, B., TAO, X.: Micro-pulling-down furnace modification and single crystal fibers growth, in W. A. Clarkson, R. K. Shori, eds., *Solid State Lasers XXV: Technology and Devices*, vol. 9726, International Society for Optics and Photonics, SPIE, 2016 p. 97260E, doi:<https://doi.org/10.1117/12.2211220>.
- [13] WU, C. T., JU, Y. L., WANG, Z. G., WANG, Q., SONG, C. W., WANG, Y. Z.: Diode-pumped single frequency Tm:YAG laser at room temperature, *Laser Physics Letters*, jul 2008, **vol. 5(11)**, p. 793, doi:<https://dx.doi.org/10.1002/lapl.200810069>.
- [14] ELDER, I., PAYNE, M.: YAP versus YAG as a diode-pumped host for thulium, *Optics Communications*, 1998, **vol. 148(4)**, pp. 265–269, ISSN 0030-4018, doi:[https://doi.org/10.1016/S0030-4018\(97\)00714-1](https://doi.org/10.1016/S0030-4018(97)00714-1).
- [15] ŠVEJKAR, R., ŠULC, J., BOHÁČEK, P., NĚMEC, M., JELÍNKOVÁ, H., TRUNDA, B., HAVLÁK, L., NIKL, M., JUREK, K.: Influence of Er^{3+} concentration in Er:GGAG crystal on spectroscopic and laser properties, *Journal of Alloys and Compounds*, 2023, **vol. 941**, p. 168964, ISSN 0925-8388, doi:<https://doi.org/10.1016/j.jallcom.2023.168964>.
- [16] BEACH, R. J., SUTTON, S. B., HONEA, E. C., SKIDMORE, J. A., EMANUEL, M. A.: High-power 2- μm diode-pumped Tm:YAG laser, in R. Scheps, ed., *Solid State Lasers V*, vol. 2698, International Society for Optics and Photonics, SPIE, 1996 pp. 168 – 175, doi:<https://doi.org/10.1117/12.236152>.
- [17] QUEHL, G., GRÜNERT, J., ELMAN, V., HEMMERICH, A.: A tunable dual frequency Tm:YAG laser, *Optics Communications*, 2001, **vol. 190(1)**, pp. 303–307, ISSN 0030-4018, doi:[https://doi.org/10.1016/S0030-4018\(01\)01077-X](https://doi.org/10.1016/S0030-4018(01)01077-X).
- [18] SONG, P., ZHAO, Z., XU, X., JANG, B., DENG, P., XU, J.: Growth and properties of Tm:YAG crystals, *Journal of Crystal Growth*, 2004, **vol. 270**, pp. 433–437, doi:<https://doi.org/10.1016/j.jcrysgro.2004.06.042>.
- [19] YUMOTO, M., SAITO, N., URATA, Y., WADA, S.: 128 mJ/Pulse, Laser-Diode-Pumped, Q-Switched Tm:YAG Laser, *IEEE Journal of Selected Topics in Quantum Electronics*, 2015, **vol. 21(1)**, pp. 364–368, doi:<https://doi.org/10.1109/JSTQE.2014.2338872>.
- [20] KRATOCHVÍL, J., BOHÁČEK, P., SULC, J., NĚMEC, M., FIBRICH, M., JELÍNKOVÁ, H., TRUNDA, B., HAVLÁK, L., JUREK, K., NIKL, M.: 1.7 μm diode-pumped Tm:GGAG and Tm, Ho:GGAG 2.0-2.1 μm laser, in W. A. Clarkson, R. K. Shori, eds., *Solid State Lasers*
-

-
- XXIX: Technology and Devices*, vol. 11259, International Society for Optics and Photonics, SPIE, 2020 p. 1125905, doi:<https://doi.org/10.1117/12.2545795>.
- [21] ŠULC, J., BOHÁČEK, P., NĚMEC, M., FIBRICH, M., JELINKOVÁ, H., TRUNDA, B., HAVLÁK, L., JUREK, K., NIKL, M.: Tm:GGAG crystal for 2 μ m tunable diode-pumped laser, in J. I. Mackenzie, H. Jelínková, T. Taira, M. A. Ahmed, eds., *Laser Sources and Applications III*, vol. 9893, International Society for Optics and Photonics, SPIE, 2016 p. 98930H, doi:<https://doi.org/10.1117/12.2227641>.
- [22] LUONG, M. V., EMPIZO, M. J. F., GABAYNO, J. L. F., MINAMI, Y., YAMANOI, K., SHIMIZU, T., SARUKURA, N., PHAM, M. H., NGUYEN, H. D., STEENBERGEN, K. G., SCHWERDTFEGER, P., CADATAL-RADUBAN, M.: Direct band gap tunability of the LiYF₄ crystal through high-pressure applications, *Computational Materials Science*, ISSN 0927-0256, doi:<https://doi.org/10.1016/j.commatsci.2018.07.020>.
- [23] XIONG, J., PENG, H., HU, P., HANG, Y., ZHANG, L.: Optical characterization of Tm³⁺ in LiYF₄ and LiLuF₄ crystals, *Journal of Physics D: Applied Physics*, apr 2010, vol. **43(18)**, p. 185402, doi:<https://doi.org/10.1088/0022-3727/43/18/185402>.
- [24] AGGARWAL, R., RIPIN, D., OCHOA, J., FAN, T.: Measurement of thermo-optic properties of Y₃Al₅O₁₂, Lu₃Al₅O₁₂, YAlO₃, LiYF₄, LiLuF₄, BaY₂F₈, KGd(WO₄)₂, and KY(WO₄)₂ laser crystals in the 80-300 K temperature range, *Journal of Applied Physics*, 12 2005, vol. **98**, pp. 103514 – 103514, doi:<https://doi.org/10.1063/1.2128696>.
- [25] SCHELLHORN, M.: High-power diode-pumped Tm:YLF laser, *Applied Physics B: Lasers and Optics*, 4 2008, vol. **91**, pp. 71–74, ISSN 09462171, doi:<https://doi.org/10.1007/S00340-008-2943-4/METRICS>.
- [26] CORNACCHIA, F., TONCELLI, A., TONELLI, M.: 2- μ m lasers with fluoride crystals: Research and development, *Progress in Quantum Electronics*, 2009, vol. **33(2)**, pp. 61–109, ISSN 0079-6727, doi:<https://doi.org/10.1016/j.pquantelec.2009.04.001>.
- [27] DING, Y., ZHANG, D., WANG, W., YAO, B., DUAN, X., JU, Y., WANG, Y.: High power Tm:YLF laser operating at 1.94 μ m, *Optik*, 2015, vol. **126(7)**, pp. 855–857, ISSN 0030-4026, doi:<https://doi.org/10.1016/j.ijleo.2015.02.032>.
- [28] ZHANG, B., LI, L., HE, C., TIAN, F., CUI, J., ZHANG, J., SUN, W.: Compact self-Q-switched Tm:YLF laser at 1.91 μ m, *Optics & Laser Technology*, 03 2018, vol. **100**, doi:<https://doi.org/10.1016/j.optlastec.2017.10.001>.
-

-
- [29] DEMIRBAS, U., THESINGA, J., BEYATLI, E., KELLERT, M., PERGAMENT, M., KÄRTNER, F. X.: Continuous-wave Tm:YLF laser with ultrabroad tuning (1772-2145 nm), *Opt. Express*, Nov 2022, **vol. 30(23)**, pp. 41219–41239, doi:<https://doi.org/10.1364/OE.471288>.
- [30] WALSH, B., BARNES, N., DI BARTOLO, B.: Branching Ratios, Cross Sections, and Radiative Lifetimes of Rare Earth Ions in Solids: Application to Tm³⁺ and Ho³⁺ Ions in LiYF₄, *Journal of Applied Physics*, 04 1998, **vol. 83**, pp. 2772 – 2787, doi:<https://doi.org/10.1063/1.367037>.
- [31] DEMIRBAS, U., THESINGA, J., KELLERT, M., KÄRTNER, F. X., PERGAMENT, M.: Temperature dependence of the fluorescence lifetime and emission cross section of Tm:YLF in the 78-300 K range, *Opt. Mater. Express*, Dec 2022, **vol. 12(12)**, pp. 4712–4732, doi:<https://doi.org/10.1364/OME.475971>.
- [32] LU, Y., DAI, Y., YANG, Y., WANG, J., DONG, A., SUN, B.: Anisotropy of thermal and spectral characteristics in Tm:YAP laser crystals, *Journal of Alloys and Compounds*, 2008, **vol. 453**, pp. 482–486, ISSN 0925-8388, doi:<https://doi.org/10.1016/j.jallcom.2006.11.178>.
- [33] ZHANG, H., SUN, D., LUO, J., QUAN, C., CHENG, M., HU, L., HAN, Z., DONG, K.: Effect of Tm concentration on structure, defect, and spectral properties of Tm:YAP crystals, *Applied Physics A*, 2 2021, **vol. 127**, doi:<https://doi.org/10.1007/s00339-021-04875-1>.
- [34] ČERNÝ, P., ŠULC, J., JELÍNKOVÁ, H.: Continuously tunable diode-pumped Tm:YAP laser, in A. Sennaroglu, ed., *Solid State Lasers and Amplifiers II*, vol. 6190, International Society for Optics and Photonics, SPIE, 2006 p. 619008, doi:<https://doi.org/10.1117/12.662681>.
- [35] LOIKO, P., YUMASHEV, K., KULESHOV, N., RACHKOVSKAYA, G., PAVLYUK, A.: Detailed characterization of thermal expansion tensor in monoclinic KRe(WO₄)₂ (where Re=Gd, Y, Lu, Yb), *Optical Materials*, 2011, **vol. 34(1)**, pp. 23–26, ISSN 0925-3467, doi:<https://doi.org/10.1016/j.optmat.2011.07.007>.
- [36] GURETSKII, S., TRUKHANOVA, E., KRAVTSOV, A., GUSAKOVA, N., GORBACHENYA, K., KISEL, V., YASUKEVICH, A., LISIECKI, R., LUKOWIAK, A., KARPINSKY, D., OZEN, Y., OZCELIK, S., KULESHOV, N.: Tm³⁺:KY(WO₄)₂ single crystals: Controlled growth and spectroscopic assessment, *Optical Materials*, 2021, **vol. 120**, p. 111451, ISSN 0925-3467, doi:<https://doi.org/10.1016/j.optmat.2021.111451>.
- [37] GAPONENKO, M., LOIKO, P., GUSAKOVA, N., YUMASHEV, K., KULESHOV, N., PAVLYUK, A.: Thermal lensing and microchip laser performance of Ng-cut Tm³⁺:KY(WO₄)₂ crystal, *Applied Physics B*, 09 2012, **vol. 108**, doi:<https://doi.org/10.1007/s00340-012-5111-9>.
-

-
- [38] KAMINSKII, A. A., KONSTANTINOVA, A. F., OREKHOVA, V. P., BUTASHIN, A. V., KLEVTSOVA, R. F., PAVLYUK, A. A.: Optical and nonlinear laser properties of the $\chi(3)$ -active monoclinic α -KY(WO₄)₂ crystals, *Crystallography Reports*, 7 2001, **vol. 46**, pp. 665–672, ISSN 10637745, doi:<https://doi.org/10.1134/1.1387135/METRICS>.
- [39] GAPONENKO, M., DENISOV, I., KISEL, V., MALYAREVICH, A., ZHILIN, A., ONUSHCHEHKO, A., KULESHOV, N., YUMASHEV, K.: Diode-pumped Tm:KY(WO₄)₂ laser passively Q-switched with PbS-doped glass, *Applied Physics B*, 12 2008, **vol. 93**, pp. 787–791, doi:<https://doi.org/10.1007/s00340-008-3266-1>.
- [40] LAGATSKY, A., BROWN, C., SIBBETT, W., CALVEZ, S., DAWSON, M., GUPTA, J.: Highly efficient, broadly tunable 2- μ m femtosecond Tm:KYW laser, in *2011 Conference on Lasers and Electro-Optics Europe and 12th European Quantum Electronics Conference (CLEO EUROPE/EQEC)*, 05 2011 doi:<https://doi.org/10.1109/CLEOE.2011.5942457>.
- [41] GUPTA, J. A., LAGATSKY, A., DAWSON, M. D., CALVEZ, S., BROWN, C. T. A., SIBBETT, W., KISEL, V. E., KULESHOV, N. V.: Broadly tunable femtosecond mode-locking in a Tm:KYW laser near 2 μ m, *Optics Express*, Vol. 19, Issue 10, pp. 9995-10000, 5 2011, **vol. 19**, pp. 9995–10000, ISSN 1094-4087, doi:<https://doi.org/10.1364/OE.19.009995>.
- [42] VATNIK, S., VEDIN, I., PAVLJUK, A.: Diode-pumped thin disk 15% Tm:KYW laser, in V. A. Orlovich, V. Panchenko, I. A. Scherbakov, eds., *International Conference on Lasers, Applications, and Technologies 2007: Advanced Lasers and Systems*, vol. 6731, International Society for Optics and Photonics, SPIE, 06 2007 p. 673110, doi:<https://doi.org/10.1117/12.752836>.
- [43] BAGAYEV, S. N., VATNIK, S. M., MAIOROV, A. P., PAVLYUK, A. A., PLAKUSHCHEV, D. V.: The spectroscopy and lasing of monoclinic Tm:KY(WO₄)₂ crystals, *Quantum Electronics*, apr 2000, **vol. 30(4)**, p. 310, doi:<https://dx.doi.org/10.1070/QE2000v030n04ABEH001713>.
- [44] WEBER, M. J., MATSINGER, B. H., DONLAN, V. L., SURRATT, G. T.: Optical Transition Probabilities for Trivalent Holmium in LaF₃ and YAlO₃, *The Journal of Chemical Physics*, 07 1972, **vol. 57(1)**, pp. 562–567, ISSN 0021-9606, doi:<https://doi.org/10.1063/1.1678000>.
- [45] ZELMON, D. E., SMALL, D. L., PAGE, R.: Refractive-index measurements of undoped yttrium aluminum garnet from 0.4 to 5.0 μ m, *Appl. Opt.*, Jul 1998, **vol. 37(21)**, pp. 4933–4935, doi:<https://doi.org/10.1364/AO.37.004933>.
-

-
- [46] BARNES, N. P., GETTEMY, D. J.: Temperature variation of the refractive indices of yttrium lithium fluoride, *J. Opt. Soc. Am.*, Oct 1980, **vol. 70(10)**, pp. 1244–1247, doi:<https://doi.org/10.1364/JOSA.70.001244>.
- [47] SVELTO, O.: *Principles of lasers*, Springer US, 2010, ISBN 9781441913012, doi:<https://doi.org/10.1007/978-1-4419-1302-9>.
- [48] DING, J., GITIN, M., KAFKA, J.: MKS instruments handbook principles & applications in photonics technologies, 2019, URL https://www.newport-japan.jp/pdf/MKS_PHOTONICS_HANDBOOK.pdf.
- [49] HECHT, E.: *OPTICS 5th edition*, Pearson, 2016, ISBN 0133977226.
- [50] BEZUIDENHOUT, D. F.: *Handbook of Optical Constants of Solids*, Academic Press, 1997, ISBN 978-0-12-544415-6, doi:<https://doi.org/10.1016/B978-012544415-6.50082-0>.
- [51] PEDROTTI, F. L., PEDROTTI, L. M., PEDROTTI, L. S.: *Introduction to Optics*, Cambridge University Press, 12 2017, ISBN 9781108552493, doi:<https://doi.org/10.1017/9781108552493>.
- [52] SALEH, B., TEICH, M.: *Fundamentals of Photonics, 3rd Edition*, John Wiley, 2 2019, ISBN 9781119506874, doi:<https://doi.org/10.1002/0471213748>.
- [53] GLEBOV, L. B.: High brightness laser design based on volume Bragg gratings, *Laser Source and System Technology for Defense and Security II*, 5 2006, **vol. 6216**, p. 621601, ISSN 0277786X, doi:<https://doi.org/10.1117/12.667196>.
- [54] GLEBOV, L.: Volume Bragg Gratings in PTR glass - New Optical Elements for Laser Design, *Frontiers in Optics*, 2008, doi:<https://doi.org/10.1364/ASSP.2008.MD1>.
- [55] YUAN CHUNG, T., RAPAPORT, A., SMIRNOV, V., GLEBOV, L., RICHARDSON, M., BASS, M.: Solid-state laser spectral narrowing using a volumetric photothermal refractive Bragg grating cavity mirror, *Optics letters*, 2 2006, **vol. 31**, pp. 229–231, doi:<https://doi.org/10.1364/OL.31.000229>.
- [56] VOLODIN, B., DOLGY, S., MELNIK, E., DOWNS, E., SHAW, J., BAN, V.: Wavelength stabilization and spectrum narrowing of high-power multimode laser diodes and arrays by use of volume Bragg gratings, *Optics letters*, 2 2004, **vol. 29**, pp. 1891–1893, doi:<https://doi.org/10.1364/OL.29.001891>.
- [57] V., O. A., DORRER, C., SMIRNOV, V. I., GLEBOV, L. B., ZUEGEL, J. D.: Spectral filtering in a diode-pumped Nd:YLF regenerative amplifier using a volume Bragg grating, *Opt. Express*, 6 2007, **vol. 15**, pp. 8197–8202, doi:<https://doi.org/10.1364/OE.15.008197>.
-

-
- [58] VENUS, G., GLEBOV, L., ROTAR, V., SMIRNOV, V., CRUMP, P., FARMER, J.: Volume Bragg semiconductor lasers with near diffraction limited divergence, in G. L. Wood, M. A. Dubinskii, eds., *Laser Source and System Technology for Defense and Security II*, vol. 6216, SPIE, ISBN 0819462721, ISSN 0277786X, 5 2006 pp. 12–18, doi:<https://doi.org/10.1117/12.666193>.
- [59] SADIKU, M., MUSA, S., NELATURY, S.: Free space optical communications: An overview, *European Scientific Journal*, 02 2016, vol. 12, pp. 1857–7881, doi:<https://doi.org/10.19044/esj.2016.v12n9p55>.
- [60] KAUSHAL, H., JAIN, V., KAR, S.: *Free Space Optical Communication*, Springer New Delhi, 2017, ISBN 978-81-322-3689-4, doi:<https://doi.org/10.1007/978-81-322-3691-7>.
- [61] MEHENDALE, N., NEOGE, S.: Review on lidar technology, *SSRN Electronic Journal*, 01 2020, doi:<https://doi.org/10.2139/ssrn.3604309>.
- [62] CARIOU, J.-P., AUGERE, B., VALLA, M.: Laser source requirements for coherent lidars based on fiber technology, *Comptes Rendus Physique*, 2006, vol. 7(2), pp. 213–223, ISSN 1631-0705, doi:<https://doi.org/10.1016/j.crhy.2006.03.012>.
- [63] LAHYANI, J., THIERS, M., GIBERT, F., EDOUART, D., GOUËT, J. L., CÉZARD, N.: Hybrid fiber/bulk laser source designed for CO₂ and wind measurements at 2.05 μm, *Opt. Lett.*, Feb 2024, vol. 49(4), pp. 969–972, doi:<https://doi.org/10.1364/OL.510598>.
- [64] GORAJEK, L.: Linearly polarized 2044-nm pulsed laser generation in Ho:YAG active medium, *Optical Engineering*, 2022, doi:<https://doi.org/10.1117/1.OE.61.4.046104>.
- [65] ROMANO, C., PANITZEK, D., LORENZ, D., FORSTER, P., EICHHORN, M., KIELECK, C.: High-power thulium-doped fiber MOPA emitting at 2036 nm, *Journal of Lightwave Technology*, 2024, vol. 42(1), pp. 394–398, doi:<https://doi.org/10.1109/JLT.2023.3310121>.
- [66] ŠULC, J., NĚMEC, M., VYHLÍDAL, D., JELÍNKOVÁ, H., NEJEZCHLEB, K., POLÁK, J.: Holmium doping concentration influence on Ho:YAG crystal spectroscopic properties, in W. A. Clarkson, R. K. Shori, eds., *Solid State Lasers XXX: Technology and Devices*, vol. 11664, International Society for Optics and Photonics, SPIE, 2021 p. 1166413, doi:<https://doi.org/10.1117/12.2578284>.